SPONTANEOUS FORMATION OF QUANTIZED VORTICES IN BOSE-EINSTEIN CONDENSATES

by

Chad Nathan Weiler

A Dissertation Submitted to the Faculty of the

COLLEGE OF OPTICAL SCIENCES

In Partial Fulfillment of the Requirements
For the Degree of

DOCTOR OF PHILOSOPHY

In the Graduate College

THE UNIVERSITY OF ARIZONA

2 0 0 8

THE UNIVERSITY OF ARIZONA
GRADUATE COLLEGE

As members of the Final Examination Committee, we certify that we have read the dissertation prepared by Chad Nathan Weiler
entitled SPONTANEOUS FORMATION OF QUANTIZED VORTICES IN BOSE-EINSTEIN CONDENSATES
and recommend that it be accepted as fulfilling the dissertation requirement for the Degree of Doctor of Philosophy.

Brian Anderson — Date: 17 April 2008

Ewan Wright — Date: 17 April 2008

Poul Jessen — Date: 17 April 2008

Final approval and acceptance of this dissertation is contingent upon the candidate's submission of the final copies of the dissertation to the Graduate College.

I hereby certify that I have read this dissertation prepared under my direction and recommend that it be accepted as fulfilling the dissertation requirement.

Dissertation Director: Brian Anderson — Date: 17 April 2008

STATEMENT BY AUTHOR

This dissertation has been submitted in partial fulfillment of requirements for an advanced degree at The University of Arizona and is deposited in the University Library to be made available to borrowers under rules of the Library.

Brief quotations from this dissertation are allowable without special permission, provided that accurate acknowledgment of source is made. Requests for permission for extended quotation from or reproduction of this manuscript in whole or in part may be granted by the head of the major department or the Dean of the Graduate College when in his or her judgment the proposed use of the material is in the interests of scholarship. In all other instances, however, permission must be obtained from the author.

SIGNED: _____

Chad Nathan Weiler

ACKNOWLEDGEMENTS

The research performed during my dissertation has been some of the most challenging and the most rewarding work I have ever undertaken. Throughout the course of this work I have had the pleasure of working with numerous people who have helped define the start to my experimental career. My gratitude towards my advisor Brian Anderson for providing me with this opportunity cannot be measured. Brian fosters an environment in which the student can direct the experiment, yet he is always there when advice is needed. I believe that I had the opportunity to work with not only a great scientist but a wonderful friend.

In the lab I had the pleasure of working with numerous people of whom played an integral part in making this experiment work: David Scherer, Tyler Neely, Dave Henry, Dave Kaz, Elaine Ulrich, and Tim McComb. David and I spent many years together building up the lab. His strong work ethic and his great ability to teach allowed me to integrate into the group quickly. Tyler and I had the opportunity to work on a project that really tested our abilities as scientists. We worked immeasurably well together and I always knew that I could bounce an idea off of him and vice versa. Tyler has a wonderful knack for experimentation, which I believe will serve him well as he continues on his own scientific path. I am not sure that I have ever worked with a more enthusiastic and curious person than Dave Henry. Dave Kaz never ceased to bring a wonderfully quirky way of doing science to the lab. Elaine Ulrich was also responsible for helping construct the BEC apparatus, while Tim McComb brought a quiet yet efficient work ethic to the lab.

I would especially like to thank Tom Milster and his group members for providing me the opportunity to construct the computer generated holograms, phase dots, and binary masks. Specifically, I appreciate all the time and effort Delbert Hansen gave to me, teaching how to operate the maskless lithography tool and how to process the samples. Several other professors have been valuable to this dissertation: Poul Jessen, Ewan Wright, and Alex Cronin. Each has contributed to my scientific knowledge base.

Two guys who provided some great discussion and wonderful comic relief are Souma and O. May the 'video' live on in the annals of the Quantum Optics and BEC labs.

I would also like to thank my wife for being there for me when things seemed to be at their hardest. Her ability to listen and provide very practical and frank solutions helped me deal with the many challenges I faced throughout my graduate career.

Finally I would like to thank my parents and my extended family. They have always pushed me to dream big and always provided me with the means to do so.

DEDICATION

To my PopPop who encouraged me at a young age to tinker and was always willing to teach even though I was probably more of a hinderance than a help.
Also, to my wife whose patience and understanding have been remarkably steadfast during what has been a much longer process than either of us ever imagined.

TABLE OF CONTENTS

TABLE OF CONTENTS – *Continued*

TABLE OF CONTENTS – *Continued*

LIST OF FIGURES

LIST OF FIGURES – *Continued*

LIST OF TABLES

ABSTRACT

Phase transitions abound in the physical world, from the familiar water to ice transition, to the not so familiar normal fluid to superfluid transition. In the Bose-Einstein condensation phase transition, a gas of trapped bosonic atoms is cooled to a critical temperature. Below this temperature, a macroscopic number of atoms suddenly starts to occupy a single quantum state; these atoms comprise the Bose-Einstein condensate (BEC). The dynamics of the BEC phase transition are the focus of this dissertation and the experiments described here have provided new information on the details of BEC formation. New theoretical developments are proving to be valuable tools for describing BEC phase transition dynamics and interpreting new experimental results. With their amenability to optical manipulation and probing, along with the advent of new microscopic theories, BECs provide an important new avenue for gaining insight into the universal dynamics of phase transitions in general.

Spontaneous symmetry breaking in the system's order parameter may be one result of cooling through a phase transition. A potential consequence of this is the spontaneous formation of topological defects, which in a BEC appear as vortices. We experimentally observed and characterized the spontaneous formation of vortices during BEC growth. We attribute vortex creation to coherence length limitations during the initial stages of the phase transition. Parallel to these experimental observations, theory collaborators have used the Stochastic Gross-Pitaevski Equation formalism to simulate the growth of a condensate from a thermal cloud. The experimental and theoretical statistical results of the spontaneous formation of vortex cores during the growth of the condensate are in good quantitative agreement with one another, supporting our understanding of the dynamics of the phase transition. Ultimately, our understanding of the dynamics of the BEC phase transition may lead to a broader understanding of phase transitions in general, and provide new

insight into the development of coherence in numerous systems.

CHAPTER 1

INTRODUCTION

1.1 What is a phase transition?

As I was preparing to write this dissertation, I posed this question to several of my fellow graduate students. I was having a difficult time answering this question myself and was interested in their responses. A majority of my colleagues found it easy to come up with examples of phase transition, such as the water to ice transition, but similar to my own experience many had trouble trying to actually explain the physics of a phase transition. Many discussions of phase transitions do not give an actual definition but instead rely on a description of when a phase transition occurs [1–4]. Although my intent is not to be an authority on phase transitions, it is necessary to clarify what is meant by the occurrence of a phase transition in order to provide the necessary building blocks to understand the phenomenon of spontaneous vortex formation in Bose-Einstein condensates (BEC), the primary subject of this dissertation. Also, the dynamics of the BEC phase transition is immediately related to the development of coherence in condensates. This subject will be discussed in this dissertation, although in this chapter the discussion will be focused on developing a general conceptual description of phase transitions.

1.2 Phase Transition: a definition

Josiah Gibbs, one of the founders of modern thermodynamics, described a *phase* of matter as a "state of matter that is 'uniform throughout, not only in chemical composition but also in physical state'" [4]. In other words the system being studied must be in thermal equilibrium. With this knowledge, a phase transition can then be characterized as any abrupt change in one or more of these physical or chemical

properties. A simple example of an abrupt change in a physical property is the change of H_2O molecule density when going from liquid to solid. In these simple terms a phase transition is defined as the transformation of a system from one phase (or state of matter) to another.

Often in the literature [1], the concept of an order parameter is invoked to characterize the progress of a phase transition. Below a critical temperature in a thermodynamic phase transition, the spatial average of the order parameter is finite. As the system approaches the critical temperature from below the order parameter average approaches zero. Above the critical temperature it is zero; at the critical temperature it is undefined. This is the basis for which the average value of the order parameter can be used as a marker for a phase transition; the challenge is often to determine what quantity to associate with the order parameter for a given transition.

The 'order' of a phase transition describes the dynamical properties of the transition, whether the order parameter experiences a sudden discontinuous change at the phase transition (such is the case for a *first order transition*) or changes continuously (as is the case for *second and higher order transitions*). A plot of the order parameter versus temperature can been seen in Figure 1.1 for both first and second order phase transitions. Another distinguishing feature between a first order and a second order phase transition is that first order transitions usually need to have energy added to the system, in the form of latent heat, in order for the transition to occur. This is true for situations where the system approaches the critical point from above, in the opposite sense energy is actually released.

It has been demonstrated that the dynamics of a phase transition are intimately related to the order of the transition. It is therefore instructive to look at an example of a first order phase transition, one of the ^{3}He superfluid transitions, and a second order phase transition, the ^{4}He superfluid transition. From the diagram in Figure 1.2 it can be seen that ^{3}He has three distinct phases: the normal fluid phase, the superfluid A phase, and the superfluid B phase. Over a range of pressures and temperatures an A to B phase transition may occur. As the critical temperature

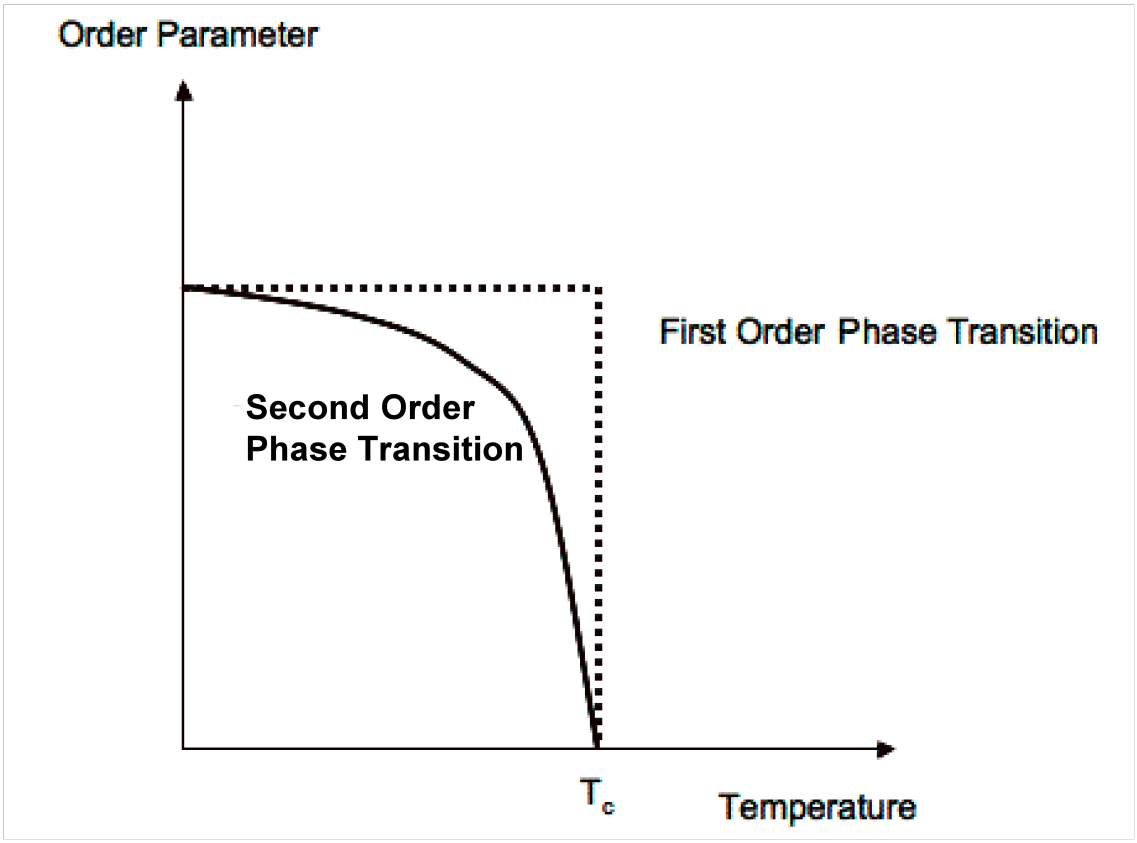

Figure 1.1: Graphical depiction of the behavior of the order parameter for a first order (dotted line) and second order phase transition (solid line).

for the B phase is approached (for some appropriate pressure) random thermal fluctuations in the order parameter will induce small bubbles of the B phase to form in the bulk A phase. A parameter of particular importance is the thermal correlation length ξ. It determines the length scale over which the order parameter varies, which in turn sets the size scale for the B phase bubble walls. Eventually, as the temperature is decreased further, the bubbles begin to grow (ξ begins to grow large) until they either meet other bubbles and merge or one particular bubble dominates and fills up the entire volume. This type of bubble nucleation arising from random thermal fluctuations is typical of first order phase transitions.

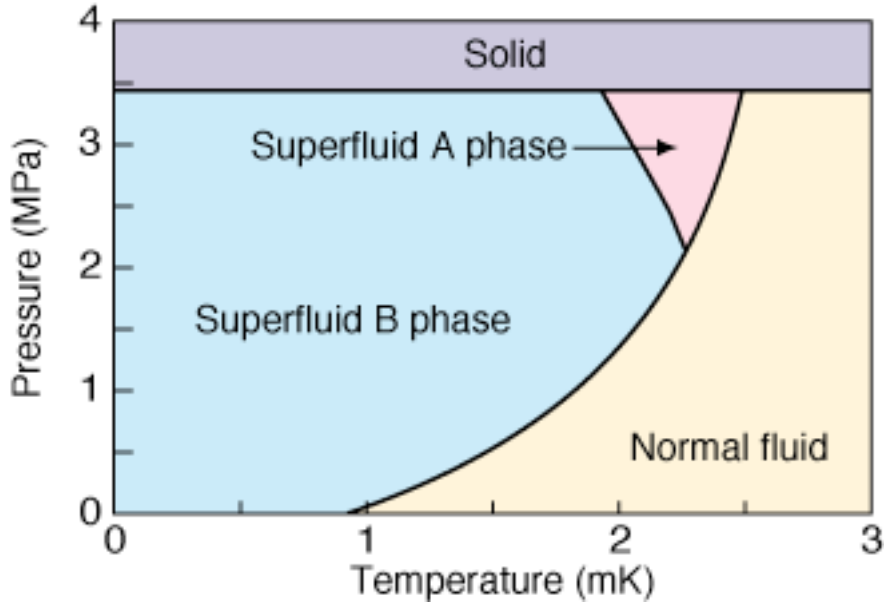

Figure 1.2: Phase Diagram of ^{3}He

In contrast to the first order case, second order phase transitions characteristically occur simultaneously at all points in a homogenous sytem. It is important to understand that at the critical temperature, differences between the two phases are minimal and therefore the system can move continuously between the two phases without needing to jump an energy barrier. This is largely due to the continuous nature of the order parameter during a second order transition. Consider the superfluid transition of ^{4}He. The order parameter of the system is related to the complex

number $\psi = \sqrt{\rho}\exp(i\theta)$ (where ρ is the density of the fluid and θ the quantum mechanical phase) that describes the quantum state of the superfluid system [1]. Here the use of a *coherence length* ξ is invoked to describe the length scale over which the order parameter ψ is correlated, i.e. the length scale over which changes in ψ can be observed. In the normal state ξ will be very short, while in the superfluid state it will be much longer. The coherence length can be compared to that of the spatial coherence length of light; the normal state being similar to that of white light and the superfluid state to that of narrow-bandwidth laser light.

In an ideal second order phase transition the coherence length diverges as the critical temperature is approached in thermal equilibrium [1, 5]. An infinite coherence length implies that the entire system is governed by the same order parameter. Thus, as long as the system remains in thermal equilibrium as the critical temperature is approached, it can be stated that the transition will occur everywhere simultaneously.

In practice keeping an entire macroscopic system in thermal equilibrium is very difficult to achieve due to the presence of random thermal fluctuations. Quite often these thermal fluctuations are responsible for causing multiple uncorrelated regions of the sample to undergo the phase transition. This is where the physics of phase transitions becomes murky because this type of nucleation very much resembles that of the bubble nucleation present in first order phase transitions. This is the source of much confusion in the dynamics of phase transitions. The above described dynamics are an important part to understanding the formation of spontaneous vortices in BECs.

1.3 Spontaneous Symmetry Breaking in Phase Transitions

Until this point nothing has been said about the symmetries that may be present within a thermodynamic system. A system undergoing a phase transition usually possess a symmetry property that is present in the high temperature phase, but gets lost in the low temperature phase [4]. For purposes of discussion I will call

the high temperature state the 'symmetric' state and the low temperature state the 'unsymmetric' state. This loss of symmetry has been given the name spontaneous symmetry breaking [1, 6–8]. Examples of spontaneous symmetry breaking during phase transitions abound: the acquisition of magnetization in a ferromagnet, the acquisition of quantum phase in the superfluid state of ^{4}He, the formation of domains in the universe after the big bang [9], and the acquisition of quantum phase in a BEC.* The latter becomes important in later discussions of spontaneous vortex formation in BEC. Associated with spontaneous symmetry breaking is the formation of topological defects. These topological defects can be considered as discontinuities of the system that get trapped in the normal/symmetric state as areas of the unsymmetric state begin to merge together during cooling of the system. The phenomenological understanding of defect formation during a phase transition is described by the Kibble-Zurek (KZ) scenario [9–11]. Defect formation during a spontaneous symmetry breaking phase transition will be discussed further in Chapter 2.

Spontaneous symmetry breaking phenomena are ubiquitous in physical systems [12, 13]. A classical example would be that of a particle moving in a double well potential. In equilibrium the particle will sit in one of the two minima. As soon as this choice is made the reflection symmetry is broken. A more general example [5] is that of a dinner table that has been set such that there is a plate in front of every guest's seat and a spoon halfway between adjoining plates. There is clearly a symmetry between left and right and each guest has a choice between the spoon on the left or the spoon on the right. As soon as a guest chooses a spoon the symmetry is broken spontaneously and all the other guests must conform to the initial guest's choice.† A description of spontaneous symmetry breaking in the

*The use of the word phase in these contexts is primarily meant to simplify discussions. In this context, phase refers to a quantum mechanical parameter, not the definition of phase of matter as presented on page 14. Strictly speaking, however, absolute phase is meaningless and only relative phases are important. We might thus think of symmetry breaking as the random relative phase that exists between two BECs that simultaneously created.

†A topological defect might correspond to multiple people making different choices simultane-

context of thermal phase transitions is not as easily explained. One must invoke the use of field theories to describe what symmetry means and how symmetry gets broken in phase transitions. The following discussion will provide intuition with regard to the relevant general ideas of field theory.

1.3.1 Spontaneous symmetry breaking: general field theory

Much of the field theory literature relates spontaneous symmetry breaking to that of a scalar field subject to the 'Mexican Hat' potential [1, 9]. This potential has the form

$$V(\phi) = \lambda(\mid \phi \mid^2 - \eta^2)^2 \tag{1.1}$$

where ϕ is the complex scalar field (the order parameter) and λ and η are constants. A potential of this type can be seen in Figure 1.3. This potential is symmetric under phase rotations, $\phi \rightarrow \phi e^{i\theta}$, about the vertical axis.

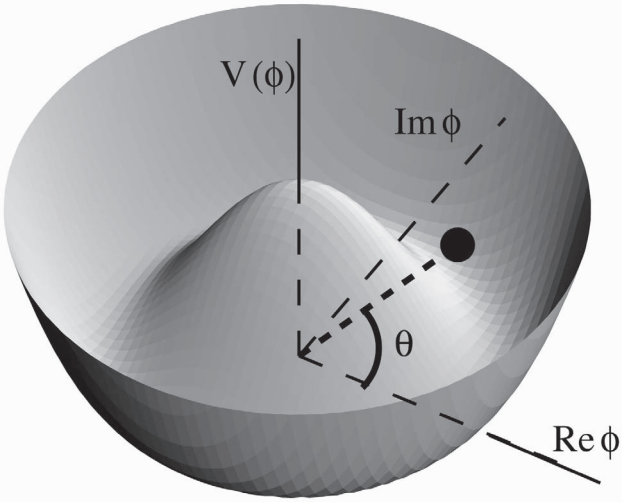

Figure 1.3: The Mexican Hat Potential: This potential is symmetric under phase rotations and has a maximum at $\phi = 0$. The minimum occur at around the circle $\mid \phi \mid = \eta$. The points on this circle represent different degenerate ground states. Image taken from [5].

---

ously, leaving some people with two spoons and some with none.

A phase transition will occur when the system approaches the critical temperature T_c. This critical temperture is dependent upon parameters of the potential. For $T > T_c$, large thermal fluctuations in the field ϕ allow it to jump over the maximum of the potential, and on average $\langle\phi\rangle = 0$ [14]. When the temperature is below T_c, the field ϕ settles into the valley of the potential well. In so doing the field chooses a phase θ, thus breaking the symmetry.

To provide a practical understanding of spontaneous symmetry breaking I have found an example given in reference [5] to be the most enlightening. It relates spontaneous symmetry breaking to that of the time of day. Consider being isolated from all other people and having full liberty to choose the time of day from any possible value between 0:00 and 23:59. With 24:00 being exactly the same as 0:00, a choice can be made from any number of possibilities lying on a circle. Thus we see the similarity between this situation and the field having a choice of any one of the vacuum manifold values around the circle of minima of the mexican hat potential.

In reality, our daily lives depend on us having synchronized our clocks with one another. If we did not it would be very difficult to coordinate meetings with others. The choice of a time standard breaks the symmetry and directly relates to the choice of phase the field takes at T_c. The situation that has been discussed thus far has been that of a global symmetry where the system is only symmetric under rigid rotations. Here if the field is subject to a rotation at one point in space it must be rotated by that same amount everywhere. There are cases where the idea of spontaneous symmetry breaking can be extended to what is known as a local gauge symmetry. In this case the field can be rotated at local points in space by different amounts, however the overall physical content contained in the field is retained. I will not discuss local gauge symmetries here but the reader is referred to references [5, 15–17].

1.4 The Bose-Einstein Condensate Phase Transition

Consider an ideal Bose gas consisting of N indistiguishable particles distributed among the microstates of a confining potential, such that any occupation number is allowable. The mean distribution of the particles will obey the Bose-Einstien distribution, which can be derived in several different manners; see for instance reference [4]. The mean occupation number for the *ith* state can be written as

$$n_i = \frac{1}{e^{(\epsilon_i - \mu)/k_B T} - 1} \tag{1.2}$$

where ϵ_i is the energy of the particle in the *ith* state, k_b Boltzmann's constant, μ the chemical potential of the system, and T the temperature. The quantities μ and T can be determined from constraints on total number N and total energy E:

$$N = \sum_i \frac{1}{e^{(\epsilon_i - \mu)/k_B T} - 1} \tag{1.3}$$

$$E = \sum_i \frac{\epsilon_i}{e^{(\epsilon_i - \mu)/k_B T} - 1} \tag{1.4}$$

For systems with a large number of particles and large volume the sums may be replaced by integrals

$$N = \int d\epsilon \frac{g(\epsilon)}{e^{(\epsilon_i - \mu)/k_B T} - 1} \tag{1.5}$$

$$E = \int d\epsilon \frac{\epsilon g(\epsilon)}{e^{(\epsilon_i - \mu)/k_B T} - 1} \tag{1.6}$$

where $g(\epsilon)$ is the density of states in the confining potential [18]. All of the ideal gas physics needed to characterize BEC are contained in equations 1.2–1.6.

In a 3D infinite square-well confining potential, the ground-state occupation number as a function of temperature can be determined from equations 1.5 and 1.6 by allowing both the volume V and the total number N to approach infinity and keeping the gas density fixed [19]. A critical temperature for an ideal gas BEC with particle mass m can be defined as

$$T_c, ideal = \frac{h^2}{2\pi m k} \left(\frac{n}{\zeta(3/2)}\right)^{2/3} \tag{1.7}$$

where $\zeta(z)$ is the Riemann zeta function and $\zeta(3/2) \approx 2.612$. When the system is cooled below this temperature particles in the gas accumulate in the ground state of the system; the system undergoes a phase transition to a Bose-Einstein condensed state. Although this result was specific for a homogeneous potential, the ideas presented can be extended to accommodate all confining potentials where the critical temperature exceeds the energy splitting between levels of the system [20]. It is the search to understand the dynamics of this particular phase transition that will dominate the remainder of the discussion in this thesis. More specifically, we attempted to begin to develop a more thorough understanding of how the condensate begins to grow from the thermal cloud, how coherence is developed in the condensate, and use what we learned to broaden our understanding of other phase transitions in the physical world.

1.5 Layout of this Dissertation

In the interest of providing quick access to the ideas and data presented in this dissertation, the following will be the 'road map' for the rest of the material presented. In Chapter 2, a discussion on the formation of topological defects during a phase transition will be presented. Defect formation is a direct consequence of spontaneous symmetry breaking and the ideas set out in Chapter 1 will provide a basis for our understanding these defects. The Kibble-Zurek scenario will also be discussed. This scenario provides a model for calculating the coherence length during the transition and utilizes this knowledge along with other initial conditions to calculate a density of defects. A small digression will be taken to discuss some of the essential physics needed to tie the physics of spontaneous symmetry breaking and topological defect formation to that of a condensate. The chapter will close with a section devoted to relating the ideas of the Kibble-Zurek mechanism to the BEC phase transition.

Chapter 3 will present a list of many of the experiments that the have seen the existence of topological defect formation. Many of these experiments have attempted to match the ideas presented by the Kibble-Zurek scenario and brief overview of their

successes and failures will be given.

Chapter 4 discusses the three-well trap experiment presented in [21, 22]. An overview of the general experimental techniques used to get to condensation will be given. A brief synopsis of the three-well experiment will follow, with a quick summary of the main results. The end of this chapter will focus on using this experiment as a model for understanding the formation of spontaneous vortices in BECs.

Chapter 5 will provide an overview of techniques used to generate computer generated holograms for use in manipulating condensates. Some of the techniques use to make holograms were directly employed in the experiment discussed in Chapter 4.

In Chapter 6, I will discuss the findings during our experiments involving spontaneous vortices. I will provide an overview of the various experiments that were performed. I will compare our experimental results with the theoretical results produced by our collaborators at the University of Queensland in Queensland, Australia.

Chapter 7 is devoted to the investigations of spontaneous vortices in a toroidal trap geometry. Data analyis for both the experiment and theory will be presented.

Chapter 8 will be a summary of the major results presented in this dissertation. A quick review of three main experiments involving the spontaneous formation of vortices will be given along with a summarization of the main results. There are many avenues that can be taken to further our understanding of the creation of spontaneous vortices in BECs and the development of coherence in BECs. I will take the liberty of discussing them here.

CHAPTER 2

TOPOLOGICAL DEFECT FORMATION AND THE KIBBLE-ZUREK SCENARIO

2.1 Introduction

The discussion in this chapter introduces a well-known model used to relate the phenomenon of topological defect formation to spontaneous symmetry breaking. The model, known as the Kibble-Zurek scenario [9, 10], provides a prescription for estimating the coherence length ξ present at the critical temperature for a second order phase transition. As will be seen, an estimate of ξ at the critical point directly leads to an estimate of the density of defects that may spontaneously form. The features of topological defect formation present in the Kibble-Zurek scenario will be related to the BEC phase transition through a simplistic representation of the condensate formation process. This approach will provide physical intuition about the possible mechanisms responsible for spontaneous vortex formation in condensates.

2.2 Topological Defect Formation: The Kibble Scenario

We assume that the state of a system undergoing a second-order phase transition can be represented by the complex field ϕ. The main idea behind the formation of topological defects during a symmetry-breaking phase transition is that as the system approaches the critical temperature the field ϕ settles into the valley of the mexican hat potential, as described in Section 1.3. In so doing, the field chooses a phase θ, spontaneously breaking the symmetry of the possible outcomes. It is as if each one of these regions can be thought of as having its own independent 'mexican hat' potential associated with it. Thus, the phase associated with each region has a choice of any one of the possible values from 0 to 2π around the minimum of the

potential. The length scale over which the regions must be spaced to be considered independent is set by the aforementioned coherence length ξ: regions separated by a distance longer than ξ will be completely uncorrelated from one another and will therefore have independent phases. Within each region ξ, the field is constant; between each region the field will be completely random. As the system is cooled further the independent regions will continue to grow, eventually merging together to form the bulk phase of matter.

It is possible that around any closed path in space that the phase changes between regions form a $2n\pi$ loop. At the center of such an arrangement the field amplitude of ϕ must vanish, leaving behind a topological defect. This is due to continuity arguments, namely that the field must be continuous and single valued. Topological defect formation resulting from a symmetry-breaking phase transition was first postulated by Tom Kibble in 1976 while describing the dynamics of the early universe [9]. An illustration of a general case where a topological defect exists in the field ϕ can be seen in Figure 2.1. For superfluid systems, BECs included, these topological defects take the form of quantized vortices. Knowledge of the coherence length ξ and the size of the system provides the means of calculating the density of defects expected for particular initial conditions as will be shown below. Thus for superfluids, the ability to calculate ξ would provide insight into the development of long range coherence of the system.

Kibble's ideas were directed at understanding the dynamics of the early universe, which are not easily emulated with experiment. However, as mentioned in Chapter 1, spontaneous symmetry breaking phase transitions are seen in numerous systems. Presumably, it could be possible to model other phase transitions after Kibble's conjecture and therefore make comparisons between spontaneous symmetry breaking phase transitions. In 1984, Wojciech Zurek recognized the possibility of extending these ideas to something more tangible, the superfluid phase transition of ^{4}He [10]. His theory was based on the Ginzburg-Landau theory [4] and provided a prescription for calculating ξ. He also suggested a method for manipulating the ^{4}He superfluid transition to validate his predictions. Zurek later extended his ideas to

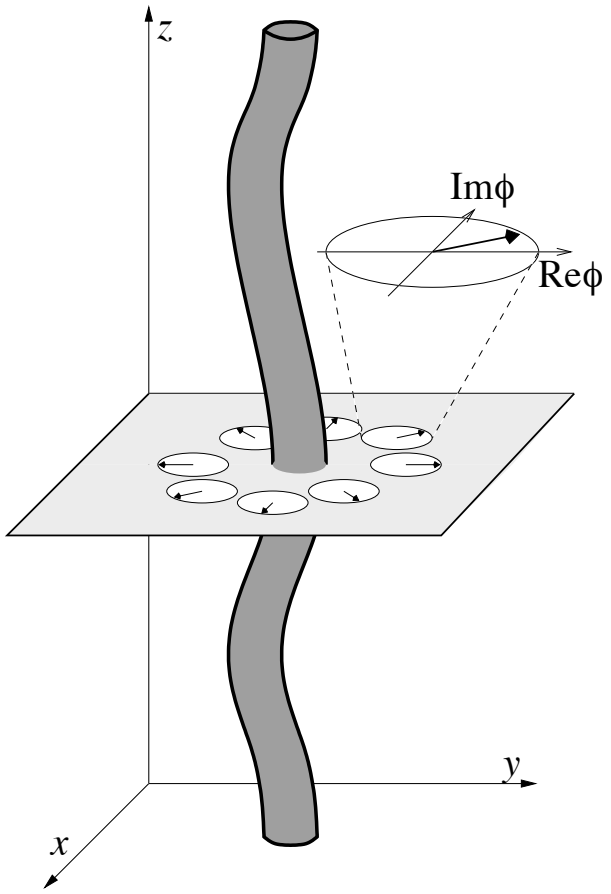

Figure 2.1: An example of a vortex line in three dimensions that could be produced during a phase transition. In the cross sectional plane, the arrows indicate the direction of the complex scalar field ϕ. Around the vortex core the direction rotates by a full 2π, and the field vanishes at the center. (Figure taken from reference [5], Figure 2)

other systems, specifically BECs [11]. This will prove pertinent to later discussions on the spontaneous vortex formation of vortices in BECs.

The combination of Kibble's ideas and Zurek's further elaborations has been designated as the Kibble-Zurek scenario and will be the subject of the next section. There is one caveat to the above discussion: although Kibble's ideas are relevant for all phase transitions (both discontinuous and continuous), Zurek's work is strictly applicable to the continuous case only. Since the BEC phase transition is a continuous transition, the focus of the remainder of this dissertation will be on transitions of this type.

2.3 Kibble-Zurek Scenario

The following discussion of the Kibble-Zurek scenario is relevant for the superfluid phase transition. As the system temperature T is quenched from above towards the critical value T_c, the relaxation rate of the system slows. The relaxation rate is defined as $1/\tau$, where τ characterizes the equilibration time and takes the form

$$\tau = \tau_0 k_B T / \mid \mu \mid \tag{2.1}$$

where τ_0 is the collision time for elastic collisions between particles, k_B is Boltzmann's constant, and μ is the chemical potential [11]. We can assume that the temperature during the phase transition will decrease linearly in time,

$$T(t) = (1 - \frac{t}{\tau_q})T_c \tag{2.2}$$

where τ_q is known as the quench time and characterizes the rate of cooling in the system. At a critical time $t = -\hat{t}$ before the critical point (defined to be at $t = 0$), the relaxation rate $1/\tau$ becomes slower than the cooling rate $1/\tau_q$ of the forced temperature quench. The system then falls out of equilibrium and the correlation length ξ of the system at $t = -\hat{t}$ is essentially 'frozen' into the gas for the remainder of the transition. The value for ξ at this point is then defined as

$$\xi = \lambda_{T_c}(\tau_q/\tau_0)^{1/4} \tag{2.3}$$

where λ_{T_c} is the thermal de Broglie wave length of a gas particle at the critical temperature. The thermal de Broglie wavelength is defined as $\lambda_{T_c} = \sqrt{\frac{h^2}{2\pi m k_B T_c}}$, where h is Planck's constant and m is the mass of the particles in question. The 1/4 power dependence of ξ on τ_q is accounted for by mean field theories relevant for BECs [10, 11].

Putting this in context with that which was described in Section 2.2, if the system size is significantly larger than ξ, different regions of the system will choose their phases independently as the superfluid forms; eventually these must merge with the restriction that the macroscopic wave function for the superfluid be single-valued. The merging will randomly give phase loops of 2π that result in superfluid vortices (see Section 4.4 for a more complete description). The coherence length can be considered the size of the domains surrounding a particular defect, in this way we can use the prediction to calculate the density of defects; for superfluid systems the defect density is $\propto 1/\xi^2$ [10, 11]. From Equation 2.3 it is seen that faster cooling rates will produce the freezing in of a smaller correlation length ξ, and hence a higher density of vortices immediately after the transition. The next chapters will serve to tie the ideas presented in Chapters 1 and 2 to the formation of spontaneous vortices in BECs.

2.4 Universality

In this dissertation the point is made that continuous phase transitions are ubiquitous across physics. What is perhaps most interesting about many of these different systems is that they obey universal thermodynamic properties near the phase transition that depend only on a small number of features, such as dimensionality and symmetry [1, 5, 23, 24]. One such example would be the divergeance of the coherence length ξ during a second order phase transition. These universal properties are insensitive to the underlying microscopic properties of the system. The ability to lump many wildly different systems undergoing continuous phase transitions into unifying groups is known as universality. The universal nature of phase transitions

has allowed for a broad cross-fertilization of fields [25]. Specifically, small scale systems, such as condensed matter systems that are very accessible to researchers, can provide insight into the dynamics of large scale systems, such as the universe which are not accessible to laboratory experimentation [25].

The characterization of universality classes is done through the use of critical exponents. It has been shown that many of the universal properties associated with continous phase transitions have a power law dependence. For example, Zurek showed that for continuous phase transitions, there is a power law dependence of the coherence length ξ on the quench time τ_Q, namely $\xi \propto \tau_q^\sigma$ [10]. A good portion of the experimental phase transition research in condensed matter systems has focused on measuring this power law dependence (see Chapter 3 for a summary of these experiments).

2.5 Properties of BECs

2.5.1 What is meant by coherence of a BEC

The term coherence is widely used in the physics literature. Here we loosely define coherence as the predictability of the change in phase $\delta\theta$ across points in space (or time). For a discussion on the relationship of coherence to a condensate, it is instructive to define the quantum state of the BEC, which is well-approximated by the complex function

$$\Psi(\vec{r}) = \sqrt{n(\vec{r})}e^{i\theta(\vec{r})}. \tag{2.4}$$

Here, $n(\vec{r})$ and $\theta(\vec{r})$ are the spatially varying condensate density and quantum phase, respectively [26, 27]. We may call this the condensate wave function. Spatial coherence in a condensate is therefore the predictability of the quantum phase difference $\delta\theta(\vec{r})$ [18] between points r_1 and r_2 within the condensate for any given time. Many experiments have demonstrated the coherent properties of BEC, most notably, the Ketterle group's observation of interference fringes between two condensates [28]. In this experiment two separate condensates were formed in a double well potential;

the condensates were then released from the trap and allowed to ballistically expand. In the overlap region of the two clouds high contrast matter wave fringes were observed, thus demonstrating the ability to measure the relative phases between two condensates and providing clear evidence for coherence in the system.

To correlate these coherence ideas with the physics that have been discussed earlier in this dissertation, it is seen that the coherence length ξ of a fully formed spatially coherent condensate is at least as large as the width of the condensate [29]. However, this coherence length is only relevant for the condensate itself; it does not describe coherence within the non-condensed thermal atomic cloud. As stated earlier in this chapter, the coherence length of the system is important and central to understanding the dynamics of a phase transition and will be the focus of a discussion in Chapter 6 about the spontaneous formation of vortices in the BEC phase transition.

2.5.2 Quantized vortices

An important consequence of the condensate wave function being written as in Equation 2.4, is that we can define the velocity of fluid flow $v(\vec{r})$ as

$$\vec{v}(\vec{r}) = \frac{\hbar}{m}\nabla\theta(\vec{r}) \tag{2.5}$$

where $\hbar$ is Planck's constant, m is the mass of a ^{87}Rb atom, and $\theta(\hat{r})$ is the condensate phase profile. It is immediately seen that $\vec{v}(\vec{r})$ is irrotational from

$$\nabla \times \vec{v}(\vec{r}) = 0 \tag{2.6}$$

unless the phase of the wave function has a singularity[30].

From quantum mechanics we know that the condensate wave function must be single-valued, therefore around any closed loop the change in the phase of the wave function$\Delta\ \theta$ must be a multiple of 2π, meaning

$$\Delta\theta = \oint \nabla\theta \cdot d\vec{l} = 2\pi\ell \tag{2.7}$$

where ℓ is an integer. We can then define the circulation Γ around a closed contour to be

$$\Gamma = \oint \vec{v} \cdot d\vec{l} = \frac{\hbar}{m} 2\pi\ell = \ell \frac{h}{m}, \tag{2.8}$$

which shows that the circulation is quantized in units of h/m. Equation 2.8 is known as the Onsager-Feynman quantization condition [27].

A wonderful example of such a flow is presented in reference [30]. Here the authors describe a situation where a purely azimuthal flow in a trap is invariant under rotation about the z axis. In order for the condensate wave function to satisfy the single-valuedness condition it must vary as $e^{i\ell\varphi}$, where φ is the azimuthal angle. A situation such as this can be seen in Figure 2.2 If we define ρ as the radial

Figure 2.2: Depiction of situation where the phase increases azimuthally around the z axis from 0 to 2π

distance from the center of the trap we find using Equation 2.8 that the velocity is

$$v_\varphi = \ell \frac{\hbar}{m\rho}. \tag{2.9}$$

If the contour encloses the axis, the circulation will be lh/m and zero otherwise. Upon inspection of Equation 2.9, it is seen that if $\ell \neq 0$, the condensate wave function must go to zero or else the azimuthal kinetic energy will diverge. The flow pattern in this case will be that of a vortex line.

One final note, for an external potential with axial symmetry and for a state that has a singularity directly on axis, the angular momentum per particle will be

$\ell\hbar$ about the axis, with the total angular momentum L about the axis being $N\ell\hbar$, where N is the total number of atoms. However, any system with a singularity off axis will have some average fraction of $\ell\hbar$ per particle, with the total angular momentum being proportionally lower by that fraction.

2.5.3 Vortices in BEC

One of the signature features of a superfluid system is the existence of quantized vortices [31, 32]. The observations of quantized vortices in BEC [33] have provided much insight about the superfluid properties of BEC. Vortices in BEC have been created using a myriad of methods, from quantum phase manipulation [33, 34], to turbulance [35], to rotating traps [36–39], and dynamical instabilities [40, 41]. In references [21, 22] we discussed how vortices could be produced via the mixing of initially isolated superfluids. It was emphasized that our approaches were unique in that they utilized coherent dynamics of condensate mixing to produce vortices rather than through external manipulation such as stirring. The remainder of this dissertation will build on these ideas by utilizing our understanding of merging dynamics to gain insight into the BEC phase transition dynamics and the development of coherence in condensates.

2.6 Kibble-Zurek Scenario, Vortices, and the BEC Phase Transition

The physical process behind spontaneous vortex formation in BECs is intimately connected to the dynamics of condensate growth. A simple picture, illustrated in Fig. 2.3, suggests that near the critical point of the phase transition proto-condensates of characteristic size ξ form with individual macroscopic wave functions and random relative phases. These causally isolated regions then merge together as the transition proceeds with the requirement that the resulting macroscopic wave function is continuous. The initially discrete phase differences lead to a phase *gradient* in the merged state, with the lowest energy configuration having the smallest possible gradient; for example, regions with phases of $\pi/4$ and $7\pi/4$ will connect

through a continuous phase change of $\pi/2$, rather than $3\pi/2$ in the opposite direction. This is an example of the so-called Geodesic rule [42, 43] for determining the angle between two points on a sphere (or circle). Occasionally three or more merging regions can trap a 2π phase loop within the condensate, as illustrated in Fig. 2.3. Due to the requirement of continuity of the macroscopic wave function, the condensate density at these locations is topologically constrained to be zero, resulting in the formation of a *quantized vortex.* Although this model is somewhat simplistic in scope it helps build intuition about the mechanisms present during the BEC phase transition that are possibly responsible for the creation of topological defects, and relates them to the Kibble-Zurek scenario. The focus of the remainder of this dissertation is to introduce the first combined experimental and theoretical study of spontaneous vortex formation in BECs and accumulate knowledge about the development of condensate coherence during the BEC phase transition.

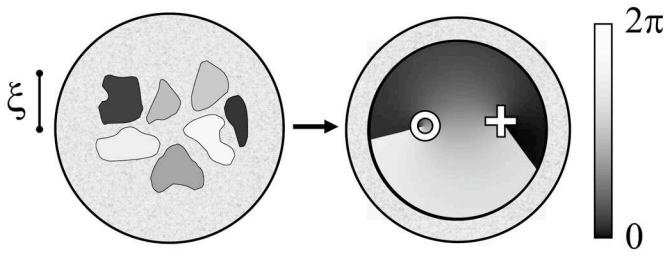

Figure 2.3: Schematic of spontaneous vortex formation in a trapped BEC. (Left) As a thermal gas (mottled grey shade) is cooled through the BEC transition, isolated proto-condensates of approximate size ξ and unpredictable phase may form[11]. Quantum phase ranges from 0 to 2π, and is represented here by shades of gray, as indicated by the gradient bar at the right. (Right) Proto-condensates eventually merge to form a single BEC (continuous greyscale region), potentially forming quantized vortices. Here, a positive (negative) vortex is labeled with a cross (circle), with the phase winding direction corresponding to the direction of superfluid flow and phase gradient around the vortex core.

2.7 Vortices from Mode Interference

The Kibble-Zurek scenario is one method that can be used to describe superfluid and condensate growth. The Ginzburg-Landau theory on which the Kibble-Zurek scenario is based allows for its application to both classical and quantum phase transitions, thus making it a universal model. However, other models exist for describing the BEC phase transition that are based solely on quantum mechanical principles. One such model was proposed by Svistunov and co-workers. It outlines a qualitative yet more complex three-stage scenario of superfluidity and condensate formation in a homogeneous Bose gas [44–47] (for a summary see reference [48]). In the first of these stages, known as the kinetic (or weak-turbulent) stage, a wave in momentum space propagates towards zero momentum as energy is removed from the system, resulting in the macroscopic occupation of a number of low-energy atomic field modes. Interference between these modes having random relative phases leads to nodes in the total field, which appear as lines of zero atomic density. In the subsequent coherent (or strong-turbulent) stage, a *quasi-condensate* having local coherence but no long-range coherence grows around the lines of zero density, which simultaneously evolve into well-structured vortex cores. The final stage involves long-range ordering, where the superfluid relaxes into equilibrium and a true condensate with global phase coherence is achieved.

Berloff and Svistunov numerically demonstrated this scenario for the *homogeneous* Bose gas in simulations of the Gross-Pitaevskii equation [49]. These three stages, however, do not necessarily occur for the *harmonically trapped* Bose gas which is relevant for our experimental studies. If the mean time between collisions of trapped particles is greater than the time it takes for them to traverse the trap, a pure condensate whose phase coherence spans the entire system may form from the beginning [50]. This assumption has always been made in previous models of condensate formation in harmonic traps [51–56], and with the exception of condensate growth in the hydrodynamic regime[57], has been broadly successful in describing experimental observations [58–61]. This type of growth would not support the spon-

taneous creation of vortices. In contrast, as will be described in Chapter 6, our work experimentally studied condensate growth in a harmonic trap and observed vortices in the resulting condensates. Although the mechanisms proposed by Svistunov et. al. are qualitatively appealing, it is more difficult to obtain simple numerical estimates of the coherence length ξ and the density of spontaneously formed vortices in a phase transition. For this reason both the Kibble-Zurek scenario and the description of mode interference are useful in interpreting observations of spontaneously formed vortices.

CHAPTER 3

EXPERIMENTAL STUDIES OF SPONTANEOUS TOPOLOGICAL DEFECT FORMATION

3.1 Introduction

This Chapter provides an overview of the various systems in which the predictions of the Kibble-Zurek scenario have been tested experimentally. In some cases agreement was found between predictions and experimental results; however in most cases comparisons were not able to be made or were found not to be in good correspondence. These investigations portray the difficulties faced by the experimenter in trying to verify the dynamics present during a symmetry breaking phase transition. Further discussion of some of the experiments may be found in summary articles by A. J. Gill [1], A. Rajantie [15], and T. Kibble [25].

3.2 Nematic Liquid Crystals

1. ∗ **I. Chuang, R. Durrer, N. Turok, and B. Yurke, "Cosmology in the Laboratory: Defect Dynamics in Liquid Crystals,"** ***Science*****, vol. 251, pp. 1336–1342, 1991.**

   ∗ **I. Chuang, N. Turok, and B. Yurke, "Late-Time Coarsening in a Nematic Liquid Crystal,"** ***Physical Review Letters*****, vol. 66, pp. 2472–2475, 1991.**

   This is the first experiment that looked for the presence of defects after a rapidly induced phase transition. The transition was initiated by performing rapid pressure and temperature quenches. Nematic liquid crystals are unique systems in that they support the three most interesting defects also relevant to cosmology: strings, monopoles, and textures. Strings in liquid crystals are the

defects most resembling vortices in superfluids. In this work qualitative comparisons were made between observations and the Kibble-Zurek scenario; however since the Nematic liquid crystal transition is a first-order phase transition the theory of the dynamics governing the transition are somewhat different. The dependence of the defect number density on τ_Q was not tested.

2. **M. J. Bowick, L. Chandar, E. A. Schiff, and A. M. Srivastava, "The Cosmological Kibble Mechanism in the Laboratory: String Formation in Liquid Crystals," *Science*, vol. 263, pp. 943–945, 1994.**

   The experiment reported here focused on predicting the formation of string defects by observing domain coalescence. By performing a temperature quench of the liquid crystal and imaging with a phase contrast microscope, the researchers were able to view the nucleation of bubbles of the nematic liquid crystal phase as the cooled the system. An estimation of the minimum sized bubble needed to contribute to string formation provided the ability to make qualitative comparisons to the Kibble scenario. However, since this system undergoes a first-order phase transition defect densities as a function of τ_Q were not calculated.

3. **S. Digal, R. Ray, and A. M. Srivastava, "Observing Correlated Production of Defects and Antidefects in Liquid Crystals," *Physical Review Letters*, vol. 83, pp. 5030–5033, 1999.**

   Reported here are first time observations of correlations between defects and anti-defects. The experimenters present a new technique to determine the winding of the defects and demonstrate that it is extremely efficient.

3.3 Superfluids

3.3.1 ^{4}He

1. **P. C. Hendry, N. S. Lawson, R. A. M. Lee, P. V. E. McClintock, and C. D. H. Williams, "Generation of defects in superfluid ^{4}He as**

an analogue of the formation of cosmic strings" *Nature*, vol. 368, pp. 315–317, 1994.

This was the first test of Kibble-Zurek ideas in superfluid systems. The system was cooled to just above the superfluid critical temperature in a chamber that was able to be rapidly expanded. The rapid expansion lowered the pressure, allowing the system to undergo the superfluid phase transition. To measure the presence of vortices the researchers analyzed the attenuation of second sound, which is strongly dissipated by the presence of vortices. Their experimental observations showed evidence for the presence of vortices, however their results were inconclusive due the fact that it was unclear whether the vortices were created by the temperature quench or through other means, specifically hydrodynamic turbulence generated by the expansion process used.

2. **M. E. Dodd, P. C. Hendry, N. S. Lawson, P. V. E. McClintock, and C. D. H. Williams, "Nonappearance of Vortices in Fast Mechanical Expansions of Liquid ^{4}He through the Lambda Transition," *Physical Review Letters*, vol. 81, pp. 3703–3706, 1998.**

   This is a follow up experiment to the one immediately above. Here the researchers took care to minimize vortex creation via hydrodynamic turbulence. Again, the transition was induced through the use of a rapid expansion. The generated vortex densities were found to be a factor of two below those predicted by the Kibble-Zurek scenario. There also were instances where no vortices were detected. It has become generally believed the the vortices decay rapidly, making them very difficult to view experimentally [62, 63].

3.3.2 ^{3}He

1. **C. Baürle, Yu. M. Bunkov, S. N. Fisher, H. Godfrin, and G. R. Pickett, "Laboratory simulation of cosmic string formation in the early Universe using superfluid ^{3}He," *Nature*, vol. 382, pp. 332–334, 1996.**

This experiment utilizes superfluid ^{3}He's ability to absorb a slow neutron. The absorption of the neutron by the superfluid heats a small region of the fluid above the critical temperature, and through rethermilzation the sample cools back through the transition, thus generating a tangle of vortices as the system cools. The absorption reaction $n+^3\text{He}\rightarrow p+^3\text{He}$ releases 764 keV of energy (n reprsens a neutron and p a proton). In this experiment an oscillating wire technique was used to measure the energy liberated after the neutron absorption. The energy release was found to be in the range of 600 to 650 keV, with another 50 keV lost to UV radiation. However, this still leaves an energy deficit and vortices are the likely form in which the energy could reside. The residual energy in the liquid correlated well with the predictions of the Kibble-Zurek scenario.

2. **V. M. H. Ruutu, V. B. Eltsov, A.J. Gill, T.W.B. Kibble, M. Krusius, Yu. G. Makhlin, B. Plaçais, G. E. Volovik, and Wen Xu, "Vortex formation in neutron-irradiated superfluid ^{3}He as an analogue of cosmological defect fromation," *Nature*, vol. 382, pp. 334–336, 1996.**

   Similar to the above study, this group also used neutron absorption to heat the sample, though their technique for analyzing vortex formation was much different. The technique employed was to spin the cryostat below the superfluid critical velocity such that the normal fluid rotates with the cryostat but the superfluid component remains completely stationary. The system was subsequently bombarded with neutrons therefore producing vortex tangles in the superfluid. The subsequent differential velocity between the normal and superfluid component subjects the vortices to a transverse Magnus force, which forces the vortices to expand and move into a central cluster where they can be counted. Nuclear magnetic resonance (NMR) techniques were utilized to view the vortices. This study demonstrated that vortices could be formed from the heating and subsequent cooling of the superfluid occurring after neutron ab-

sorption, however the researchers were unable to sufficiently provide evidence of the dependence of the vortex density on the quench rate.

3.4 Superconductors

3.4.1 Thin films

1. **R. Carmi, E. Polturak, "Search for spontaneous nucleation of magnetic flux during rapid cooling of $YBA_2Cu_3O_{7--\delta}$ films through T_c," *Physical Review B*, vol. 60, pp. 7595-7600, 1999.**

   This experiment aimed to observe spontaneous flux lines during a thermal quench of $YBA_2Cu_3O_{7--\delta}$ (YBCO) thin films through the normal to superconductor transition. The thin film is heated by a focused light beam and subsequently cooled by a strong thermal link to liquid nitrogen. The flux lines were measured using a high T_c superconducting quantum interference device (SQUID). In all instances no evidence for the presence of spontaneous flux lines was seen. The researchers attributed this to the possibility that the Kibble-Zurek vortex density calculation may be much smaller in practice than the predicted value.

2. **A. Maniv, E. Polturak, G. Koren, "Observation of Magentic Flux Generated Spontaneously During a Rapid Quench of Superconducting Films," *Physical Review Letters*, vol. 91, p. 197001, 2003.**

   The main difference between this experiment and the above experiment is that the cooling rate was approximately eight orders of magnitude faster. The presence of vortices was seen in this experiment and a reasonable fit to a power law dependence of the total magnetic flux on the quench rate was obtained. However, their exponent was not very tightly constrained therefore making it hard to make any major comparisons. The interpretation of these results is further complicated by the fact that the symmetry that is broken is a local gauge symmetry, which was shown by Hindmarsh and Rajantie to exhibit two

different mechanisms for defect formation [64].

3.4.2 Thin film rings

1. **J. R. Kirtley and C. C. Tsuei, "Thermally Activated Spontaneous Fluxoid Formation in Superconducting Thin Film Rings," *Physical Review Letters*, vol. 90, p. 257001, 2003.**

   The geometry of the superconductor in this study was that of thin film superconducting rings. Even though the quench rate was able to be varied over five orders of magnitude, it was found that defect density was only very weakly dependent on the quench rate. This is in agreement with local gauge theories. Kirtley and colleagues argued that the trapped fluxons generated in the experiment would be eliminated via tunneling mechanisms into and out of the rings.

3.4.3 Josephson junctions

1. **R, Carmi, E. Polturak, and G. Koren, "Observation of Spontaneous Flux Generation in a Multi-Josephson-Junction Loop," *Physical Review Letters*, vol. 84, pp. 4966–4969, 2000.**

   The investigations utilized a superconducting loop that contained 214 Josephson junctions in series. As the system is cooled each one of the 214 sections between the junctions chooses its own phase. Therefore it can be seen that the phase will make a random walk around the loop. In their study, the presence of flux was seen; however the researchers made no attempt to investigate the dependence of the flux on the cooling rate.

2. $*$ **E. Kavoussanaki, R. Monaco, and R. J. Rivers, "Testing the Kibble-Zurek Scenario with Annular Josephson Tunnel Junctions," *Physical Review Letters*, vol. 85, pp. 3452-3455, 2000.**

   $*$ **R. Monaco, J. Mygind, and R. J. Rivers, "Zurek-Kibble Domain Structures: The Dyanmics of Spontaneous Vortex Formation in**

Annnular Josephson Tunnel Junctions," *Physical Review Letters*, vol. 89 p. 080603, 2002.

∗ **R. Monaco, M. Aaroe, J. Mygind, R. J. Rivers, and V. P. Koshelets, "Experiments on spontaneous vortex formation in Josephson tunnel junctions," *Physical Review B*, vol. 74, p. 144513, 2006.**

The above three papers were a series of experiments aimed at testing the dependence of the defect number on the quench rate in annular Josephson junction superconductors. The cooling rate was successfully varied over four orders of magnitude and the trapping of flux was indeed measured. In the initial experiments good agreement was seen with their results and the Kibble-Zurek scenario prediction in 1D. However, later performed experiments which incorporated a better range of quench times were not in agreement.

3.5 Nonlinear Optical Systems

1. **S. Ducci, P. L. Ramazza, W. González-Viñas, and F. T. Arecchi, "Order Parameter Fragmentation after a Symmetry-Breaking Transition," *Physical Review Letters*, vol. 83, pp. 5210–5213, 1999.**

   The nonlinear optical system consisted of a liquid crystal light valve that is inserted into a feedback loop and is illuminated with a laser beam. In this configuration the light valve acts like an optical Kerr medium, corresponding to a phase retardation of the beam reflected from the front of the valve that is proportional the beam intensity on the rear face. The transition is induced by ramping the light intensity from below to above a critical threshold within a quench time τ_Q. Above the threshold intensity a self-sustaining diffraction pattern will be formed in the shape of stripes. Depending upon the intensity ramp rate, point defects will form in the 2D pattern. This system has the advantage that the intensity ramp of the laser can be controlled very easily. This experiment showed with good accuracy that the density of defects formed

were in very good agreement with the Kibble-Zurek scenario.

3.6 Fluids Undergoing the Conduction-Convection Transition

1. **S. Casado, W. González-Viñas, H. Mancini, S. Boccaletti, "Topological defects after a quench in a Bénard-Marangoni convection system," *Physical Review E*, vol. 63, p. 057301, 2001.**

   This system is based on the fact that as the rate of heating of the Bénard-Marangoni convection system is increased conductive heating is replaced by convective cells, in which rising plumes form a hexagonal pattern. When the system is rapidly heated many 'penta-hepta' defects form in the pattern. The plume pattern has points that have five and seven nearest neighbors instead of the standard six. In this system τ_Q can again be very easily controlled through the manipulation of the heating rate. The researchers saw a power law dependence of the defect density with respect to the heating rate, however the exponent was not in agreement with the Kibble-Zurek scenario. This was attributed to the fact that this system cannot be described by a simple scalar field, therefore the mean field theory is probably a poor approximation.

3.7 Spinor BECs

1. **L.E. Saddler, J. M. Higbie, S. R. Leslie, M. Vengalatorre and D. M. Stamper-Kurn, "Spontaneous symmetry breaking in a quenched ferromagnetic spinor Bose-Einstein condensate," *Nature*, vol. 443, pp. 312–315, 2006.**

   This work explored spontaneous symmetry breaking during a rapid quench across a quantum phase transition to a ferromagnetic state in a ^{87}Rb spinor condensate. The quench was performed by ramping a 2G magnetic field down to a value of 50 mG over 5 ms, which was then held at the final value for variable times. After the hold period the cloud was imaged using magnetization-sensitive phase contrast imaging [65]. With these methods the researchers were

able to observe the presence of spin textures, ferromagnetic domains, domain walls, and detect spin vortices. The latter can be considered a topological defect resulting from spontaneous symmetry breaking. This investigation did not attempt to make comparisons to the Kibble-Zurek scenario.

3.8 Significance of these Experiments on the Kibble-Zurek Scenario

The above experimental overviews show the difficulties present in verifying Kibble-Zurek type dynamics in physical systems. Specifically for superfluids, detecting the presence of vortices has proved to be problematic [66–68] and in cases where they were able to be detected, dependence of the vortices on the quench rate could not be sufficiently proven [69]. There is some evidence that supports power-law behavior between the density of defects and the quench rate [70, 71]. However, many questions still remain to be answered and a need exists for better tests of the Kibble-Zurek scenario; investigations in BECs may eventually provide one such check and will be the subject of the remainder of this dissertation.

CHAPTER 4

DEFECT FORMATION DURING THE MERGING OF INDEPENDENT CONDENSATES

4.1 Introduction

In reference [21] we demonstrated that the formation of vortices was possible through the merging of independent BECs. This Chapter will discuss this experiment, using it as a model for understanding the production of spontaneous vortices during the BEC phase transition and tying BEC phase transition dynamics to the general ideas presented in Chapters 1 and 2.

This chapter begins with a description of the experimental techniques used to cool a gas of ^{87}Rb atoms to condensation and discuss the imaging techniques used to collect the data. A brief overview of how the three-well trap was created will be followed by a synopsis of the three-well trap results. Comparisons between the 'proto'-condensate model of spontaneous vortex formation in BECs (as presented in Chapter 2) with the three-well trap experiment is presented.

4.2 Initial Experimental Conditions

4.2.1 MOT loading and Transfer

In our lab we have chosen to use a dual vacuum chamber, single magneto-optical trap (MOT) design to produce our condensates. A photograph of our vacuum chamber can be seen in Figure 4.1. The use of such a design requires the ability to magnetically transfer the atoms from the 'high' pressure MOT end of the chamber to the low pressure BEC end. The initial laser cooling stages of the ^{87}Rb atoms are performed at the MOT end of the chamber and consist of the loading of a diverging beam MOT over $\sim$ 12 s. At the end of our MOT load we have collected $\sim 3 \times 10^9$

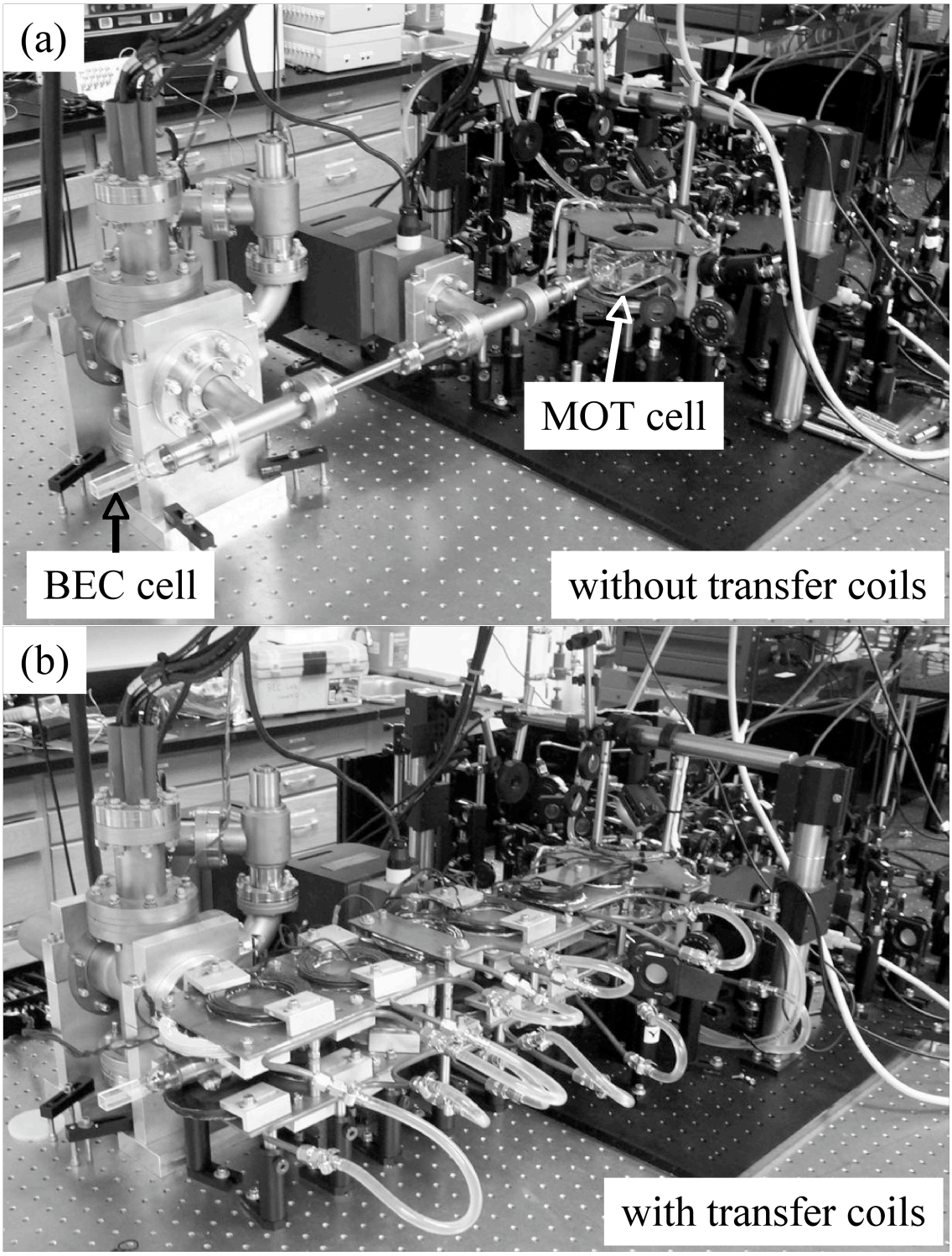

Figure 4.1: Photograph of the dual chamber vacuum system with and without the transfer coils. (a) shows both the high pressure MOT end of the chamber and the low pressure BEC end of the chamber. (b) shows the apparatus with the magnetic transfer coils present (photograph taken from [22]).

atoms that are at a temperature of few hundred μK. The MOT load is followed by a 60 ms compressed MOT (CMOT) stage and a 1 ms optical pumping stage of the atoms to the $5S_{1/2}$, $F = 1$ level of ^{87}Rb. The cooled and compressed atoms are then loaded into an axially symmetric 40 G/cm magnetic trap which is then ramped to 180 G/cm over 100 ms. With this arrangement only the low field seeking atoms, those that are in the $|F = 1, m_F = -1\rangle$ state, are able to be trapped. The atoms are then magnetically transfered from the MOT cell to the BEC cell by successively ramping on a series of anti-Helmholtz coil pairs. See [22] for more information on the transfer process. The transfer sequence takes $\sim$ 4 s to complete.

4.2.2 Initial evaporative cooling stage

Immediately after the transfer, the atoms are loaded into a time-averaged orbiting potential (TOP) trap [72] that initially has an instantaneous vertical magnetic field gradient of $B'_z = 300$ G/cm, and a $B_0 = 50$-G magnetic bias field that rotates in a horizontal plane at $\omega_{rot} = (2\pi) \cdot 4$ kHz or $\omega_{rot} = (2\pi) \cdot 2$ kHz (in our lab the vertical direction corresponds to the axial direction of our traps and also the direction of gravity). Radio-frequency (rf) forced evaporative cooling then proceeds over 72 seconds as B_0 decreases to 5.2 G, leaving a trapped cloud of atoms at a temperature just above the condensation critical temperature T_c. B'_z is then adiabatically reduced to 54 G/cm over 2 seconds, thereby weakening the harmonic-oscillator trapping potential against gravity. The measured frequencies for our experiments of spontaneous vortex formation (Chapters 6 and 7) are $\omega_r = 2\pi \cdot 7.81(9)$ Hz and an axial (vertical) trapping frequency of $\omega_z = 2\pi \cdot 15.3(2)$ Hz. Decreased trap frequencies cause a downward shift in the $|\vec{B}| = 0$ point of the trap due to the larger role of the gravitational potential on the atoms. This shift causes the atomic cloud position to shift 0.6 mm down along the vertical direction from the original tight trap position. In the lab, this sag has brought about the name 'sagged' trap for this configuration. It is at this point where we choose to manipulate the cloud to perform our experiments, thus discussions of the experiments that follow will start from manipulation of the cloud from this point.

4.2.3 Data Acquisition

All data taken in our experiment comes from the analysis of images taken of our atomic clouds. The main method used to search for the presence of spontaneous vortices was through near-resonant absorption imaging. The imaging procedure involves the sudden removal of the B_0 bias magnetic field, and the subsequent addition of a near 32.4 G magnetic field along the vertical direction. The B'_z magnetic field gradient is adjusted to near 60 G/cm (this value is adjusted day to day) to keep the atomic sample in the sagged position. With this configuration of magnetic fields, a very weak harmonic trapping potential is maintained along the vertical (axial) direction, while in the horizontal (radial) direction the field can be very weakly trapping or even anti-trapping. This allows the atoms to ballistically expand in the radial direction, while being held against gravity in the vertical direction. The atoms are held in the field for 56 ms of expansion, after which all fields are turned off and the cloud is able to expand in free space for an additional 3 ms. This last step is ensure that all fields are off during probing of the atomic cloud, therefore eliminating the effects of Zeeman shifts.

Due to our dual chamber configuration we have the ability to image along both the horizontal and vertical directions. A schematic of the imaging system can be seen in Figure 4.2. With both axes we have the ability to perform phase contrast and near-resonant absorption imaging. As stated at the beginning of this section the majority of our images are taken with absorption imaging along the vertical direction. Our near-resonant light is on the $|F = 2 \rightarrow F' = 3\rangle$ transition, however our condensates are created in the $|F = 1, m_f = -1\rangle$ state. In this scheme it is necessary to optically pump the atoms from the $|F = 1\rangle$ to the $|F = 2\rangle$ state using a short pulse of light (50 μs), that we call the 'repump flash.' The repump flash is tuned on resonance with the $|F = 1 \rightarrow F' = 2\rangle$ transition. Immediately after the repump flash, a 20 μs image is taken with the laser light intensity on the order of 1.6 mW/cm^2.

The absorption profile of the atomic density distribution is imaged onto a camera.

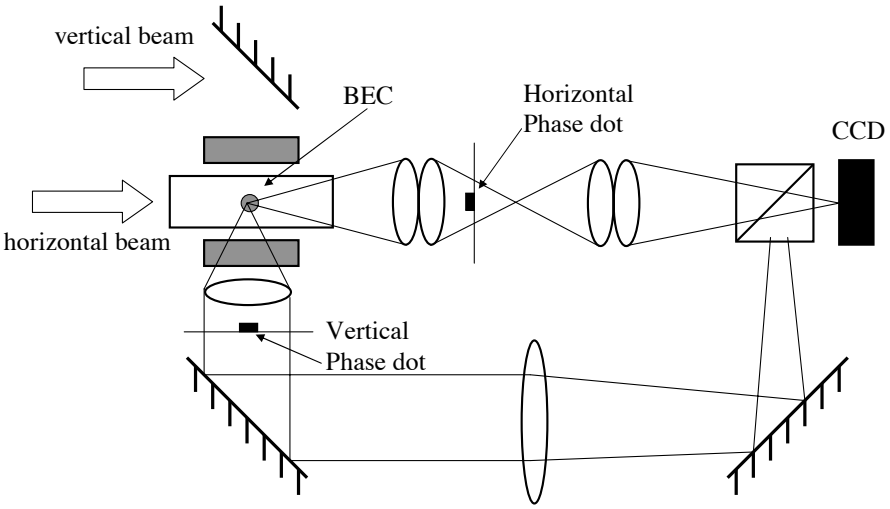

Figure 4.2: Schematic of the horizontal and vertical imaging systems. With both axes we have the ability to perform phase contrast and on-resonant absorption imaging. When using absorption imaging the phase dot is physically removed from the system. The optical magnification of both systems is ~ 5.4. (Image taken from [22])

For each data run we take a series of three images. The first image is of the atoms and the light field, the second with just the light field, and the third a dark frame with no light present. The images are processed using a MatLab fitting routiine as discussed in Section 4.5.2 in [22].

In our images, lighter shades represent higher optical depth, proportional to the integrated column density along the z-direction line-of-sight. A typical expanded vertical absorption image can be seen in Figure 4.3 (a). As stated in Section 2.5.2, a clear vortex core appears as a hole in the density distribution[73] of the BEC. A very clear example of this can be seen in Figure 4.3 (b).

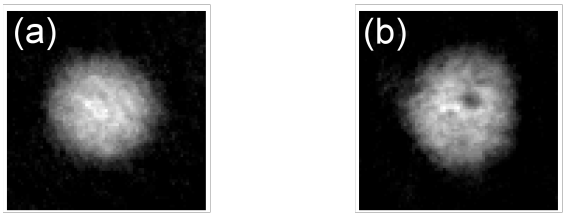

Figure 4.3: Typical expanded vertical absorption images. (a) An typical image of an expanded BEC. Here lighter shades represent the presence of atoms (higher optical depth). (b) a sample image of a cloud with a vortex present in the sample. The vortex appears as a dip in the density distribution.

4.3 The Three-Well Trap

4.3.1 BEC formation with an optical potential

By utilizing the optical dipole potential $U = \frac{\hbar\Gamma}{8}\frac{I/I_{sat}}{\Delta/\Gamma}$ (where Γ is the natural linewidth of the atomic species, I the laser intensity, I_{sat} the saturation intensity of the atomic species, and Δ the detuning) we were able to transform the initially harmonic potential to one in which there are three local potential minima as is shown in the contour plot seen in Figure 4.4 (a). This was accomplished by illuminating a binary mask* as seen in Figure 4.4 (b), with a blue-detuned ($\lambda = 660nm$) Gaussian Laser beam and imaging this mask onto the minimum of the harmonic trap. The

*See Section 5.6 for a description of how the 'Y' mask was made

intensity profile of the beam can be seen in Figure 4.4 (c); a schematic of the experimental setup can be seen in Figure 4.5. The optical potential was ramped on during the 2 second ramp down of B'_z. A final 10 sec rf-evaporation step commenced thus taking the sample to condensation in the three-well trap.

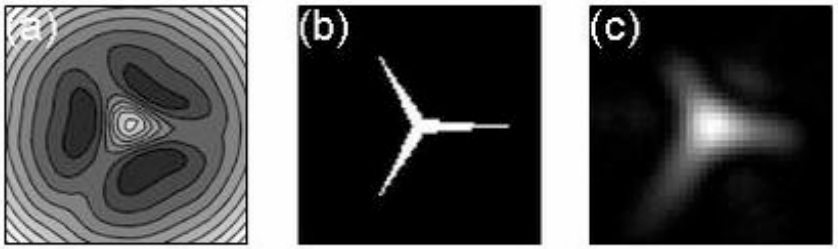

Figure 4.4: (a) Potential energy contour showing a horizontal slice through the center of our three-well trap, representing the addition of the harmonic TOP trap with the measured intensity profile of the optical barrier beam, scaled to a potential energy. (b) The binary mask profile used to create the optical barrier, where white represents the transmitting area. (c) An image of the actual optical barrier profile in the plane of the BEC. The size of images (a) and (c) are 85 μm $\times$ 85 μm

4.3.2 Formation of independent BECs

Condensing in the trap described above allows for the creation of three initially independent condensates each of which has its own quantum phase. The condensate merging was controlled in three different scenarios. The first two control sequences were performed with the barrier height high enough to prevent the three condensates from knowing the others existed. The merging was performed by either ramping down the barrier adiabatically (slow ramp) or non-adiabatically (fast ramp). For the third case the barrier height was weak enough to allow the condensates to merge during their growth.

The fluid flow direction during the merge is dependent upon the relative phase differences between the three condensates as described in Section 2.5.2. These three condensates will also merge in a manner that minimizes the energy very similar to that of proto-condensates. Here again the possibility exists for the trapping of a

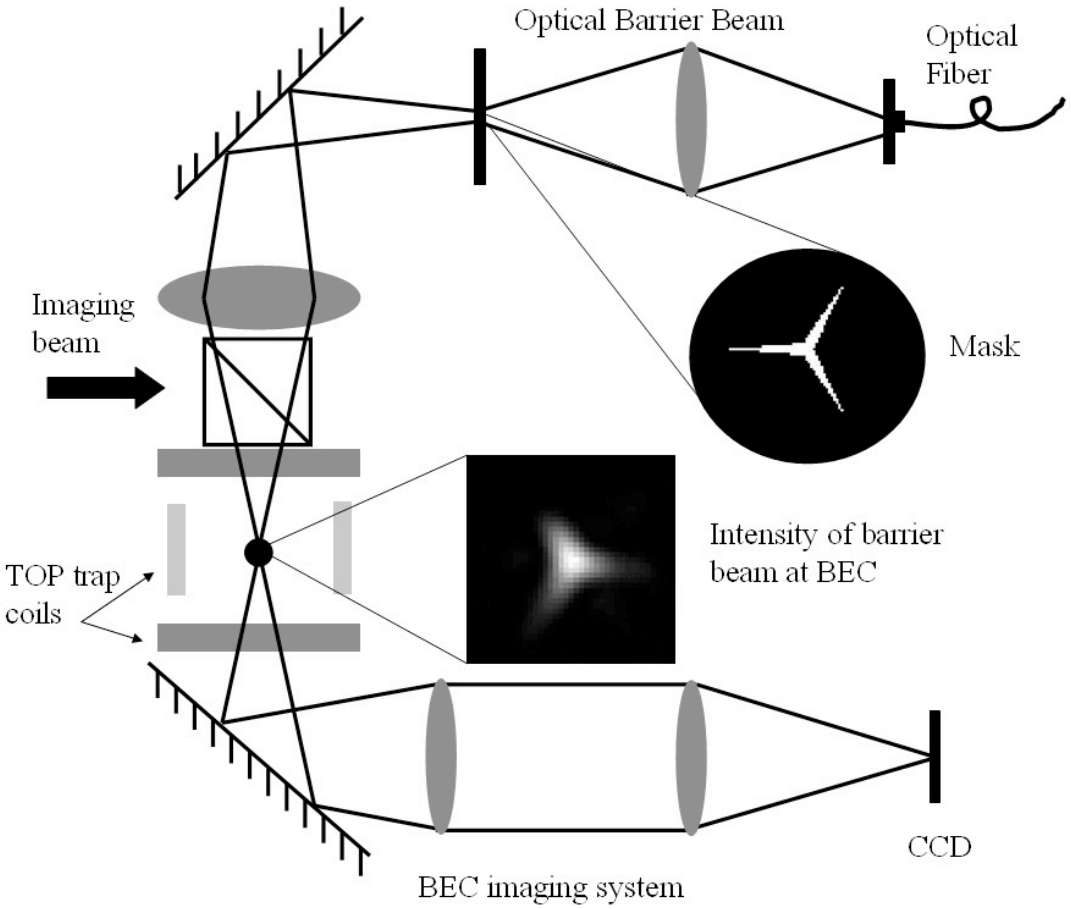

Figure 4.5: Schematic of the experimental setup. The optical barrier beam is coupled from an optical fiber and focused onto the binary transmission mask. The beam that passes through the binary transmission mask then passes through a polarizing beam-splitter cube and imaged by one focusing lens onto the plane of the BEC; the intensity of the optical barrier beam at the plane of the BEC is shown. The vertical imaging beam passes through the other port of the polarizing beam-splitter cube and passes through the BEC vertically, then gets imaged onto the CCD camera. The horizontal imaging system is not shown. Caption taken from [22].

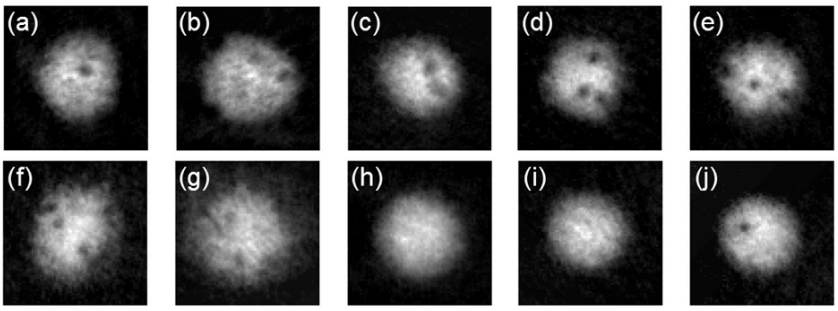

Figure 4.6: (a),(b) 170–μm wide images showing vortices naturally occurring in condensates created in a trap with a $k_B\times 7$ nK barrier. (c)–(h) Images obtained using various barrier energies. (i),(j) BECs created without an optical barrier.

2π phase loop around the three condensates. Similar arguments to those used in Section 4.4 can be used here and it is expected that vortices could be produced in this configuration. Indeed the presence of vortices was detected in our condensates using this technique as is illustrated in Figure 4.6. One of the main results of this experiment was the proof that vortex (topological defect) generation is possible through the merging of initially isolated and uncorrelated condensates.

4.4 How does this aid in the description of spontaneous vortices in BEC?

Reflecting back to the ideas presented at the end of Chapter 2, it can be immediately seen how the three well trap experiment can be viewed as a model/test of the fundamental principles set forth by the Kibble-Zurek scenario. The distinct difference being that in the three well case the dynamics of the merging of the three condensates can be completely controlled. Whereas, in the merging of the 'proto-condensates' the dynamics of the merge is completely uncontrolled and much more complicated to describe due to the possibility of more than three regions being able to merge together. Nevertheless, this experiment provided insight into the ability to form topological defects through the merging of initially uncorrelated BECs.

CHAPTER 5

COMPUTER-GENERATED HOLOGRAMS FOR BEC

5.1 Introduction

The computer-generated hologram (CGH) has found a wide range of uses since the advent of binary CGHs by Lohman, Brown and Paris in 1966 [74] (for a brief history of Lohman's acheivement see his article in Optics and Photonics News [75]). They have been applied to optical testing of optical elements [76], optical lithography and fabrication [77], optical tweezers [78], and the list goes on. A little-explored application of the CGH is in manipulationg ultra-cold atomic gases. The use of computer-generated holograms in BEC experiments could be far ranging. CGHs would provide the ability to optically manipulate the condensates in a myriad of possibilities. As we began our work on the Three Well experiment the idea was proposed to use a CGH to generate the Y pattern for the triple well trap. We had investigated the possibility of using a spatial light modulator (SLM) to generate our desired design, however these prove to be expensive and have many drawbacks. Not long after we had decided to explore the possibility of using a hologram, I took part in professor Tom Milster's Computer Generated Holography Workshop at the College of Optical Sciences. During this workshop I was introduced to a fabrication technique called high-speed maskless grayscale lithography that their group was developing for production of CGHs. This method employed the use of a maskless lithography tool (MLT) to write the CGH into a photoresist polymer. We approached Tom about using the MLT for our CGHs and he was more than willing to help our efforts. I also had the benefit of taking professor William Dallas' OPTI 627 Computer Generated Holography class. Thus began our study of the utility of CGHs for manipulating BECs.

The remainder of this chapter will outline the methods used to generate the

CGHs and provide details about the high-speed grayscale lithography tool process. An overview will be given of the procedures used to prepare the polymer photoresists for use on the MLT. Many iterations of CGHs were produced, each with multiple changes to improve quality. Some of the major drawbacks to using CGH in BEC experiments will also be presented. These drawbacks were what ultimately led us to use a direct mask approach in our three well experiment. The direct mask was also produced on the MLT and details of how these masks were constructed will be given. The utility of the MLT is far ranging. Not only were we able to create CGHs and the direct mask but it also allowed us to generate phase dots for use in our phase contrast imaging setup. An overview of the methods used to create the phase dots will be presented.

5.2 Computer Generated Holograms

As stated in the Section 5.1, the main advantage of a computer-generated hologram is that the object to be encoded in the hologram does not have to be a real physical object. Therefore, as long as the object can be programmed, a CGH can be generated. The only real limitation being the feasibility of fabricating the CGH. For our experiments we wanted to create a Y pattern that had a peak intensity at the intersection of the three arms and trailed off nearly exponentially along each arm. An image of the desired pattern is shown Figure 5.1.

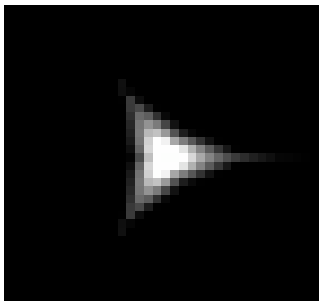

Figure 5.1: The generated Y pattern used to construct the CGH. The Y has the following characteristics: the peak intensity is at the intersection of the three arms, with a near exponential fall off of intensity along each arm respectively.

The ability to construct CGHs is predicated on the fact that a lens is a Fourier transformer. The concentration of the work done in computer-generated holography is on the telecentric image system or the '4f' system. This system is composed of two thin lenes of equal focal length spaced at twice their focal lengths. The input plane is located one focal length in front of the first lens, while the output plane is located one focal length behind the second lens. The Fourier plane is located at the intermediate focal plane between the two lenses. A schematic of a '4f' system can be seen in Figure 5.2. Generally speaking, placing the object at the input plane and Fourier transforming places the transform of the object at the intermediate plane. Inverse Fourier transforming returns the resulting image at the output plane. Essentially, this is how the 'idea' CGH is constructed, with the Fourier transform of the input object being the CGH. Of course in practice things are not this simple, the subject of the next section will be to lay out the necessary steps taken to construct the CGH.

5.2.1 General procedure for producing CGHs

Computer generated holography is predicated on Fourier math concepts. The Fourier transform of an object returns a complex number, $\mathcal{F}\{Object(x))\} = A(\xi)e^{-i\theta(\xi)}$, where A provides amplitude information and θ provides phase information. The many types of CGHs that can be produced are based on manipulating the amplitude, phase information or a combination of the two. For our holograms we focused on using the phase information only. The main style of hologram we designed is known as a phase only, phase hologram or a kinoform. Kinoforms are designated phase only, phase holograms because the CGH is generated by normalizing the amplitude information while maintaining all of the phase information (the phase only part). The phase part is because these holograms are phase holograms. The second type of hologram we tried was the binary phase hologram. These holograms are generated similarly to the kinofrom, however once the kinoform was produced the phase was limited to be either 0 or π.

The following is a list of the steps taken to produce both the kinoform and the

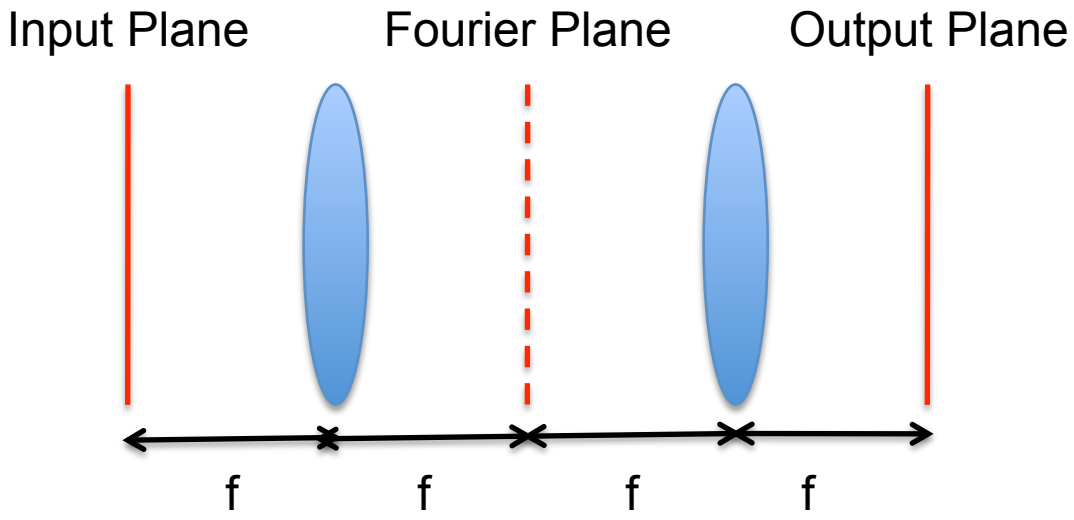

Figure 5.2: The telecentric or '4f' imaging system. The '4f' system consists of two equal focal length lenses spaced by twice their focal lengths. The front focal plane is located at the front focus of the first lens, while the back focal plane is located at the back focal length of the second lens. The Fourier plane is located at the midway point between the two lenses. This type of imaging system is the one most widely modeled when constructing computer-generated holograms

binary phase holograms. Where applicable, I will point out where the two differ.

1. Create a 256 gray level colormap. This is done for the purposes of writing the CGH on the MLT, see Section 5.3 for details.
2. Load the Object
3. For the binary phase case only, shift the object off axis. This is necessary to prevent the twin images from overlapping one another.
4. Add a random phase diffuser to the object. This serves to spread the light field over the entire Fourier plane, without it the light would be very concentrated near the center of the Fourier plane.
5. Optimize the random phase using the Gerchberg-Saxton Algorith (see Section 5.2.2 for details).
6. Normalize the Fourier transform amplitude and retain the phase information.
7. For the binary phase case only, limit all phase values to either 0 or π.
8. Display the CGH.
9. Reconstruct the image by inverse Fourier Transforming. This will provide a test for how well the CGH can reproduce the original image.

Generated CGH's for both the kinoform and binary phase cases as well as the reconstrected images can be seen in Figures 5.3 and 5.4, respectively.

5.2.2 The Gerchberg-Saxton algorithm

The initial intent of the Gerchberg-Saxton algorithm was for phase retrieval from two intensity measurements [79, 80]. Here it is used to optimize the initially applied diffuser (step 5 above) to produce the best estimate of the initial object. The procedure goes as follows:

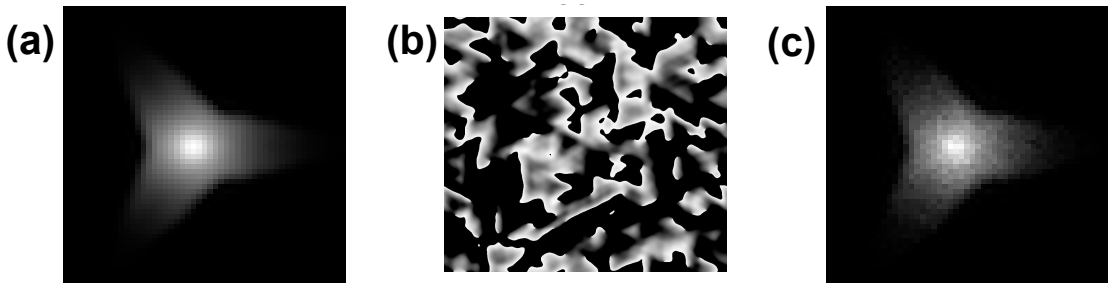

Figure 5.3: Example computer generated images of **(a)** the object **(b)** the kinoform CGH, and **(c)** the reconstructed object.

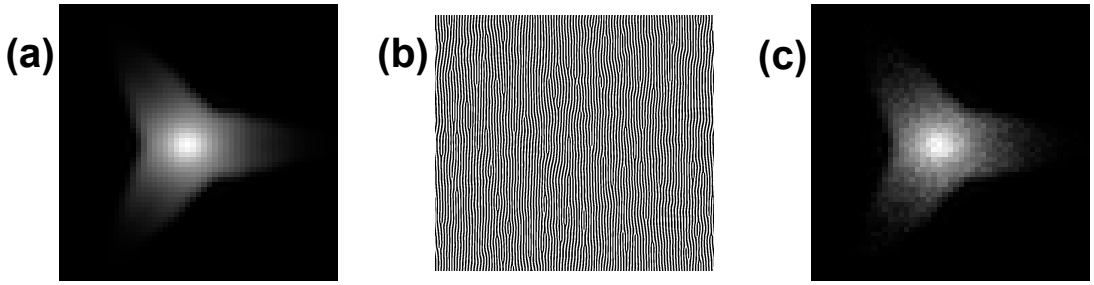

Figure 5.4: Example computer generated images of **(a)** the object **(b)** the binary phase CGH, and **(c)** the reconstructed object.

1. Fourier transform the object with the applied diffuser.
2. Replace the modulus of the resulting computed Fourier transform with the measured Fourier modulus to form an estimate of the Fourier Transform
3. Inverse Fourier transform the estimate of the Fourier transform.
4. Replace the modulus of the resulting computed image with the modulus of the measured object to form a new estimate of the object.
5. Repeat steps 1–4 multiple times (for this work it was repeated 100 times).

5.3 The Maskless Lithography Tool (MLT)

5.3.1 How the MLT works

The Maskless Lithography Tool (MLT) is a device operated by the Milster Group in the College of Optical Sciences at the University of Arizona. The MLT is a raster scanning device that allows for the printing of binary and greyscale photoresists without the need of a photomask, which are expensive to produce. A picture of the tool can bee seen in Figure 5.5.

A multi-faceted polygon is used to raster a UV laser beam, $\lambda = 360$ nm, across the sample in one particular direction; this is a fast scan. A linear translation stage is used to move the sample orthogonal to raster direction; this is a slow scan [81]. In the maskless lithography field this type of writing has been called 'Flying Spot' raster scanning [82].

The desired phase steps of the CGH are written into the resist by modulating the intensity of the laser beam as it is scanned. The machine is interfaced with a LabView program that uploads a 256 level grayscale bitmap that represents that CGH to be written. Each gray scale level corresponds to a particular laser intensity, which directly influences the photoresist height after processing. The laser intensity has been linearized to the resist's response, to produce a linear gradient in step size. The resists used to produce the CGHs are Shipley 1805 or 1822 depending upon

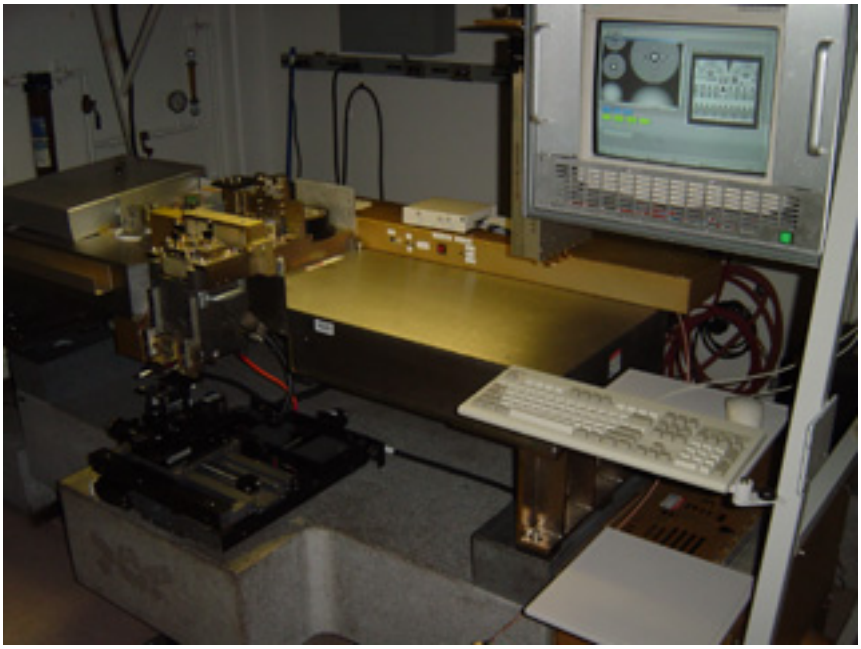

Figure 5.5: Maskless Lithography Tool (MLT)

the desired CGH characteristics. These resists are positive resists (see Appendix C for the resist specifications). With a positive resist the area that is exposed to light becomes soluble to the resist developer and the area that remains unexposed remains insoluble. Therefore, areas exposed to high intensity will produce low resist thickness regions and vice versa. All of this allows the user to create 256 level phase steps for the kinoform, where zero phase corresponds to the lowest thickness region and 2π corresponds to the largest thickness.

The maximum number of pixels available to the image is 12k X 12k, with a writing pixel size of $\sim$2.5μm, this gives a final image area of 30 mm X 30 mm. The total write time for a 30 mm X 30 mm sample is amazingly fast at 15 sec. Currently, work is being performed to allow for stitching of large bitmaps for the final printed image, which will allow for larger final printed images.

5.4 Preparing the samples

The samples to be printed consist of a glass substrate coated with the above mentioned photoresist. For this work 30 mm X 30 mm glass slides are cut from a common microscope slide. These substrates are then cleaned using the following procedure:

1. Wearing rubber gloves, rub surfaces of slides with fingers in a 2% solution of micro-90 cleaner in deionized water, rinse in deionized water.
2. Clean in an ultrasonic bath with a 2% solution of micro-90 cleaning solution in deionized water for 30 minutes.
3. Rinse in an ultrasonic bath with deionized water for 30 minutes.
4. Dry thoroughly with compressed air.
5. Clean with acetone in an ultrasonic bath for 30 minutes.
6. Dry thoroughly with compressed air.
7. Clean with methanol in an ultrasonic bath for 30 minutes.
8. Use compressed air to dry thoroughly.
9. Bake in an 300 °F oven for 2 hours.

I prefer this method over an acid wash mainly because I dislike handling acid, it may be a slightly longer process but in the end I find it to equal to an acid wash.

After the samples are cleaned it is time to apply the resist to the samples. The two resists used are chemically the same polymer material but are of different concentrations of polymer to solvent and therefore have different viscosities. The viscosity plays a very important role in determining the resist thickness after deposition, so it is important to know which resist is able to produce the desired height. Using the equation $\delta = 2\pi(n_2 - n_1)d$ where δ is the desired phase shift, n_2 the refractive

index of the phase retarder, n_1 the refractive index of the non-retarding medium (in our case air), and d the thickness of the phase dot, the maximum resist height is calculated by determining the thickness that corresponds to a 2π phase shift for the wavelength of light being used to reconstruct the hologram (see Appendix C for index of refraction values for the resist).

Spin coating is the preferred method of depositing the resist. I will not provide a full description of spin coating methods here but instead refer the reader to reference [83]. I will describe the general procedure used to make a 1μm thick sample. The glass substrate is loaded onto the spin coater chuck and flooded with the resist. The spin coater then ramped the sample to 3000 rpms over six seconds. It was kept at 3000 rpm for an additional 30 seconds in order for all of the resist solvent to evaporate. After the 30 second hold the spin coater is shut off and the sample is taken to a hot plate at 150 °C and left to dry for 15 sec. This final bake is used to expel excess solvent remaining after the spin and serves to 'harden' the spun layer. A cross-sectional image of the finished sample can be seen in Figure 5.6.

Figure 5.6: Cross-sectional view of the spin coated sample before printing.

I put 'harden' in quotes as a caution. These samples are extremely susceptible to scratches and therefore great care must be taken when handling them. Also, they are very sensitive to UV light so it is advised to keep spun samples covered in plastic cases and out of normal fluorescent light. In most cases the Milster group placed UV filters over their fluorescent bulbs or are using special UVless bulbs in their labs, but it is still a good idea to keep the samples in the dark as much as possible before printing. I also caution that the spin rates and times stated above are rough

estimates and highly subject to change. Spin coating is very dependent upon many conditions such as climate (mainly humidity), the age of the resist, cleanliness of the substrate, etc. It is often the case that the parameters that produced a 1μm thick sample on one particular day could produce a 1.25μm thick sample the next day. When spinning new samples it is always important to measure the thickness of the resist on the Veeco profilometer.

After the samples have been dried they are ready for use on the MLT. Once the CGH has been printed, it is developed in MICROPOSIT MF–319 developer for 1 minute, rinsed in DI water and blown dry with compressed air. A cross-sectional depiction of a printed CGH can be seen in Figure 5.7. An examination of the CGH under a microscope will allow for the determination of how well the MLT has printed the desired pattern.

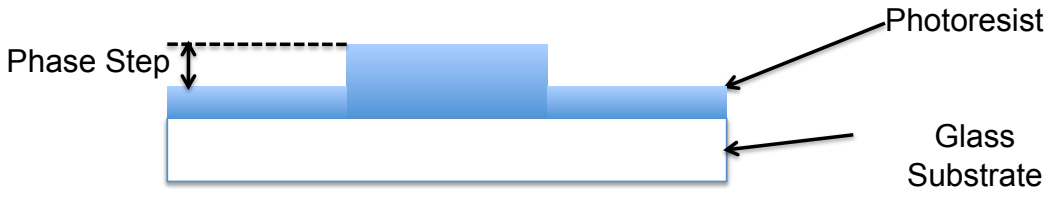

Figure 5.7: A cross-sectional view of a printed CGH. The height of the photoresist layer will produce the desired phase shifts in order for the CGH to reconstruct the image.

5.5 Drawbacks of CGHs Generated Using the MLT

An example experimental reconstructed image of a hologram fabricated using the MLT is shown in Figure 5.8. As seen from the image one of the biggest challenges of this method is to combat the presence of speckle. Speckle is inherent in the hologram due to the addition of the random phase at the beginning of the generation process. It can be expected that within the random phase diffuser the possibility exists for a 2π phase winding to occur around any closed path around pixel values in the diffuser. These regions will produce optical vortices or speckle. Attempts were made

to reduce the speckle by adding a spherical phase and by using a search algorithm to find the areas in which the 2π phase loops existed and adjusting the phase values to eliminate the winding. However, these methods never proved to reduce the amount of speckle in the reconstructed images.

Another problem has been an issue of size. The MLT at the time could only produce holograms that were 30 mm square. Governed by diffraction theory, this limited the size of hologram at the condensate with feature sizes being much too large for use in the experiments. In most cases for the Y CGHs the $1/e^2$ drop offof the intensity from center was on the order of or larger than the size of the condensate. Since this work was completed the Milster group has modified the system to make larger holograms, which could in principle aid in producing feature sizes much more in line with what is needed to be able to manipulate the BEC.

5.6 Preparing the 'Y' mask

The binary'Y' masks used in the three well experiment were created using the MLT. The binary masks are written on chrome coated slides purchased from Telic Company (*http://www.telicco.com/*). These slides are multicoated samples on glass substrates; the bottom layer being chrome with the top layer photoresist. A cross-sectional view of the sample can be seen in Figure 5.9.

The chrome layer is processed in an acid based developer that etches away the chrome layer; an exposed chrome region will therefore become a clear aperture after it is processed. The photoresist acts as a protectant to the chrome layer. Thus, the creation of the binary masks is a two step process. The first step involves using the MLT to write the desired pattern in the photoresist. The MatLab generated bitmap was 1600×1600 pixels and contained four Y patterns at the corners. A blown up version of one of the 'Y' patterns can be viewed in Figure 5.10. Once loaded into the MLT LabView program, the bitmap was enlarged a factor of 3. This produced the correct sized Y for our optical system. The MLT laser intensity was set at 250 mW for exposure. The written sample was developed using the same method as

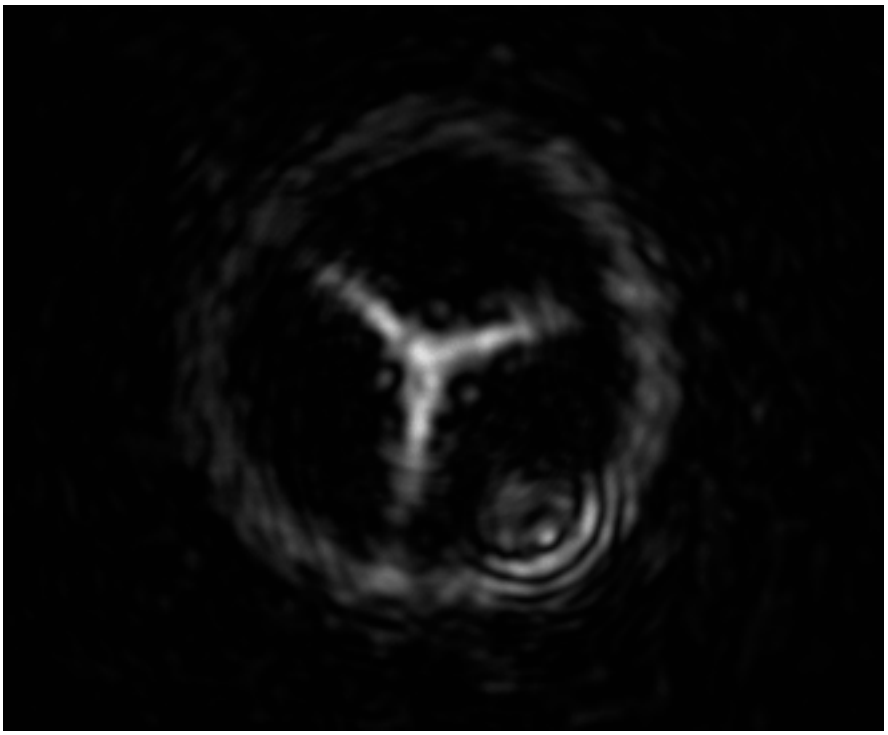

Figure 5.8: Experimental reconstructed image of a CGH fabricated with the MLT. As with all of the reconstructed images generated with this method it is very mottled due to speckle. The CGH pattern used to produce this image was done by the DeMarco group at the University of Illinois Urbana-Champagne, the physical CGH was constructed using the MLT.

Figure 5.9: The binary mask slides are multilayered samples. The glass substrate is coated with a chrome layer and the chrome layer is coated with a layer of photoresist.

the CGHs. Once the photoresist has been processed, the sample is placed in the acid developer for 2 minutes. The acid developer was composed of a solution of 165 grams of Amonium Nitrate dissolved in 42 mL of perchloric acid and 959 mL of deionized water. The sample was then rinsed with DI water and blown dry with compressed air. The masks were then examined under a microscope, checking for defects.

Figure 5.10: A blown up version of one of the four Y patterns generated on the bitmap.

5.7 Phase Dots

The use of phase contrast imaging in our experimental setup necessitates the need to fabricate a phase dot. Phase contrast imaging relies on interference between the light refracted by the BEC and the un-refracted lght. This is accomplished by focusing the un-refracted light through a phase retarding medium, thus producing a phase shift. In many labs the phase dot is constructed using magnesium fluoride deposited on a substrate, the techniques of which are not easily performed. In our lab we utilized the MLT to construct our phase dots. The utility of the MLT provided us the means to make phase dots of any size, shape, and phase shift. Through experimentation we found that a $5\pi/2$ phase shift gave us the best signal to noise for our images. The resist has a refractive index of $\sim$1.625 at the imaging wavelength of 780 nm corresponding to a phase dot thickness of 1.5 μm. Thus it is necessary to spin coat a sample of thickness 1.5 μm. The MLT laser power is set at 350 mW in order to take the resist down to bare glass around the phase dot. The phase dots were developed using the same techniques described for the CGHs.

A square pattern phase dot was chosen because this provides the means of distinguishing the phase dot from residual resist left on the substrate after development. Several different sized phase dots were produced, however it was found that 150 μm $\times$ 150 μm works best for the vertical path, and a 100 μm $\times$ 100 μm is sufficient for the horizontal path. A MatLab generated bitmap image of the phase dot can be seen in Figure 5.11. The code for producing the phase dot can be seen in Appendix B. The code shown is for a 150 μm square phase dot, however in the code it can be seen that the limits are set to produce a 50 μm square dot. The extra factor of 3 is produced by the MLT Labview code, however much has been changed about the MLT code since phase dots were last fabricated so it is unclear whether this is still a necessary step. A similar scaling was used to produce the 100 μm square phase dots.

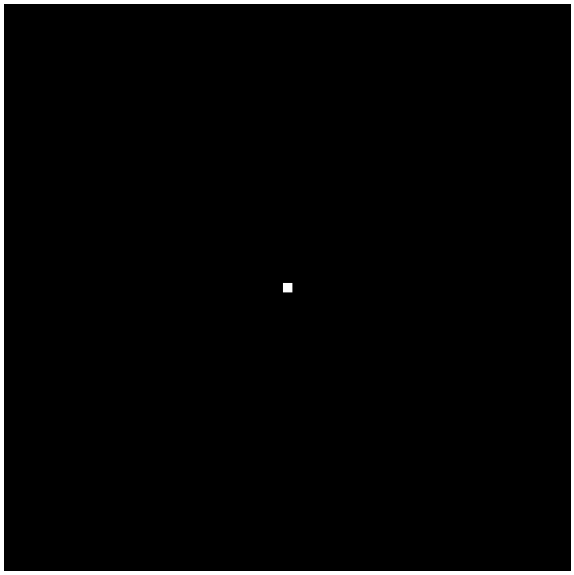

Figure 5.11: Example bitmap image of a phase dot used to generate dots on the MLT. This particular phase dot produced a 150 μm $\times$ 150 μm square phase dot. For viewing purposes the contrast has been reversed.

CHAPTER 6

THE BEC TRANSITION IN A HARMONIC TRAP

6.1 Introduction

In Chapters 1 and 2, the concepts of spontaneous symmetry breaking and topological defect formation for continuous phase transitions were introduced. It was also suggested that the spontaneous formation of topological defects, such as vortices, is common in continuous phase transitions [1]. Chapter 3 presented an overview of the various systems in which spontaneous defect formations has been studied. However, in many of these systems the microscopic dynamics of defect formation have been difficult to investigate, particularly the thermal-to-superfluid phase transition [84–86]; in superfluid ^{4}He for example, vortex formation may be attributable to inadvertent convective stirring mechanisms [87], significantly complicating spontaneous vortex formation studies. Because of their amenability to manipulation and probing, Bose-Einstein condensates (BECs) offer a unique experimental opportunity for studying microscopic details of phase transitions and topological defect formation. Furthermore, these superfluid systems can be described by microscopic theories [88–93] that incorporate quantum fluctuations and atomic interactions. Although some theoretical estimates have predicted that vortices should be spontaneously formed in the BEC transition [11, 50], until now they have not been observed; it has even been suggested that their spontaneous formation may be energetically unfavorable [92, 94].

In this chapter I will present an experimental and theoretical study* of BEC growth from evaporatively cooled atomic gases held in a harmonic potential, providing the first observations and statistical characterization of spontaneous vortex formation in the BEC transition. Of particular interest is the remarkable quantita-

*Theoretical work was performed by our collaborators Matthew Davis and Ashton Bradley at the University of Queensland, Brisbane, Australia

tive agreement between our experimental and theoretical results.

6.2 Methods for the Harmonic Trap

6.2.1 Final evaporative cooling stage.

We advance towards condensation with the pre-cooled gas in the sagged trap as described in Section 4.2.2. For our data collection the typical final stage of our cooling cycle, which I will designate as "Quench A", involves a continuous 6-s ramp of a radio-frequency (rf) field that induces the evaporative cooling of the atom cloud from 70 nK to 20 nK, with T_c ∼42 nK, to create condensates of $N_c \sim 5 \times 10^5$ atoms. The second approach, which will be designated as "Quench B", involved replacing the continuous rf evaporative cooling ramp with a sudden rf jump to a final rf value, followed by a hold of the atomic sample in the trap before release and imaging. In this situation $T_c \sim 35$ nK and the final condensate number is $N_c \sim 3 \times 10^5$ atoms.

6.2.2 Theoretical techniques

As mentioned in the introduction, the theoretical and numerical work was performed by Davis and Bradley at the University of Queensland, Brisbane Australia. The comparison between our experimental work and the numerical simulations provide a sound basis from which we can collaboratively formulate an understanding of the dynamics of the BEC phase transition. Therefore, it is necessary to include a discussion of the numerical studies in tandem with our experimental studies. The following descriptions of theoretical and numerical methods contain modified excerpts from a manuscript describing the results of our collaborative experimental and theoretical work. These excerpts are denoted with asterisks (*).

The dynamics of the fully formed condensate approximately obey the nonlinear Schrodinger equation known as the Gross-Pitaevskii equation (GPE) [29, 30]

$$(-\frac{\hbar^2}{2M}\nabla^2 + V(\hat{r}) + g|\psi(\hat{r})|^2)\psi(\hat{r}) = i\hbar\frac{\partial\psi(\hat{r})}{\partial t} \text{ [29, 30]} \tag{6.1}$$

where M is the mass of a single particle, V is the external potential, g is the coupling

constant, and ψ the condensate wave function. The majority of the numerical work that has been performed on condensate dynamics thus far have been modeled after this equation [95]. The GPE must be modified to include higher order modes from which the condensate can grow. The Stochastic Gross-Pitaevskii equation (SGPE) [90] has this capability. The SGPE also incorporates coupling of the BEC to a thermal bath and density and phase noise. In this research our collaborators employed the SGPE to simulate the dynamical processes involved during condensate growth.

Stochastic Gross-Pitaevskii theory.*

The condensate and low energy portion of the trapped gas is denoted with the field $\alpha(\mathbf{x}, t)$. Defining the Gross-Pitaevskii operator

$$L_{\rm GP} = -\frac{\hbar^2}{2m}\nabla^2 + V(\mathbf{x}) + g|\alpha(\mathbf{x}, t)|^2, \tag{6.2}$$

the equation of motion for the field is

$$d\alpha(\mathbf{x}, t) \;=\; \mathcal{P}\left\{-\frac{i}{\hbar}L_{\rm GP}\alpha(\mathbf{x}, t)dt + \frac{G(\mathbf{x})}{k_B T}(\mu - L_{\rm GP})\alpha(\mathbf{x}, t)dt + dW_G(\mathbf{x}, t)\right\}$$

which has been derived from first principles using the Wigner phase-space representation [90]. The first term on the right describes unitary evolution of the classical field according to the Gross-Pitaevskii equation, the second term represents growth processes, i.e. collisions that transfer atoms from the thermal bath to the classical field and vice-versa, and the form of $G(\mathbf{x})$ may be determined from kinetic theory [96]. The third term is the complex noise associated with growth satisfying $\langle dW_G^*(\mathbf{x}, t)dW_G(\mathbf{x}', t')\rangle = 2G(\mathbf{x})dt\delta\ (\mathbf{x} - \mathbf{x}')\delta(t - t')$. This form of the noise correlation is mandated by the fluctuation-dissipation theorem. The projection operator $\mathcal{P}$ restricts the dynamics to the low-energy region [88, 91] defined by all harmonic oscillator modes with energy $E_{\rm cut} < 40\hbar\omega_r$ for these calculations, with occupation at the cutoffof $N(\epsilon) \sim 3$. For typical experimental parameters this method is accurate from slightly above the critical temperature to colder temperatures where there is still a significant thermal fraction [97, 98]. A spatially constant dimensionless

rate $\gamma = \hbar G(\mathbf{x})/k_B T$ is chosen to provide coupling to the high energy component; in principle this is specified by a quantum Boltzmann integral [96], but here it is treated as an experimental fitting parameter for the condensate growth rate; it is never more than a factor of two different from the result of Bradley *et al* [96]. Previous theoretical work on evaporative cooling suggests that discrepancies between theoretical and experimental values of γ of this order are typical [54, 55].

6.3 Harmonic Trap Results

6.3.1 Experimental Procedure

The following procedure was followed for the harmonic trap experiments:

1. Produce a BEC.
2. Release the BEC from the trap and image.
3. Look for the presence of vortices.
4. Repeat items 1–3 many times.
5. Determine vortex formation statistics.
6. Compare experimental statistics with the numerical simulations.

6.3.2 Experimental Results

Plots of condensate number versus time for both Quench A and B are shown in Fig. 6.1, with the measured temperature trajectories shown in the inset. By performing a linear fit to the temperature trajectory data seen in the inset of Figure 6.1 we calculate that our quench rate $1/\tau_Q$ is ~ 0.140 Hz for Quench A and is ~ 0.182 Hz for Quench B. Based on the prescription outlined in Section 2.3, an estimate of the coherence length near the condensation critical point can be obtained. For Quenches A and B the coherence length was estimated to be $\xi \approx 0.7\mu$m and $\xi \approx 0.6\mu$m, respectively . This is about a factor of ~ 5 *smaller* than the radial harmonic oscillator

length $a_r \equiv \sqrt{\frac{\hbar}{m\omega_r}} \sim 3.8$ μm (where m is the mass of a ^{87}Rb atom) that nominally characterizes a condensate radius for small atom number. This suggests that the formation of 'proto'-condensates during the condensation process is possible and based on the discussion set forth in Section 4.4 vortices can be created during the initial growth stages of the condensate in the experiment.

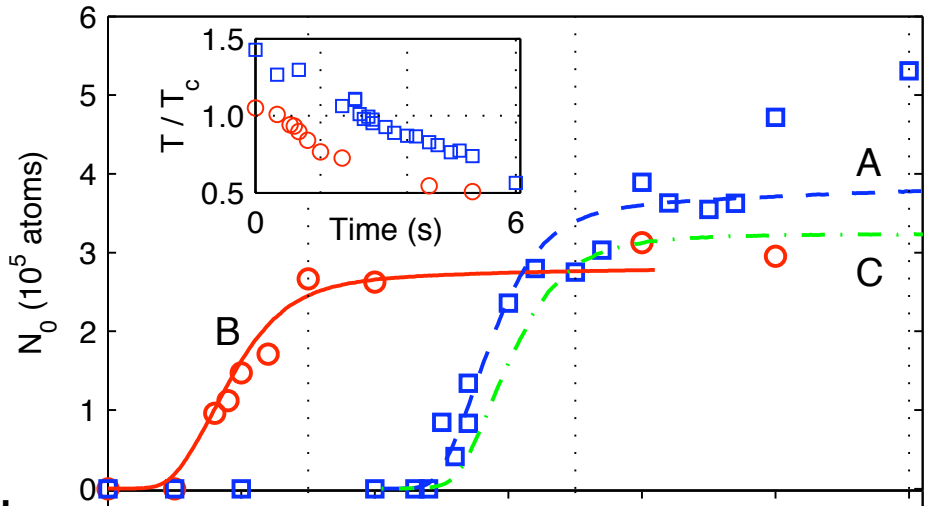

Figure 6.1: Condensate number versus time. The blue squares (red circles) indicate the number of atoms in the condensate versus time for the experimental data for Quench A (B), with the solid lines corresponding to the simulation. The inset shows the experimentally measured temperatures for Quenches A and B. The vertical dotted lines indicate the observation times for which statistics are gathered for the theoretical case.

As stated in Section 4.2.3 and briefly summarized here, to look for the presence of vortex cores in BECs created in the laboratory, the trapping potential was suddenly removed at the end of the 6-s evaporative cooling ramp of Quench A (the BEC starts to form ∼2.5 s into this quench), or ∼1.5 s after the rf jump for Quench B (the BEC starts to form ∼0.5 s into this quench). The BEC was allowed to ballistically expand before imaging the atom cloud along the z direction. Vortex cores well-aligned with the z axis appear as holes in the column-density distribution, as shown in Fig. 6.3 (a). It is emphasized that the experimental procedure does not impart net angular

momentum to the atomic cloud, such as through stirring or phase imprinting; thus the observations presented represent a new regime for the study of quantized vortex nucleation in BECs.

For Quench A, the experimental data set consisted of 90 BEC images, with between 21 and 25 images (23% to 28%) containing at least one visible vortex core. The quoted error ranges are defined by the uncertainty in determining whether or not an image shows a vortex core. For example, a vortex core tilted or bent with respect to the imaging axis will decrease the visibility of the core; localized decreases in the density profile of a given image thus may or may not clearly indicate the presence of a core, these uncertain cases are used to define the error. An image where a core is clearly present can be seen in Figure 6.2 (a) versus an image where there is density dip but it is unclear whether it is a vortex core can be seen in Figure 6.2 (b). For Quench B 98 images were obtained, with between 15 and 20 images (15% to 20%) showing at least one vortex core. While the two quenches utilize quite different rf evaporation trajectories, they exhibit similar cooling and BEC growth rates. For this reason it can be expected that statistical similarities should exist between the two data sets. Further breakdown of the experimental observations can be seen in Table 6.1 at the end of this chapter.

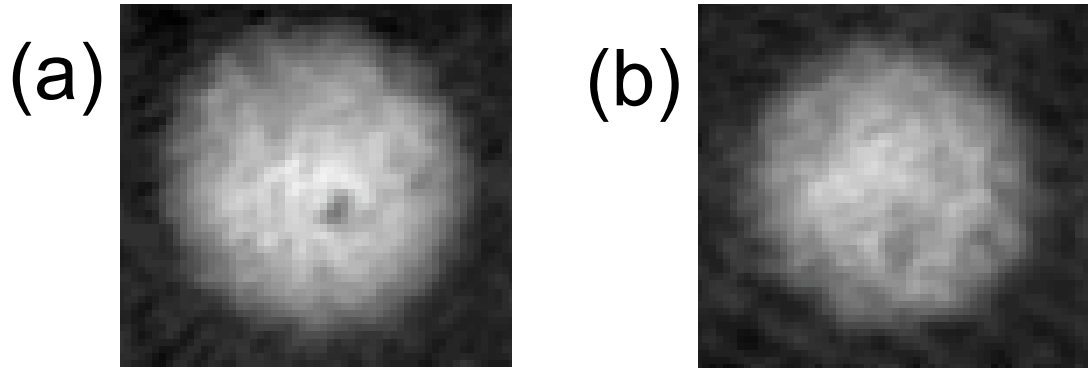

Figure 6.2: Example experimental images. (a) Example image of a clear vortex. (b) example image showing a localized decrease in density that may or may not be a vortex. The uncertainty in determining whether a core is present in the cloud was taken into account in our counting statistics.

6.3.3 Numerical Procedure

The following procedure was followed for the harmonic trap numerical simulations:

1. Start with an equilibrium state such that the temperature of the system T is greater than the critical temperature T_c.
2. Change the temperature T, and chemical potential μ to initiate the condensate formation process.
3. Watch the BEC form, looking for the presence of vortices.
4. Repeat items 1–4 many times.
5. Determine vortex formation statistics.
6. Compare the numerical statistics with the experimental statistics.

The goal for the numerical simulations is to have each simulation run mimic that of the experiment.

6.3.4 Numerical Results

Davis and Bradley simulated condensate formation using parameters that matched our experimental parameters using the Stochastic Gross-Pitaevskii equation (SGPE) formalism [89, 90]. This approach represents the condensate and highly-occupied excitations as a classical field that evolves according to a generalized Gross-Pitaevskii equation, as described in Section 6.2.2. Collisions of these partially condensed matter waves with high-energy atoms in the thermal cloud at chemical potential μ and temperature T also introduce dissipation and thermal noise into the SGPE. The initial states used in their simulations are independent field configurations generated by ergodic evolution of the SGPE at equilibrium with the thermal cloud with $\mu_i = \hbar\omega_r$ and $T_i = 45(35)$ nK for Quench A (B), representing the thermalized Bose gas above the transition temperature.

Evaporative cooling experiments contain many physical subtleties that are difficult to model in their entirety; in light of this Davis and Bradley represent an idealized cooling procedure by a sudden jump in chemical potential and temperature of the thermal cloud to $\mu_f = 25.0$ (22.0) $\hbar\omega_r$ and $T_f = 34$ (25) nK for Quench A (B) for 300 (298) initial field configurations. By averaging over the different realizations any quantum mechanical observable can be calculated as a function of time, and in particular the single-particle density matrix can be calculated and diagonalized to find the condensate number [91, 99]. However, each trajectory can be interpreted as corresponding to an experimental run as long as it remains within the Wigner formalism underpinning the SGPE. Therefore, a vortex dynamics study can be obtained for each condensate as it grows and comparisons of the numerical vortex observation statistics and our experimental statistics can be made. Because vortex formation is expected to depend upon the BEC growth rate, the coupling rate is adjusted which describes Bose-enhanced collisions between the classical field and thermal cloud. This provides the means of obtaining a close match to the experimental BEC growth curves. The dashed (solid) curves in Fig. 6.1 are the numerical results for Quench A (B), and the good agreement with experiment allows a meaningful comparison of vortex observation statistics.

For each simulated data set, our collaborators count the number n_j and extract the percentage P_j of images that show $j = 0$, 1, or 2 vortex cores within a radius of vortex core displacements $d_c < 0.8$, where $d_c \equiv |\mathbf{r}|/R_{TF}$, $\mathbf{r}$ is the position vector of the vortex core relative to the BEC center, and R_{TF} is the Thomas-Fermi radius of the BEC.

To determine the presence of a vortex Davis and Bradley consider an instantaneous slice of the classical field in the $z = 0$ plane of the trap, and detect all phase-loops of $\pm 2\pi$ with $d_c < 0.8$ where the Thomas-Fermi radius is based on the (time-dependent) condensate number. It was found that the majority of vortices (although not all) were aligned with the z axis of the trap. The vortex observation probabilities obtained from the simulations are plotted against time in Fig. 6.4 for Quenches A and B, where the experimentally measured probabilities are plotted as

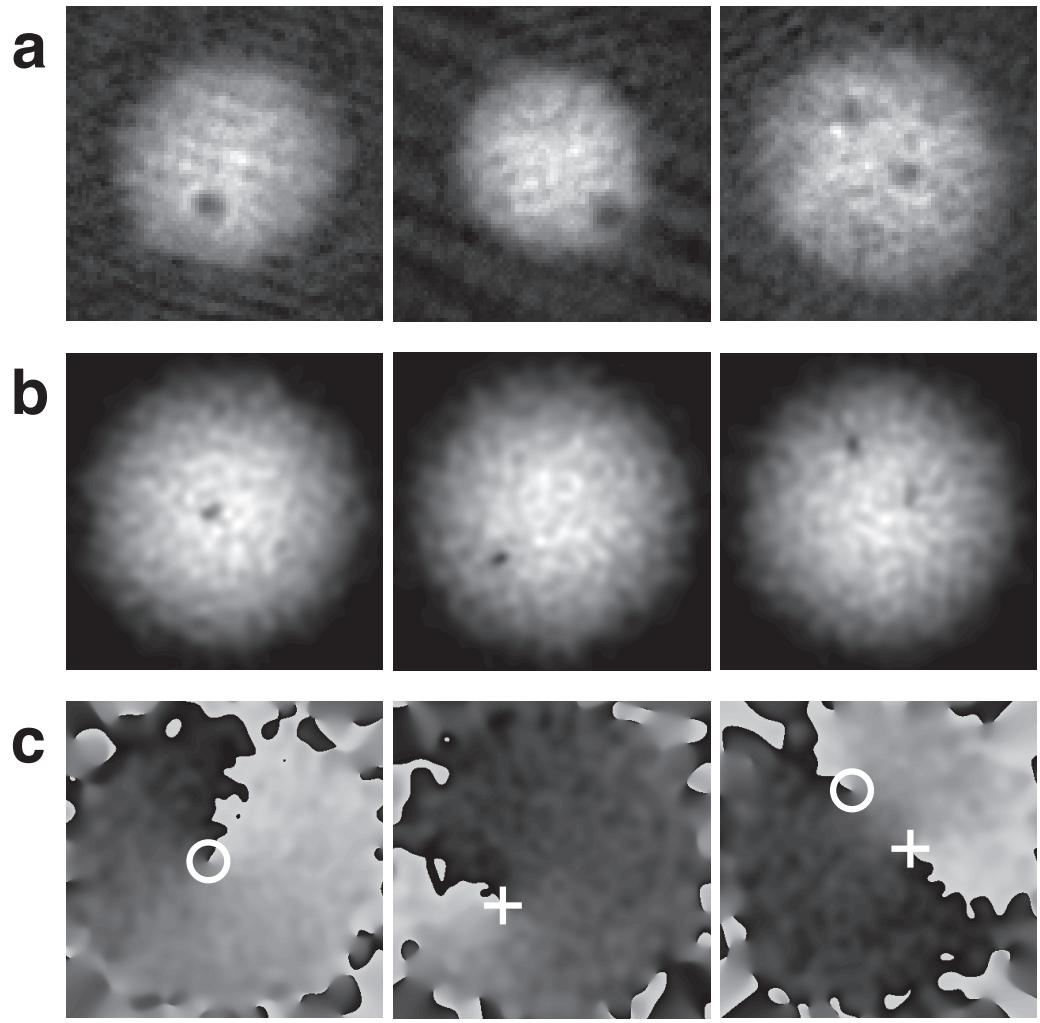

Figure 6.3: Vortices in the harmonic and toroidal traps. **(a)**, Example 200-μm-square expansion images of BECs created in a harmonic trap, showing no vortices (left), a single vortex (centre), and two vortices (right). **(b), (c)**, Sample simulation results from Quench B, showing integrated column densities along z (in **(b)**) and associated phase profiles in the $z = 0$ plane (in **(c)**), with vortices indicated by crosses and circles at $\pm 2\pi$ phase windings.

horizontal grey bars with widths corresponding to the measurement error ranges reported earlier in Section 6.3.2.

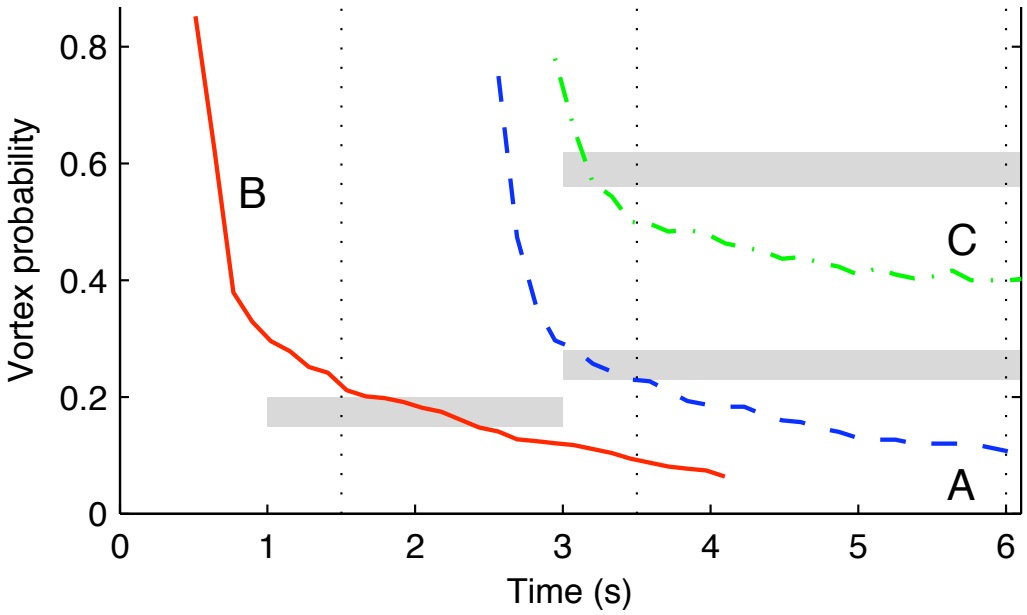

Figure 6.4: Vortex statistics. The plots show the decay rate of vortex observation for the simulation as a function of time for both Quench A (dashed line) and Quench B (solid line). The vertical dashed lines indicate the observation times at which the vortex statistics were gathered for the theoretical results. The grey areas indicate the experimental measurement range for each data set.

According to the SGPE simulations the number of vortices decreased as a function of time, which is consistent with the model being used. Specifically, the thermal bath had no angular momentum, so the thermodynamic final state should be a condensate without any vortices due the coupling imparted to the thermal bath and the condensate. In this respect the simulations diverged from the experimental observations, where no significant variation of the vortex observation probability occurred with time. For example, with the conditions of Quench B, the experimental vortex observation statistics are approximately constant between observation times of 1.5 s and 6 s after the initiation of the quench, indicating negligible damping of vortices

on this timescale. This low damping rate is consistent with the comparatively small thermal fractions observed in the images, this discrepancy indicates that a more sophisticated theory may be needed to fully account for the dissipation and cooling processes of the experiment. The simulated results are quoted at times $t = 3.5$ s for Quench A, and $t = 1.5$ s for Quench B, based upon the experimental observations that vortex damping is negligible, and because the BEC is nearly fully formed at these times in the simulation. A summary of the theoretical results is shown in Table 6.1.

6.3.5 Dynamics of condensate growth*

With the exception of condensate growth in the hydrodynamic regime [57], prior condensate formation experiments [58–61] have been well described by assuming the condensate always grows in the absolute ground state of the system [51–56]. Here Davis and Bradley show that detailed examination of BEC growth using the SGPE theory reveals the role of excited states in condensate growth and the microscopic dynamics of vortex formation. A description of one run of the simulation in which a single vortex persists to the final time step for a Quench A simulation in the purely harmonic trap is given here to provide intuition into the condensation growth process. After the system temperature is initially lowered but before a bulk BEC has clearly formed, the density profile of the atomic field clearly fluctuates temporally and spatially. A snapshot illustrating this state is given in Fig. 6.5 (a), with isodensity surfaces shown in a three-dimensional rendering. As time progresses, a bulk BEC begins to grow, and a tangle of vortices is trapped within the BEC as shown in Fig. 6.5 (b), in qualitative agreement with both the predictions of Svistunov and the Kibble-Zurek scenario. At later stages, a nearly uniform condensate exists with clear vortex cores, as shown in Fig. 6.5 (c). This state eventually damps to a single core, seen in Fig. 6.5 (d).

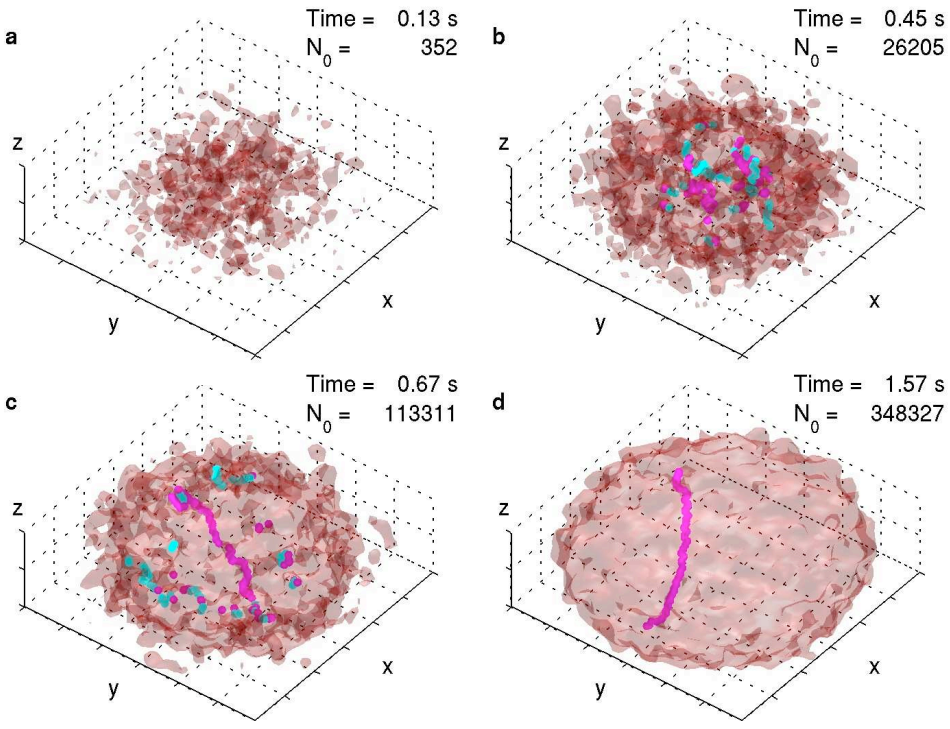

Figure 6.5: BEC growth dynamics. (a–d) Four snapshots during the simulated growth of a BEC showing isodensity surfaces as described in the text. Vortex cores of opposite charges about the z axis are indicated as magenta and cyan lines. The corresponding times are **a**, 0.13 s; **b**, 0.45 s; **c**, 0.57 s; **d**, 1.57 s, where $t = 0$ is the time when the quench is initiated in the simulation.

Quench	**runs**	**0 cores**		**1 core**		**2 cores**	
		$\mathbf{n}_0$	$\mathbf{P}_0$	$\mathbf{n}_1$	$\mathbf{P}_1$	$\mathbf{n}_2$	$\mathbf{P}_2$
A, expt.	90	65 - 69	72% - 77%	18 - 23	20% - 26%	2 - 3	2% - 3%
A, sim.	300	229	76.3%	68	22.7%	3	1.0%
B, expt.	98	78 - 83	80% - 85%	13 - 18	13% - 18%	2	2%
B, sim.	298	234	78.5%	61	20.5%	1	1.0%

Table 6.1: Table of Results for Harmonic Trap

CHAPTER 7

Spontaneous Vortices in a Toroidal Trap

7.1 Introduction

Adding a potential barrier to the center of a harmonic trap forms a multiply-connected, toroidal potential in which a BEC may display both stable superfluid flow circulating about the barrier (persistent flow) [100] as well as free vortices not pinned to the barrier. Vortex pinning in this geometry is due to energy minimization of the system; the energy cost of a vortex at the zero point in the density of the fluid created by the potential is minimal compared to elsewhere. The pinning of superfluid flow may influence both vortex dynamics during BEC growth and observations of vortices after the BEC is formed: if a vortex becomes pinned to the central barrier, the chances for complete self-annihilation between pairs of spontaneously formed vortices of opposite charge are reduced, and the probability of finding vorticity in the fully formed BEC is increased. The following will provide an overview of the experimental and theoretical investigation of spontaneous vortices in a toroidal trap geometry.

7.2 Methods for the Toroidal Trap

For this experiment the initial evaporative cooling stages remained the same as described in Section 4.2.2 in Chapter 4 except for the addition of a potential barrier to the center of the magnetic trap using a focussed blue-detuned diode laser (Mitsubishi model 101J27-01 laser diode) beam. The beam was ramped on during the relaxation of B_z' to the 54 G/cm value. The 660 nm wavelength beam had a focused Gaussian spot size of 6-μm at the plane of the BEC, with $\sim$18 μW of power. A schematic of the optical setup used to create the toroidal trap as well as an image of the intensity profile of the beam at the BEC plane can be seen in Figure 7.1.

The beam intensity corresponds to a potential barrier of approximately $k_B \cdot 20$ nK, where k_B is Boltzmann's constant. This can be compared with a $\sim k_B \cdot 10$ nK chemical potential of a fully formed BEC in the purely harmonic trap. The beam only slightly perturbed the thermal cloud but provided enough additional potential energy along the vertical axis to exclude BEC atoms from the z axis of the trap. An in trap, phase contrast image of the BEC in the toroidal trap can be seen in Figure 7.2.

The application of the aforementioned blue-detuned laser beam allowed us to experimentally study BEC growth in a toroidal potential with a 6-s final evaporative cooling ramp identical to the harmonic trap Quench A (see Section 6.2); this data set is identified as Quench C. After creating the BEC in this potential, we remove the optical potential by ramping down the beam's power over 100 ms and immediately allow the BEC to expand from the trapping potential. The expansion and imaging procedure are exactly the same as that for the harmonic trap.

7.3 Toroidal Trap Results

7.3.1 Experiment

In a 52-image data set, we found between 29 and 32 images (56% to 62%) containing at least one visible vortex core, more than a factor of two increase over the Quench A statistics (20% to 26% out of 90 runs).There also was a significant increase in the number of images with at least 2 cores present; 10% to 23% of the images compared to 2% to 3% for Quench A. A breakdown of the experimental statistics for the toroidal trap can be seen in Table 7.1. Also, example expanded BEC images are shown as the center and rightmost images in Figure 7.4 (d).

7.3.2 Theory*

Experimental data on condensate formation was not measured for this data set. Hence, for the simulations all thermodynamic parameters are identical to Quench A but with a repulsive Gaussian barrier inserted with a height of 33 $\hbar\omega_r$. A plot of sim-

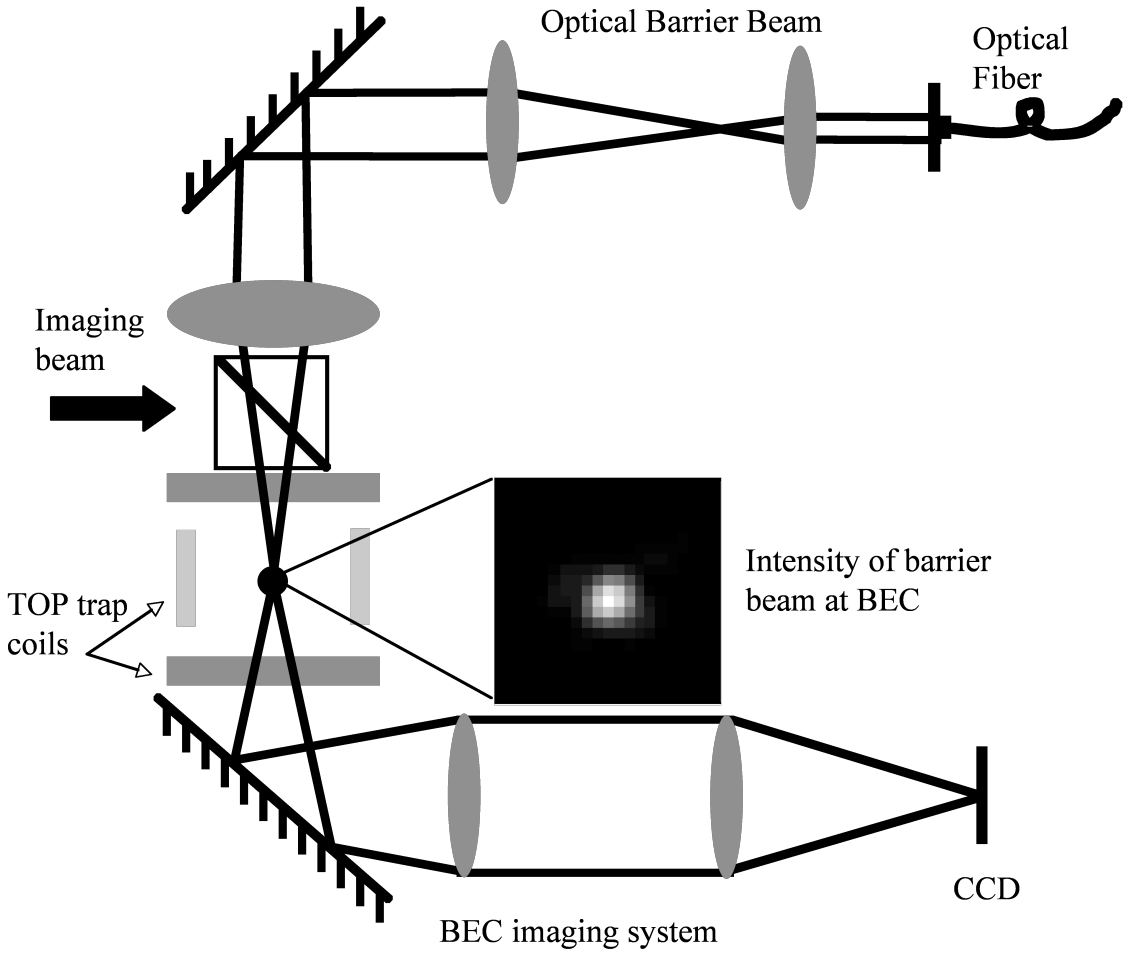

Figure 7.1: Schematic of the experimental setup for the toroidal trap. The optical barrier beam is coupled from an optical fiber and expanded through a telescope. The now expanded collimated beam gets focused onto the BEC plane by a 100 mm achromat lens mounted in a zoom lens mount. The zoom lens mount provides the means of focusing the beam directly on the condensate. An image of the intensity profile of the beam at the BEC plane is shown. (Image modified version of Figure 5.3 in reference [22].)

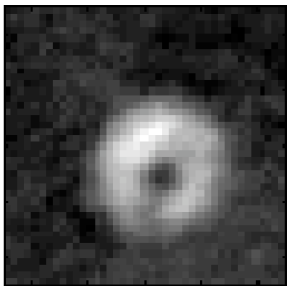

Figure 7.2: In trap, 70 μm square phase contrast image of a condensate in the toroidal trap. The maximum strength of the optical plug beam is 18 μW, which is strong enough to displace fluid from the center of the barrier. This is not a vortex.

ulated condensate growth versus time is shown as the dot-dashed curve in Figure 7.3 (a). These simulations provided a reasonable comparison to experimental results. Both in the experiment and the simulations the condensate formation occurs later in time and the final condensate number is reduced compared to Quench A. Examples of the numerically obtained column density and phase are shown in Figure 7.4 (e–f) for 3 of 300 trajectories. The vortex observation statistics are plotted as a dot-dashed line in Fig. 7.3 (b); the simulations show the probability of finding a vortex is approximately twice that of the harmonic case but somewhat lower than the experimental observations. For the toroidal case, the vortex observation curve does not exhibit decay below 40% in contrast to the harmonic case — this corresponds to vortices that are pinned by the central barrier. Additional statistics for the toroidal trap simulated data are provided in Table 7.1.

Once the vortex is pinned, it is isolated from further dynamics and annihilation with other vortices of opposite charge, as postulated above, increasing vortex observation probabilities. By examining the distribution of vortex core positions for both the experimental and simulated data we see that the toroidal trap induces a clustering of vortex cores, whereas in the harmonic trap the core positions are more evenly spread throughout the BECs. A visual comparison of these cases is given in Figure. 7.5 (a–d). Figure 7.5 (e–f) show a histogram of vortex core displacements away from the mean core position for the two different trap geometries for experiment and

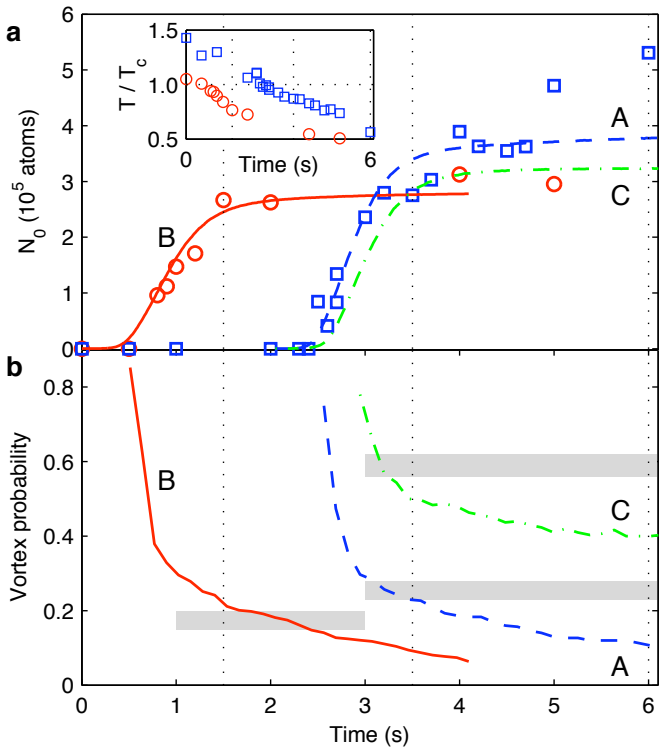

Figure 7.3: The green dot-dashed line is the theoretical result for the condensate number versus time in the toroidal trap (Quench C). The vertical dotted lines indicate the observation times for which statistics are generated. (b), The probability of finding at least one vortex passing through the $z = 0$ plane plotted for all three simulated quenches. The grey areas indicate the experimental measurement range for each data set.

theory. Due to the observation that the cores in the experimental toroidal trap data are likely to be found within a small region within the BEC, we interpret our results as indicating that the observed cores are likely to have been pinned to the central barrier prior to expansion. This suggests possibilities for future controlled studies of spontaneous vortex formation, perhaps with multiple sites at which vortices may be pinned, in order to better understand the density and number of vortices created at early times in BEC growth.

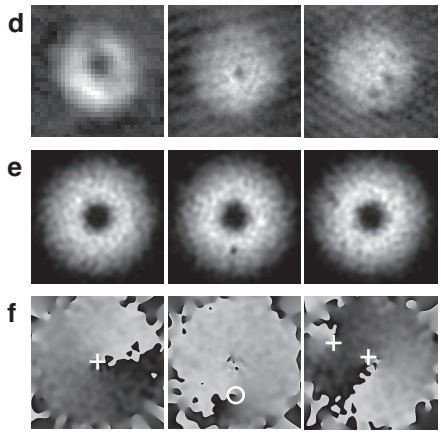

Figure 7.4: Vortices in the toroidal trap. **(d)** Left image: 70-μm-square phase-contrast experimental image of a BEC in the toroidal trap (vortices are not visible). Remaining Images: Vortices are visible in 200-μm-square expansion images of BECs created in the toroidal trap. **(e, f)**, Simulations of BEC growth in the toroidal trap show vortices (as in Figure 6.3 **b**–**c**) and persistent currents.

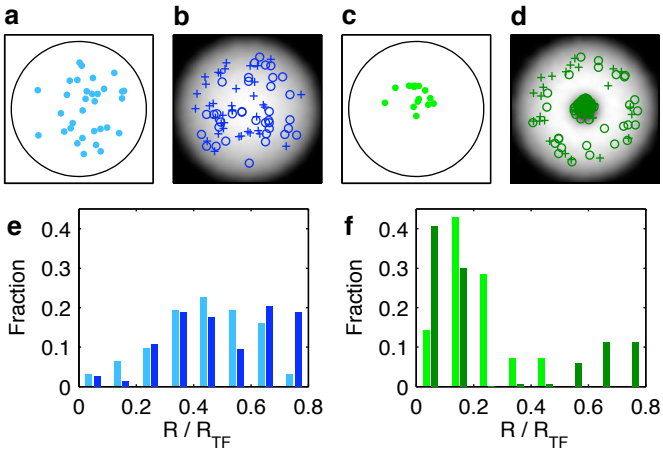

Figure 7.5: Vortex core pinning. **(a, c)**, Representation of the experimentally measured positions of all vortex cores relative to the Thomas-Fermi radius (outer circles) for **(a)**, the harmonic trap and **(c)**, the toroidal trap. **(b, d)**, Corresponding theoretical results, crosses and circles indicate oppositely charged vortices. **(e, f)**, Comparison of the statistics of the vortex locations, binned in steps of $0.1R_{TF}$, for the experimental data (left bars) and theoretical simulations (right bars). Harmonic trap results are shown in **(e)**, toroidal trap results are shown in **(f)**. For the experimental data, only images clearly showing a single core are considered.

Quench	**runs**	**0 cores**		**1 core**		**2 cores**	
		$\mathbf{n}_0$	$\mathbf{P}_0$	$\mathbf{n}_1$	$\mathbf{P}_1$	$\mathbf{n}_2$	$\mathbf{P}_2$
Toroidal, expt.	52	20 - 23	38% - 44%	15 - 25	29% - 48%	5 - 12	10% - 23%
Toroidal, sim.	300	147	49.0%	137	45.7%	16	5.3%

Table 7.1: Table of Results for Toroidal Trap

CHAPTER 8

CONCLUSIONS

8.1 Introduction

The significance of the work described in this dissertation may be far reaching for universal studies of phase transitions. The work presented here has opened up the possibility for new avenues of research in the study of spontaneous symmetry breaking and topological defect formation. The utility of the SGPE method to simulate the dynamics of the BEC phase transition has been established through the excellent agreement between it and our experimental results. Although the results of our experimental and theoretical studies are exciting, there are still many open questions left to be answered.

This concluding chapter will give an overview of the areas of research that need to be addressed in order to begin making quantitative comparisons to the ideas of spontaneous symmetry breaking and topological defect formation. It will also touch on some the major factors we believe allowed us to see spontaneous vortices, considering such observations have not been previously reported. The discussion will close with a description of the impact our work may have on the field of topological defect formation.

8.2 Why Did We See Spontaneous Vortices?

In our experiments on condensate formation dynamics, we have not performed any uncommon experimental techniques in order to observe these vortices; the Bose gas of ^{87}Rb atoms was evaporatively cooled in a manner similar to those of most other dilute-gas BEC experiments, with the cooling occurring over a relatively long time scale for Quench A and C rather than as a fast quench as one might expect would be

necessary. It is then natural to wonder why our experiments have yielded observations of spontaneous vortex formation during the BEC phase transition, particularly because such observations have not previously been reported. We believe that the major factors leading to our observations are:

1. We evaporatively cool our gas to near degeneracy in a tight trap, and then relax the trap to the final trapping frequencies before our final cooling ramp. This relaxation reduces the atomic collision rate at the point at which condensation occurs, and potentially decreases the ratio of the correlation length to the size of the ground state of the trap (the harmonic oscillator length) and thus increases the number of vortices expected to form. In the KZ mechanism, the correlation length ξ depends on the quench time τ_Q, so specific details of the ratio of correlation length to the harmonic oscillator length will depend upon specific cooling trajectories, as well as trap frequencies. Regardless of the initial number of vortices formed, we expect that vortices may survive for longer times in weaker trap, where the weaker atomic interactions generally decrease the rates of dynamical processes.

2. Our experiment is performed in a pancake shaped trap with an approximately 2:1 aspect ratio, in which it is favourable for the vortices to align along the vertical axis [73]. The majority of condensate formation experiments reported to date in the literature have been performed in cigar-shaped traps [57–61].

3. We introduce a linear magnetic field during expansion that supports the condensate against gravity and allows for long expansion times before imaging. During ballistic expansion of the condensate, the vortex cores expand relative to the condensate size and grow to such a size that our imaging system can optically resolve the cores.

4. We have the ability to acquire images of trapped atoms along the both the vertical axis (the direction of strongest confinement) as well as the standard horizontal imaging axis, allowing us to detect vortices that are well-aligned

with the vertical axis.

It seems entirely possible that spontaneous vortices have been present in other experiments, but simply could not be resolved, damped quickly, or were not sought. We are aware of one other experiment that has recorded the spontaneous formation of vortices during condensation (David Hall, private communication).

8.3 Future Directions

In order to examine the relationship of our observed vortex statistics with the predictions of the KZ mechanism, one would ideally perform a controlled ramp of either μ or T through the critical point. In our experiments we are unable to substantially change this rate merely by altering the rf evaporation trajectory while holding other conditions constant. Nevertheless, with the fastest BEC growth that we have been able to experimentally achieve in our weak harmonic trap (about two to three times faster than the growth rate using Quench A), the fraction of images showing at least one vortex core substantially increased. In a set of 60 images obtained under these faster conditions, 28 to 32 of the images (47% to 53%) had a vortex core visible, a factor of $\sim$2 increase over the data of Quenches A and B. In simulations, our collaborators able to increase the speed of condensate growth by increasing the coupling to the thermal cloud, γ. It was found that while this results in more vortices up to a point, eventually the damping rate is sufficient to keep the condensate near its instantaneous ground state at all times throughout its growth.

One of the first experiments to be performed, with the intent of cooling the BEC rapidly, will be to form the condensate with a thermal cloud loaded into a dimple style trap [101, 102]. This trap utilizes the overlap of a tightly focused far red-detuned laser beam with the harmonic TOP trap. The beam will be focused using a cylindrical lens, thus creating a sheet of light and maintaining our pancake shape geometry. The beam is ramped on adiabatically such that it will trap a small portion of the overall thermal atomic sample but will keep this sample in contact with the thermal bath. By compressing the atomic cloud in one direction adiabatically with

the dimple, an increase in phase space density will occur. With the right conditions the mixture of the increase in phase space density and collisions with the thermal cloud will cause the small sample to condense to a BEC. This condensation process will be very rapid and should allow for the increase in the quench rate needed to see noticeable changes in the number of vortices created during condensation. Once the condensate is formed one of the major issues with this configuration is the need to rapidly dispense with the thermal cloud such that expansion and imaging of the condensate is possible. The major goal of this work is to provide the ability to make more quantitative measurements between our experimental observations and the Kibble-Zurek scenario. Specifically, it is important to investigate whether a power-law dependence exists between the quench rate $1/\tau_q$ and the density of vortices formed.

An experiment that would be on the same lines as the above described experiment would be to to create multiple pinning sites in the BEC. This would allow for further vortices to be taken out of the vortex dynamics present in the system, thus increasing the ability to quantify a density of vortices.

On another quite different path, the phenomenon of superradiance [103] could be employed to probe the formation and merging of the proto-condensates. This would open a myriad of possibilities for understanding the formation and merging processes present during the BEC phase transition.

8.4 The Major Significance of this Dissertation

Perhaps the most significant result of our work is the remarkably good overall agreement between our experimental and numerical results, reinforcing our interpretation and understanding of spontaneous vortex formation in BECs and superfluids. These results may thus impact and motivate a new class of experimental and theoretical studies of finite-temperature BECs and ultra-cold gases near the BEC phase transition. Our approach may be immediately adapted for instance to studies of condensation and the development of coherence in various trap geometries and with various

atomic species and interaction strengths. By assembling a range of such investigations, the fundamental nature and implications of universality in phase transitions may be experimentally and numerically explored at the microscopic level, with potential benefit across many areas of physics.

APPENDIX A

THREE WELL PAPER

PRL **98,** 110402 (2007) PHYSICAL REVIEW LETTERS week ending 16 MARCH 2007

Vortex Formation by Merging of Multiple Trapped Bose-Einstein Condensates

David R. Scherer, Chad N. Weiler, Tyler W. Neely, and Brian P. Anderson
College of Optical Sciences, University of Arizona, Tucson, Arizona 85721, USA
(Received 5 October 2006; published 12 March 2007)

We report observations of vortex formation by merging and interfering multiple ^{87}Rb Bose-Einstein condensates (BECs) in a confining potential. In this experiment, a single harmonic potential well is partitioned into three sections by a barrier, enabling the simultaneous formation of three independent, uncorrelated BECs. The BECs may either automatically merge together during their growth, or for high-energy barriers, the BECs can be merged together by barrier removal after their formation. Either process may instigate vortex formation in the resulting BEC, depending on the initially indeterminate relative phases of the condensates and the merging rate.

DOI: 10.1103/PhysRevLett.98.110402 PACS numbers: 03.75.Lm, 03.75.Kk, 67.40.Vs

In superfluids, long-range quantum phase coherence regulates the formation and dynamics of quantized vortices [1,2]. In a dilute-gas Bose-Einstein condensate (BEC), for example, vortices can be created using direct manipulation of the quantum phase profile of the BEC [3,4]. Vortices in BECs have also been created using methods more analogous to those of classical fluids [5], namely, through rotating traps [6–9], turbulence [10], and dynamical instabilities [11,12]. Yet in contrast with classical fluids, vortex generation via the mixing of initially isolated superfluids remains experimentally unexplored. Because of the relative ease of microscopic manipulation and detection techniques, BECs are well suited to answer open questions related to superfluid mixing and vortex generation.

In this Letter, we describe our experiments demonstrating that merging together three condensates in a trap can lead to the formation of quantized vortices in the merged BEC. We ascribe the vortex generation mechanism to matter-wave interference between the initially isolated BECs, and show that vortices may be induced for both slow and fast merging rates. While it is now well known that matter-wave interference may occur between BECs [13], and that condensates can be gradually merged together into one larger BEC [14], our experiment demonstrates a physical link between condensate merging, interference, and vortex generation, providing a new paradigm for vortex formation in superfluids. We emphasize that no stirring or BEC phase engineering steps are involved in our work; the vortex formation process is stochastic and uncontrollable, and partially depends on relative quantum phases that are indeterminate prior to condensate merging. This vortex formation mechanism may be particularly relevant for developing further understanding of the roles of potential-well defects, roughness, and disorder on establishing a superfluid state. Furthermore, this work may be viewed as a model for studies of spontaneous symmetry breaking and topological defect formation during phase transitions [15,16].

To illustrate the basic concept underlying our experiment, we first describe our atom trap, which is formed by the addition of a time-averaged orbiting potential (TOP) trap [17] and a central repulsive barrier of axially (vertically) propagating blue-detuned laser light shaped to segment the harmonic oscillator potential well into three local potential minima. Figure 1(a) shows an example of potential-energy contours of our triple-well potential. We will assume throughout the ensuing discussions that the energy of the central barrier is low enough that it has negligible effect on the thermal atom cloud, as in our experiments, but high enough for independent condensates to begin forming in the three local potential minima from the single thermal cloud. There are two important regimes in this range of barrier energies: (1) if the central barrier is weak, condensates with repulsive interatomic interactions will grow and merge together during evaporative cooling; and (2) if the barrier is strong, the condensates will remain independent, but may be merged together by lowering the barrier while keeping the atoms trapped [18]. We have examined both scenarios.

Depending on the relative phases of the three condensates and the rate at which they merge together (via either process), the final merged BEC may have acquired nonzero net angular momentum about the trap axis. To demonstrate

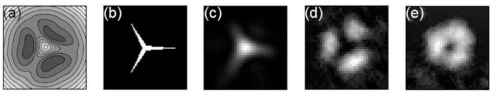

FIG. 1. (a) Potential-energy contours of a horizontal slice through the center of our triple-well trap, representing the addition of the potential-energy profiles of our TOP trap and barrier beam. (b) The binary transmission mask used to create the optical barrier. (c) An image of the optical barrier. (d),(e) Phase-contrast images of trapped condensates as viewed along the trap axis. Each shows an area of 85 μm per side, as do (a) and (c). In (d), three condensates are created in the presence of a strong barrier beam with 170 μW. (e) With 45 μW in the beam, the initial three condensates merge together during evaporative cooling. A hole in the BEC is formed by the barrier beam displacing atoms from the trap center.

this, we first envision two condensates in two potential minima merged slowly enough that although interference occurs between the condensate pair, interference *fringes* do not. As merging begins, above-barrier fluid flow between the pair is established, with the initial flow direction depending on the sine of the phase difference between the overlapping states (as also occurs in the Josephson Effect [1,19] for the case of tunneling). Recalling that the relative phase between two independent condensates is indeterminate until it is measured via interference, the relative phase and hence fluid flow direction will vary randomly upon repeated realizations of the experiment [20].

When the three condensates of our experiment gradually merge, a net fluid flow over the barrier arms may occur that is either clockwise, counter-clockwise, or neither, relative to the trap center. For ease of this discussion, and keeping in mind that only relative phases carry physical meaning, we imagine that the condensates formed in the three local minima can be labeled with phases ϕ_j, where the indices $j = 1$, 2, and 3 identify the condensates in a clockwise order, respectively. Upon merging, if the relative phases happen to be (say) $\phi_2 - \phi_1 = 0.7\pi$ and $\phi_3 - \phi_2 = 0.8\pi$, thus necessarily $\phi_1 - \phi_3 = 0.5\pi$, then clockwise fluid flow will be established for the fluid. More generally, if the three merging condensates happen to show relative phases $\phi_2 - \phi_1$, $\phi_3 - \phi_2$, and $\phi_1 - \phi_3$ that are each simultaneously between 0 and π, or each between π and 2π, the resulting BEC will have acquired nonzero net angular momentum after the merger, which will be manifest as a vortex within the BEC [21]. By examining the full range of phase difference possibilities, the total probability P_v for a net fluid flow to be established in either azimuthal direction is found to be $P_v = 0.25$, given random phase differences for each experimental run. P_v is thus the probability for a vortex to form as the three condensates merge together. This relationship between vortex trapping and relative phases is an application of the so-called geodesic rule [22]. Related work includes a theoretical investigation of three Josephson-coupled BECs [23], and spontaneous defect trapping in liquid crystals [24].

For yet faster merging rates and correspondingly steeper phase gradients, interference *fringes* may indeed develop as the condensates merge. To estimate the longest time scale τ_f over which two merging condensates can support a single dark interference fringe, we envision two condensates that are initially atomic point sources separated by a distance d, and that each expands to a radius of d in time τ_f such that the condensates overlap in the intervening region. The condensate expansion speed $v \sim d/\tau_f$ corresponds to a phase gradient at the side of each condensate of $\nabla\phi = \frac{vm}{\hbar} \sim \frac{dm}{\tau_f \hbar}$, with m the atomic mass. To create a single full interference fringe in the overlap region, $\nabla\phi \sim \pi/d$. With $d \sim 35$ μm, appropriate for our experiment, $\tau_f \sim 550$ ms; shorter merging times would produce more interference fringes, while longer times correspond to slow merging and no fringes. Each dark fringe will be subject to the same dynamical instabilities as dark solitons and decay to vortices, antivortices, and possibly vortex rings over times on the order of 50 ms [11,12,25]. Similar decay has been seen in recent numerical simulations [26]. For condensates merged together over times of τ_f or shorter, we may thus expect to find multiple vortex cores in a BEC, or to find a value of P_v exceeding 0.25.

Our basic single BEC creation technique involves the following steps. We first cool a thermal gas of $|F = 1, m_F = -1\rangle$ ^{87}Rb atoms to just above the BEC critical temperature in an axially symmetric TOP trap with radial and axial trapping frequencies of 40 and 110 Hz, respectively. We then ramp the TOP trap magnetic fields such that the final trap oscillation frequencies are 7.4 Hz (radially) and 14.1 Hz (axially). A final 10-sec stage of radio-frequency forced evaporative cooling produces a condensate of $\sim 4 \times 10^5$ atoms, with a condensate fraction near 65% and a thermal cloud temperature of $\sim$22 nK. The BEC chemical potential is $k_B \times 8$ nK, where k_B is Boltzmann's constant.

To study vortex formation induced by merging together three condensates formed independently in a triple-well potential, we modify the above procedure by ramping on the three-armed optical barrier immediately *before* the final BEC-producing 10-sec stage of evaporative cooling. The barrier itself is formed by illuminating a binary mask, illustrated in Fig. 1(b), with a focused blue-detuned Gaussian laser beam of wavelength 660 nm. After passing through the mask and a lens to image the mask onto the atom trap, the beam enters our vacuum chamber along the trap axis. Because of diffraction, the beam has an intensity profile as shown in Fig. 1(c), with a maximum intensity and thus barrier energy aligned with the center of the TOP trap. The barrier's potential energy decreases to zero over $\sim$35 μm radially along the three barrier arms separated by azimuthal angles of 120°. With 170 μW in the beam, corresponding to a maximum barrier energy of $k_B \times$ 26 nK, three condensates are created without merging together during their growth [18]; a set of three such BECs is shown in Fig. 1(d). With, instead, 45 μW in the beam, corresponding to a maximum barrier energy of $k_B \times$ 7 nK, three independent condensates also *initially* form, but as the condensates grow in atom number, they gain enough interaction energy to flow over the barrier arms. The three condensates then naturally merge together into one BEC during evaporative cooling, as shown in Fig. 1(e). We stress that in neither case is a *single* BEC formed that is then split into three sections.

In our first study, three spatially isolated condensates were created in the presence of a strong barrier of maximum potential energy $k_B \times 26$ nK, and were then merged together by ramping down the strength of the barrier to zero over a variable time τ. Since vortex cores are too small to be directly observed in the trapped BEC, we suddenly removed the trapping potential after merging and viewed the atom cloud using absorption imaging along the trap

axis after 56 ms of ballistic expansion. This process was repeated between 5 and 11 times for each of 6 different barrier ramp-down times τ between 50 ms and 5 sec.

In a significant fraction of our merged BECs, one or more vortex cores were visible, indicating that condensate merging can indeed induce vortex formation. The spatial density distributions varied from shot to shot, as would be expected with indeterminate phase differences between the initial condensates, while many images were absent of vortices. Example images of expanded BECs in Figs. 2(a)–2(d) show the presence of vortex cores after various barrier ramp-down times. An analysis of vortex observation statistics is given in Fig. 2(e) for the different values of τ examined. Here we define a vortex observation fraction F_v as the fraction of images, for each value of τ, that show at least one vortex core. The error bars reflect our uncertainty in determining whether or not an image shows at least one vortex. For example, corelike features at the edge of the BEC, or features obscured by imaging noise, may lead to uncertainty in our counting statistics and determination of F_v. As the plot shows, F_v reaches a maximum of $\sim$0.6 for the smaller τ values, and drops to $\sim$0.25 for long ramp-down times. We expect that with a large number of images, F_v should approximate P_v for each τ. Thus our results are consistent with our conceptual expectations, where $P_v > 0.25$ for fast merging times, and $P_v = 0.25$ for slow merging according to the geodesic rule for random initial phase differences. We note that τ is an overestimate of the *actual* merging time, since the condensates are merged before the barrier is completely removed.

For $\tau \leq 1$ sec, multiple cores were often observed, perhaps signifying the creation of both vortices and antivortices. Although we are unable to determine the direction of fluid circulation around the vortex cores, we checked this interpretation by ramping off the barrier in 200 ms, thus forming multiple vortex cores with a high probability. By inserting additional time to hold the final BEC in the unperturbed harmonic trap before our expansion imaging step, the probability of observing multiple cores dropped dramatically: for no extra hold time, we observed an average of 2.1 vortex cores per image, whereas this number dropped to 0.7 for an extra 100-ms hold time, suggestive of either vortex-antivortex combination on the 100-ms time scale, or other dynamical processes by which vortices leave the BEC. However, single vortices were observed even after 5 sec of extra hold time in our trap following the barrier ramp-down, indicating relatively long single-vortex lifetimes in the harmonic trap.

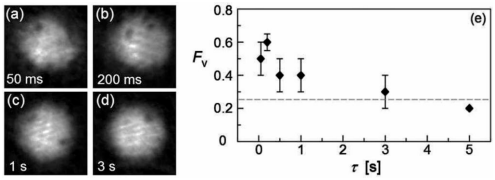

FIG. 2. (a)–(d) 170-μm wide images showing vortices in condensates created as a strong ($k_B \times 26$ nK) barrier was ramped off over the time τ indicated. (e) Vortex observation fraction F_v vs τ. The data for τ values of 50 ms, 200 ms, 500 ms, 1 sec, 3 sec, and 5 sec, consisted of 5, 11, 10, 10, 5, and 5 images, respectively. For clarity, statistical uncertainties due to finite sample sizes are not shown, but they generally exceed our counting uncertainties. The expected lower limit of $F_v \sim P_v = 0.25$ is represented by a dashed line.

In our second main investigation, we differed from the above experiment by using a weaker barrier with a maximum energy of $k_B \times 7$ nK such that three condensates initially formed but naturally merged together into one BEC during evaporative cooling. Here, merging is due solely to the increasing condensate chemical potentials exceeding the potential energy of the barrier arms; the barrier strength remained constant throughout condensate growth and merging when vortices could form. After evaporative cooling produced a single (merged) BEC in the weakly perturbed harmonic trap, we removed the weak barrier over 100 ms and released the atoms from the trap for observation. Under these conditions, our vortex observation fraction was $F_v = 0.56 \pm 0.06$ in a set of 16 images, with examples shown in Figs. 3(a) and 3(b). By adding an extra 500-ms hold time after BEC formation but *before* the barrier and trap removal, F_v decreased to 0.28 ± 0.14, perhaps again due to vortex-antivortex combination. From this we can conclude that with low barrier energies, vortices are formed during the BEC creation process in the perturbed TOP trap, rather than during removal of the weak barrier, consistent with phase-contrast images of trapped BECs that show a continuous final density distribution as in Fig. 1(e).

By using various barrier strengths and barrier ramp-down rates, up to at least four clearly defined vortex cores have been observed upon condensate merging, as the examples of Figs. 3(c)–3(f) show. Density defects other than clear vortex cores have also been observed, as in the upper left of Fig. 3(g), where a ''gash'' may be an indicator of vortex-antivortex combination. Most often, however, no vortices were observed, as in Fig. 3(h). For comparison, a BEC created in a trap without a barrier is shown in Fig. 3(i).

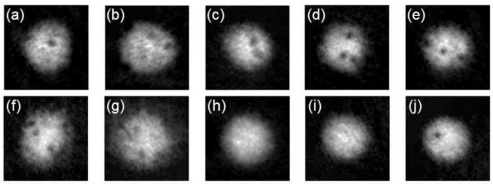

FIG. 3. (a),(b) 170-μm wide images showing vortices naturally occurring in condensates created in a trap with a $k_B \times 7$ nK barrier. (c)–(h) Images obtained using various barrier energies. (i),(j) BECs created without an optical barrier.

As a check on our results and analysis, we used a split-step method to solve the Gross-Pitaevskii equation in simulations of three merging two-dimensional condensates. Details of the simulations will be deferred to a future publication; however, we mention that the simulations display features qualitatively similar to those seen in our experiment, namely: (1) arbitrarily slow merging gives a 25% probability for vortex formation, given random initial phases, and without formation of any interference fringes (solitons); (2) rapid merging leads to interference fringes that decay to multiple vortices and antivortices, which may annihilate each other in the BEC; and (3) as merging times decrease, P_v increases. Our simulations have shown two additional features: (1) slightly asymmetric or off-center barriers, or unequal numbers of atoms in the three wells, can also lead to vortex formation upon merging; and (2) a vortex core may migrate to and be pinned at the center of the barrier where the energy cost of displacing fluid is low; this may help explain why a weak barrier does not appear to readily destroy all BEC angular momentum. We also emphasize that to generate vortices by the mechanisms described here, it is important for three reasons that condensates merge and interfere *while trapped*. First, in a trapped BEC, the nonlinear dynamics due to interatomic interactions play a key role in the structural decay of interference fringes. Second, arbitrarily slow merging times can be studied. Finally, a gas confined in an asymmetric potential well can acquire angular momentum from the trap [21].

We finally note that in a related test, for our basic single BEC creation procedure outlined initially and *without a segmenting barrier ever turned on*, we have observed spontaneous formation of single vortices in about 10% of our images. An example is shown in Fig. 3(j). These observations appear to indicate spontaneous topological defect formation [16] during cooling through the BEC transition, as has been predicted [15]. A full description of this experiment will be given in a future publication.

In summary, we have demonstrated vortex generation by merging isolated and initially uncorrelated condensates into one BEC. Our main results are that (1) subsequent vortex observations are consistent with a conceptual analysis regarding merging rates and indeterminate phase differences between the initial condensates, and (2) BECs created in the presence of weak trapping potential defects or perturbations, such as our weak optical barrier, may naturally acquire vorticity during BEC creation. This second result challenges the notion that a BEC *necessarily* forms with no angular momentum in the lowest energy state of a trapping potential; rather, the shape of a static confining potential may be sufficient to induce vortex formation during BEC growth, a concept important to current and future BEC experiments and perhaps to experiments with other superfluids.

We thank Ewan Wright and Poul Jessen for helpful discussions, and Tom Milster for use of his Maskless Lithography Tool to create our optical barrier mask and phase plates for phase-contrast imaging. This work was funded by grants from the ARO and NSF.

[1] D. R. Tilley and J. Tilley, *Superfluidity and Superconductivity* (Hilger, London, 1986).
[2] R. J. Donnelly, *Quantized Vortices in Helium II* (Cambridge University Press, Cambridge, England, 1991).
[3] M. R. Matthews *et al.*, Phys. Rev. Lett. **83**, 2498 (1999).
[4] A. E. Leanhardt *et al.*, Phys. Rev. Lett. **89**, 190403 (2002).
[5] G. K. Batchelor, *An Introduction to Fluid Mechanics* (Cambridge University Press, Cambridge, England, 1980); *A Gallery of Fluid Motion*, edited by M. Samimy, K. S. Breuer, L. G. Leal, and P. H. Steen (Cambridge University Press, Cambridge, England, 2003).
[6] K. W. Madison *et al.*, Phys. Rev. Lett. **84**, 806 (2000).
[7] E. Hodby *et al.*, Phys. Rev. Lett. **88**, 010405 (2001).
[8] J. R. Abo-Shaeer *et al.*, Science **292**, 476 (2001).
[9] P. C. Haljan *et al.*, Phys. Rev. Lett. **87**, 210403 (2001).
[10] S. Inouye *et al.*, Phys. Rev. Lett. **87**, 080402 (2001).
[11] B. P. Anderson *et al.*, Phys. Rev. Lett. **86**, 2926 (2001).
[12] Z. Dutton *et al.*, Science **293**, 663 (2001).
[13] M. R. Andrews *et al.*, Science **275**, 637 (1997).
[14] A. P. Chikkatur *et al.*, Science **296**, 2193 (2002).
[15] T. W. B. Kibble, J. Phys. A **9**, 1387 (1976); W. H. Zurek, Nature (London) **317**, 505 (1985); P. D. Drummond and J. F. Corney, Phys. Rev. A **60**, R2661 (1999); J. R. Anglin and W. H. Zurek, Phys. Rev. Lett. **83**, 1707 (1999); R. J. Marshall *et al.*, Phys. Rev. A **59**, 2085 (1999).
[16] L. E. Sadler *et al.*, Nature (London) **443**, 312 (2006).
[17] W. Petrich *et al.*, Phys. Rev. Lett. **74**, 3352 (1995).
[18] With a strong barrier, tunneling plays no role due to the large barrier width, and the BECs can be considered independent until merged.
[19] B. D. Josephson, Phys. Lett. **1**, 251 (1962).
[20] P. W. Anderson, in *The Lessons of Quantum Theory*, edited by J. de Boer, E. Dal, and O. Ulfbeck (North-Holland, Amsterdam, 1986), p. 31; J. Javanainen and S. M. Yoo, Phys. Rev. Lett. **76**, 161 (1996).
[21] The barrier in our experiment breaks the trap's cylindrical symmetry, and thus allows exchange of angular momentum between the atoms and the trap; angular momentum increase in the gas comes from the trap itself.
[22] M. V. Berry, J. Mod. Opt. **34**, 1401 (1987); J. Samuel and R. Bhandari, Phys. Rev. Lett. **60**, 2339 (1988).
[23] K. Kasamatsu and M. Tsubota, J. Low Temp. Phys. **126**, 315 (2002).
[24] I. Chuang *et al.*, Science **251**, 1336 (1991); M. J. Bowick *et al.*, Science **263**, 943 (1994).
[25] D. L. Feder *et al.*, Phys. Rev. A **62**, 053606 (2000).
[26] N. Whitaker *et al.*, cond-mat/0610242.

APPENDIX B

SAMPLE COMPUTER-GENERATED HOLOGRAM CODE

B.1 Example Kinoform Code

```
%-------------------------------------------------------------------------
%
%  Filename = kinoform.m
%
%  Author: Chad Weiler
%  Date: April 6, 2005
%  Borrowed Code From:  William Dallas
%  Comment: This program generates a Kinoform and saves the CGH as a
%           .bmp file to be used for the maskless writing tool.
%-------------------------------------------------------------------------


%----- BEGIN BLOCK ----- Clear all variables from the workspace


if(0)
  clear; % Clear the Matlab workspace
end


%------ END BLOCK ------


%----- BEGIN BLOCK ----- Set some program parameters and constants


  TRUE =  1;
  FALSE = 0;

  Pi = pi;
  TwoPi = 2.0*pi; % Two Pi.
  Ci = complex(0,1); % Square root of minus one

  FieldEdge = 1024;
  FieldCenter = (FieldEdge/2) + 1;


%------ END BLOCK ------


%----- BEGIN BLOCK ----- Generate a 256 gray-level color table


  Ramp = (0:255)/255.0; Gray256 = zeros(256,3);...
```

```
45      Gray256(:,1) = Ramp';
46    Gray256(:,2) = Ramp';  Gray256(:,3) = Ramp';
47
48
49  %------ END BLOCK ------
50
51
52  %----- BEGIN BLOCK ----- Figure Window Initialization
53
54
55   % Automatically set the sizes and positions the figure windows.
56   % Position parameters [x_left y _bottom x_width y_height]
57   % x is measured from the left of the window with a minimum of 4
58   % y is measured from the bottom of the screen. Positive
59   % up and right.
60
61    ScreenSizeVector = get(0,'ScreenSize');
62    Screen_xSize = ScreenSizeVector(3);
63    Screen_ySize = ScreenSizeVector(4);
64    Window_xSize = 0.40*Screen_xSize;
65    Window_ySize = 0.40*Screen_ySize;
66    Window_xySize = min(Window_xSize,Window_ySize);
67    Window_xPos1 = 8;
68    Window_xPos2 = Window_xPos1 + 1.02*Window_xySize;
69    Window_yPos1 = 8;
70    Window_yPos2 = Window_yPos1 + 1.25*Window_xySize;
71
72    figure_1 = [Window_xPos1 Window_yPos2 Window_xySize Window_xySize];
73    figure_2 = [Window_xPos2 Window_yPos2 Window_xySize Window_xySize];
74    figure_3 = [Window_xPos1 Window_yPos1 Window_xySize Window_xySize];
75    figure_4 = [Window_xPos2 Window_yPos1 Window_xySize Window_xySize];
76    figure_5 = [Window_xPos2 Window_yPos1 Window_xySize Window_xySize];
77
78
79  % Open the figure 1 window, position and clear it.
80    handle_1 = figure(1); pause(0.1);
81    set(handle_1,'position',figure_1); clf; home; drawnow;
82
83  % Open the figure 2 window, position and clear it.
84    handle_2 = figure(2); pause(0.1);
85    set(handle_2,'position',figure_2); clf; home; drawnow;
86
87  % Open the figure 3 window, position and clear it.
88    handle_3 = figure(3); pause(0.1);
89    set(handle_3,'position',figure_3); clf; home; drawnow;
90
91  % Open the figure 4 window, position and clear it.
92    handle_4 = figure(4); pause(0.1);
```

```
93    set(handle_4,'position',figure_4); clf; home; drawnow;
94
95
96  %Generate a 256 step graywedge map then load it
97
98    Ramp = (0:255)/255.0; Gray256 = zeros(256,3);
99    Gray256(:,1) = Ramp';
100   Gray256(:,2) = Ramp';  Gray256(:,3) = Ramp';
101   figure(1);  colormap(Gray256);
102   figure(2);  colormap(Gray256);
103   figure(3);  colormap(Gray256);
104   figure(4);  colormap(Gray256);
105
106
107
108 %------ END BLOCK ------  Figure Window Initialization
109
110
111 %----- BEGIN BLOCK ----- Import CGH pattern
112
113
114  inp = imread('directory');
115
116
117   a = zeros(FieldEdge,FieldEdge);
118   First = FieldCenter - 128;
119   Last = FieldCenter + 128 - 1;
120   Shift = 250;
121   a(First:Last,First+Shift:Last+Shift) = inp;
122
123
124 %------ END BLOCK ------
125
126
127 %------Begin Block----------Apply a diffuser
128
129
130   Phi = TwoPi*rand(FieldEdge,FieldEdge);
131   Diffuser = exp(Ci*Phi);
132   u = a.*Diffuser;
133
134
135 %------ END BLOCK ------
136
137
138 %----- BEGIN BLOCK ----- Display the object
139
140
```

```
141   figure(1);
142   Value = abs(u);
143   MaxValue = max(max(Value));
144   Gain = 255.99/MaxValue;
145   image(Gain*Value);
146   TextBuffer = 'Image';
147   title(TextBuffer);
148
149
150 %------ END BLOCK ------
151
152 %----- BEGIN BLOCK ----- Gerchberg-Saxton
153
154
155 for i = 1:1:15
156
157     U = fftshift(fft2(fftshift(u)));
158     U = U./abs(U);
159     u = fftshift(ifft2(fftshift(U)));
160     Diffuser = u./abs(u);
161     u = a.*Diffuser;
162
163 end
164
165 phase = angle(U);
166 phase = phase - min(min(phase));
167 a = find(phase ≥ pi);
168 b = find(phase ≤ pi);
169 phase(a) = pi;
170 phase(b) = 0;
171 CGH = exp(Ci*phase);
172 % CGH = repmat(CGH,2,2);
173
174
175 %------ END BLOCK ------
176
177
178 %----- BEGIN BLOCK ----- Display the Fourier transform
179
180
181   figure(2);
182   Value2 = angle(CGH);
183   MinValue2 = min(min(Value2));
184   MaxValue2 = max(max(Value2));
185   Gain = 255/(2*MaxValue2);
186   Value2 = Gain*(Value2);
187   image(Value2);
188   TextBuffer = 'CGH';
```

```
189   title(TextBuffer);
190
191
192 %------ END BLOCK ------
193
194
195
196 %----- BEGIN BLOCK -----  Reconstruct the CGH
197
198
199 Reconstruction = fftshift(ifft2(fftshift(CGH)));
200
201
202 %------ END BLOCK ------
203
204
205 %----- BEGIN BLOCK -----  Generate image of the Reconstruction
206
207
208 figure(3);
209   Value3 = abs(Reconstruction);
210   MaxValue3 = max(max(Value3));
211   Gain = 255.99/MaxValue3;
212   image(Gain*Value3);
213   TextBuffer = 'Reconstruction';
214   title(TextBuffer);
215
216
217 %------ END BLOCK ------
218
219
220 %----- BEGIN BLOCK ----- Write the CGH as a .bmp file
221
222
223  imwrite(uint8(Value4),'directory')
224
225
226 %------ END BLOCK ------
227
228
229 %----- BEGIN BLOCK ----- CLEAN UP AND EXIT.
230
231
232   if(FALSE); % Alternative is FALSE
233     %
234     pause; % Wait on enter key before closing the display window
235     %
236     % Close all open figure windows unconditionally
```

```
237      %
238      set(0,'ShowHiddenHandles','on')
239      delete(get(0,'Children'))
240      %
241      clear; % Clear memory
242      clc; % Clear the command window
243    end
244    %
245    return;
246
247
248  %------ END BLOCK ------
249
250
251  %
252  % END OF MAIN PROGRAM ***
253  %
254  %!!!!!!!!!!!!!!!!!!! END OF M-FILE !!!!!!!!!!!!!!!!!!!!!!
```

B.2 Example Binary Phase Code

```
%-------------------------------------------------------------------------
%  Filename = Binary_Kinoform.m
%
%  Author: Chad Weiler
%  Date: April 6, 2005
%  Borrowed Code From:  William Dallas
%  Comment: This program generates a  Binary Phase CGH and saves
%           the CGH as a bmp file to be used for the maskless
%           writing tool.
%-------------------------------------------------------------------------

%----- BEGIN BLOCK ----- Clear all variables from the workspace

if(0)
  clear; % Clear the Matlab workspace
end

%------ END BLOCK ------

%----- BEGIN BLOCK ----- Set some program parameters and constants

  TRUE =  1;
  FALSE = 0;

  Pi = pi;
  TwoPi = 2.0*pi; % Two Pi.
  Ci = complex(0,1); % Square root of minus one

  FieldEdge = 2*1024;
  FieldCenter = (FieldEdge/2) + 1;

%------ END BLOCK ------

%----- BEGIN BLOCK ----- Generate a 256 gray-level color table

 Ramp = (0:255)/255.0; Gray256 = zeros(256,3); Gray256(:,1) = Ramp';
 Gray256(:,2) = Ramp';  Gray256(:,3) = Ramp';

%------ END BLOCK ------

%----- BEGIN BLOCK ----- Figure Window Initialization

 % Automatically set the sizes and positions the figure windows.
 % Position parameters [x_left y _bottom x_width y_height]
```

```
45  % x is measured from the left of the window with a minimum of 4
46  % y is measured from the bottom of the screen.
47  % Positive up and right.
48
49   ScreenSizeVector = get(0,'ScreenSize');
50   Screen_xSize = ScreenSizeVector(3);
51   Screen_ySize = ScreenSizeVector(4);
52   Window_xSize = 0.40*Screen_xSize;
53   Window_ySize = 0.40*Screen_ySize;
54   Window_xySize = min(Window_xSize,Window_ySize);
55   Window_xPos1 = 8;
56   Window_xPos2 = Window_xPos1 + 1.02*Window_xySize;
57   Window_yPos1 = 8;
58   Window_yPos2 = Window_yPos1 + 1.25*Window_xySize;
59
60  figure_1 = [Window_xPos1 Window_yPos2 Window_xySize Window_xySize];
61  figure_2 = [Window_xPos2 Window_yPos2 Window_xySize Window_xySize];
62  figure_3 = [Window_xPos1 Window_yPos1 Window_xySize Window_xySize];
63  figure_4 = [Window_xPos2 Window_yPos1 Window_xySize Window_xySize];
64
65 % Open the figure 1 window, position and clear it.
66   handle_1 = figure(1); pause(0.1);
67   set(handle_1,'position',figure_1); clf; home; drawnow;
68
69 % Open the figure 2 window, position and clear it.
70   handle_2 = figure(2); pause(0.1);
71   set(handle_2,'position',figure_2); clf; home; drawnow;
72
73 % Open the figure 3 window, position and clear it.
74   handle_3 = figure(3); pause(0.1);
75   set(handle_3,'position',figure_3); clf; home; drawnow;
76
77 % Open the figure 4 window, position and clear it.
78   handle_4 = figure(4); pause(0.1);
79   set(handle_4,'position',figure_4); clf; home; drawnow;
80
81
82 %Generate a 256 step graywedge map then load it
83
84   Ramp = (0:255)/255.0; Gray256 = zeros(256,3);
85   Gray256(:,1) = Ramp';
86   Gray256(:,2) = Ramp';  Gray256(:,3) = Ramp';
87   figure(1);  colormap(Gray256);
88   figure(2);  colormap(Gray256);
89   figure(3);  colormap(Gray256);
90   figure(4);  colormap(Gray256);
91
92
```

```
93
94  %------ END BLOCK ------  Figure Window Initialization
95
96  %----- BEGIN BLOCK ----- Import CGH pattern
97  %Also shift the object off axis
98
99   inp = imread('defect.bmp');
100
101
102    a = zeros(FieldEdge,FieldEdge);
103    First = FieldCenter - 128;
104    Last = FieldCenter + 128 - 1;
105    Shift = 250;
106    a(First:Last,First+Shift:Last+Shift) = inp;
107
108 %------ END BLOCK ------
109
110
111 %------Begin Block----------Apply a diffuser
112
113    Phi = TwoPi*rand(FieldEdge,FieldEdge);
114    Diffuser = exp(Ci*Phi);
115    u = a.*Diffuser;
116
117 %------ END BLOCK ------
118
119 %----- BEGIN BLOCK ----- Display the object
120
121    figure(1);
122    Value = abs(u).^2;
123    MaxValue = max(max(Value));
124    Gain = 255.99/MaxValue;
125    Value = Gain*Value;
126    image(Value);
127    TextBuffer = 'Image';
128    title(TextBuffer);
129
130 %------ END BLOCK ------
131
132 %----- BEGIN BLOCK ----- Gerchberg-Saxton
133
134 for i = 1:1:50
135
136      U = fftshift(fft2(fftshift(u)));
137      U = U./abs(U);
138      u = fftshift(ifft2(fftshift(U)));
139      Diffuser = u./abs(u);
140      u = a.*Diffuser;
```

```
141
142 end
143
144
145 %------ END BLOCK ------
146
147
148 %----- BEGIN BLOCK ----- Constrain the phase to either 0 or 1.
149
150
151 phase = angle(U);
152 phase = phase - min(min(phase));
153 b = find(phase >= pi);
154 c = find(phase < pi);
155 phase(b) = pi;
156 phase(c) = 0;
157 CGH = exp(Ci*phase);
158
159
160 %------ END BLOCK ------
161
162
163
164 %----- BEGIN BLOCK ----- Display the Fourier transform
165 %Write the CGH to a bitmap file
166
167   figure(2);
168   Value2 = real(CGH);
169   MinValue2 = min(min(Value2));
170   MaxValue2 = max(max(Value2));
171   Gain = 255.99/(MaxValue2);
172   Value2 = Gain*Value2;
173   image(Value2);
174   TextBuffer = 'CGH';
175   title(TextBuffer);
176
177
178  imwrite(uint8(Value2),'1um_Y.bmp','bmp')
179
180 %------ END BLOCK ------
181
182 %----- BEGIN BLOCK -----  Reconstruct the CGH
183
184 Reconstruction = fftshift(ifft2(fftshift(CGH)));
185
186 %------ END BLOCK ------
187
188
```

```
189 %----- BEGIN BLOCK -----  Generate image of the Reconstruction
190
191 figure(3);
192   Value3 = abs(Reconstruction).^2;
193   MaxValue3 = max(max(Value3));
194   Gain = 255.99/MaxValue3;
195   Value3 = Gain*Value3;
196   image(Value3);
197   TextBuffer = 'Reconstruction';
198   title(TextBuffer);
199
200 %------ END BLOCK ------
201
202 %----- BEGIN BLOCK -----  Generate image of the Reconstruction
203
204
205 % figure(4);
206 %   Value4 = angle(CGH);
207 %   Value4 = repmat(Value4,2,2);
208 %   MinValue4 = min(min(Value4));
209 %   MaxValue4 = max(max(Value4));
210 %   Gain = 255.99/MaxValue4;
211 %   Value4 = Gain*Value4;
212 %   image(Value4);
213 %   TextBuffer = 'Tiled';
214 %   title(TextBuffer);
215
216
217 %------ END BLOCK ------
218
219
220 %----- BEGIN BLOCK ----- CLEAN UP AND EXIT.
221
222   if(FALSE); % Alternative is FALSE
223     %
224     pause; % Wait on enter key before closing the display window
225     %
226     % Close all open figure windows unconditionally
227     %
228     set(0,'ShowHiddenHandles','on')
229     delete(get(0,'Children'))
230     %
231     clear; % Clear memory
232     clc; % Clear the command window
233   end
234   %
235   return;
236
```

```
237 %------ END BLOCK ------
238
239
240 %----- BEGIN BLOCK -----
241
242
243
244 %------ END BLOCK ------
245
246
247
248
249 %
250 % END OF MAIN PROGRAM ***
251 %
252 %!!!!!!!!!!!!!!!!!!! END OF M-FILE !!!!!!!!!!!!!!!!
```

B.3 Example: Y mask code

```
%-------------------------------------------------------------------------
%
%  Filename = direct_image_mask_Y.m
%
%  Author: Brian Anderson
%  Modified by: Chad Weiler
%  Comment: This program is designed to create a 1cm x 1 cm binary
%  mask for direct imaging. Mask has 4 identical Y openings at each
%  corner of the mask.  The mask is then scaled accordingly for the
%  MLT and outputted as a .bmp file.

%-------------------------------------------------------------------------



%----- BEGIN BLOCK -----  Clear Matlab workspace


clear all


%------ END BLOCK ------


%----- BEGIN BLOCK ----- Create the Y mask


 nx = 834;            %set up the Grid
    dx = 6e-6;
    xmax = dx*nx;

nmid = floor(nx/2);
v = [0:nx-1]';
x = v*dx - xmax/2;
y = x;
[X,Y] = meshgrid(x,y);
R = sqrt(X.^2 + Y.^2);


    ca = 5e-6;
    cR = 60e-6;
    cth = 2*acos(cR/sqrt(cR^2 + ca^2));
    cph = pi/2-cth/2;
    cb = ca*sin(pi/2+cth/2)/sin(pi/3-cth/2);
```

```
45      cc = ca*sin(cph)/sin(pi-pi/6-cph);
46      m1 = -sqrt(3)*cR/2/(cR/2-cc);
47      m2 = -sqrt(3)*cR/2/(cR/2+cb);
48
49      Rg1 = (Y >= m1*(X+cc));
50      Rg2 = (Y <= m2*X+cb*tan(pi/3-cth/2));
51      Rg3 = (Y <= ca*(1 - X/cR));
52
53      mask2 = Rg1.*Rg2 + Rg3.*(X>0);
54      mask2 = (mask2>0).*(Y>=0);
55
56      Rg4 = (Y <= -m1*(X+cc));
57      Rg5 = (Y >= -(m2*X+cb*tan(pi/3-cth/2)));
58      Rg6 = (Y >= -ca*(1 - X/cR));
59
60      mask3 = Rg4.*Rg5 + Rg6.*(X>0);
61      mask3 = (mask3>0).*(Y<=0);
62
63      masklin0 = 1*(mask2+mask3);
64      masklin0 = (masklin0>0);
65
66
67      masklin_tiled(1:nx,1:nx) = masklin0;
68      masklin_tiled(nx+1:nx+nx,1:nx) = masklin0;
69      masklin_tiled(1:nx,nx+1:nx+nx) = masklin0;
70      masklin_tiled(nx+1:nx+nx,1+nx:nx+nx) = masklin0;
71
72
73  %------ END BLOCK ------
74
75
76  %----- BEGIN BLOCK ----- Create a 256 gray level cololrmap (needed for the
77  %MLT)
78
79
80  Ramp = (0:255)/255.0; Gray256 = zeros(256,3); Gray256(:,1) = Ramp';
81    Gray256(:,2) = Ramp';  Gray256(:,3) = Ramp';
82
83    Ramp = (0:255)/255.0; Gray256 = zeros(256,3);
84    Gray256(:,1) = Ramp';
85    Gray256(:,2) = Ramp';  Gray256(:,3) = Ramp';
86    figure(1);  colormap(Gray256);
87
88    figure(1);
89    Value = masklin_tiled;
90    MaxValue = max(max(Value));
91    Gain = 255.99/MaxValue;
92    Value = Gain*Value;
```

```
93    image(Value);
94    TextBuffer = 'Cosing Grating';
95    title(TextBuffer);
96
97
98  %------ END BLOCK ------
99
100
101 %----- BEGIN BLOCK -----  Write the file to a bmp
102
103
104 imwrite(uint8(Value),'directory')
105
106
107 %------ END BLOCK ------
108
109
110
111
112
113
114 %      imagesc(x,y,masklin_tiled)
115 %      axis image
116 %      colormap gray
117
118
119
120 %----- BEGIN BLOCK -----
121
122
123
124 %------ END BLOCK ------
```

B.4 Phase Dot Code

```
%Phase Dot
Ramp = (0:255)/255.0; Gray256 = zeros(256,3); Gray256(:,1) = Ramp';
  Gray256(:,2) = Ramp';  Gray256(:,3) = Ramp';

 nx = 3500;            % number of grid points.
    dx = 2.00e-6;           % spatial grid step, in meters



    xmax = dx*nx;    % spatial extent of grid, in meters

nmid = floor(nx/2);
v = [0:nx-1]';
x = v*dx - xmax/2;
y = x;
[X,Y] = meshgrid(x,y);
square = X ≤ 50e-6 & X ≥ -50e-6 & Y ≤ 50e-6 & Y ≥ -50e-6 ;

Value = square;
  MaxValue = max(max(Value));
  Gain = 255.99/MaxValue;
  Value = Gain*Value;

figure(1);
colormap(Gray256);
image(Value)

imwrite(Value,'test(150).bmp','bmp')
```

APPENDIX C

SHIPLEY MICROPOSIT S1800 SERIES PHOTORESITS SPECIFICATIONS

SHIPLEY

MICROPOSIT® S1800® SERIES PHOTO RESISTS

MICROPOSIT S1800 SERIES PHOTO RESISTS are positive photoresist systems engineered to satisfy the microelectronics industry's requirements for advanced IC device fabrication. The system has been engineered using a toxicologically safer alternative casting solvent to the ethylene glycol derived ether acetates. The dyed photoresist versions are recommended to minimize notching and maintain linewidth control when processing on highly reflective substrates.

MICROPOSIT S1800 SERIES PHOTO RESISTS FEATURE:

Product Assurance
- Lot-to-lot consistency through state-of-the-art physical, chemical and functional testing
- Filtered to 0.2 µm absolute

Coating Properties
- [1]Cellosolve® Acetate and xylene free
- Striation-free coatings
- Excellent adhesion
- Excellent coating uniformity
- A variety of standard viscosities are available for single-layer processing

Exposure Properties
- Optimized for G-Line exposure
- Effective for broad-band exposure
- Reflective notch and linewidth control using dyed versions

Develop Properties
- Optimized for use with the MICROPOSIT® MF®-319 Metal-Ion-Free DEVELOPER family
- Compatible with Metal-Ion-Bearing MICROPOSIT DEVELOPERS

Removal Property
- Residue-free photoresist removal using standard MICROPOSIT REMOVERS

High Resolution Process Parameters (Refer to Figure 1)	
Substrate:	Polysilicon
Photoresist:	MICROPOSIT®S1813® PHOTO RESIST
Coat:	12,300Å
Softbake:	115°C/60 sec. Hotplate
Exposure:	Nikon 1505 G6E, G-Line (0.54 NA), 150 mJ/cm^2
Develop:	MICROPOSIT® MF®-321 DEVELOPER
	15 + 50 sec. Double Spray Puddle (DSP) @ 21°C

[1]Registered trademark of Union Carbide Corporation

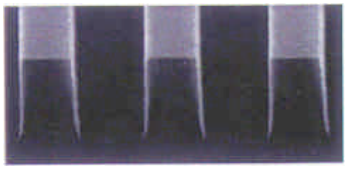

0.80 µm Lines/Spaces

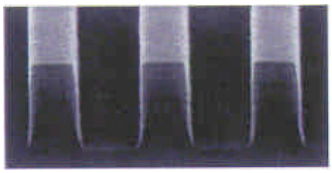

0.70 µm Lines/Spaces

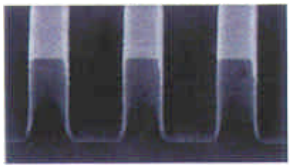

0.60 µm Lines/Spaces

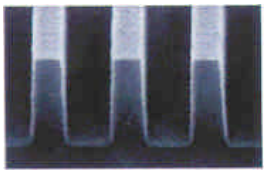

0.50 µm Lines/Spaces

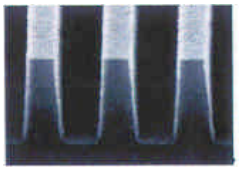

0.48 µm Lines/Spaces

Masking Linearity SEMS
Figure 1.

Instructions for Use

The following instructions cover the use of MICROPOSIT S1800 SERIES PHOTO RESISTS for all levels of microelectronic device fabrication. Exact process parameters are application and equipment dependent.

Substrate Preparation

MICROPOSIT S1800 SERIES PHOTO RESISTS work well with the hexamethyldisilazane based MICROPOSIT PRIMERS. Concentrated MICROPOSIT PRIMER is recommended when vacuum vapor priming. Diluted PRIMER is recommended for liquid phase priming applications.

Coat

MICROPOSIT S1800 SERIES PHOTO RESISTS provide uniform defect-free coatings over a wide range of film thicknesses. The film thickness versus spin speed plots displayed in **Figures 1 and 2** provide the information required to properly select a MICROPOSIT S1800 PHOTO RESIST version to meet process dependent thickness specifications. Maximum coating uniformity is typically attained between the spin speeds of 3500 rpm and 5500 rpm.

Process Parameters (Refer to Figures 1 and 2)	
Substrate	Silicon .
Coat	SVG 81
Softbake	115°C/60 seconds Hotplate
Measure	Nanometrics 210

The dispersion curve and Cauchy equation displayed in **Figure 3** describe how the refractive index of the photoresist film varies as a function of the wavelength of light incident upon the film. This information is required to program ellipsometric and other optically based photoresist measuring equipment.

Process Parameters (Refer to Figure 3)	
Substrate	Silicon
Coat	13,675Å
Softbake	115°C/60 seconds Hotplate
Measure	Prometrix SM300

MICROPOSIT S1800 PHOTO RESIST UNDYED SERIES

Figure 1. Spin Speed Curves

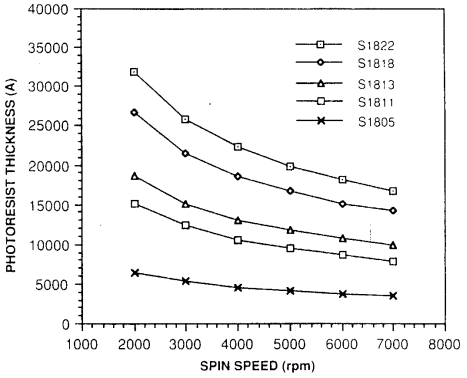

MICROPOSIT S1800 PHOTO RESIST DYED SERIES

Figure 2. Spin Speed Curves

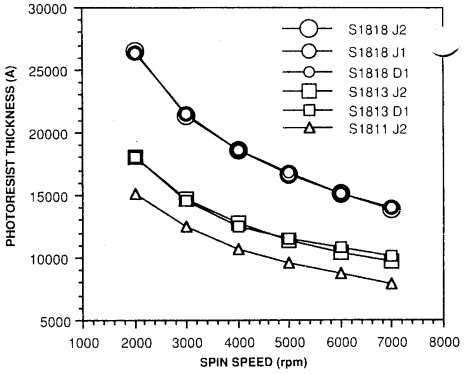

MICROPOSIT® S1813® PHOTO RESIST

Figure 3. Dispersion Curve

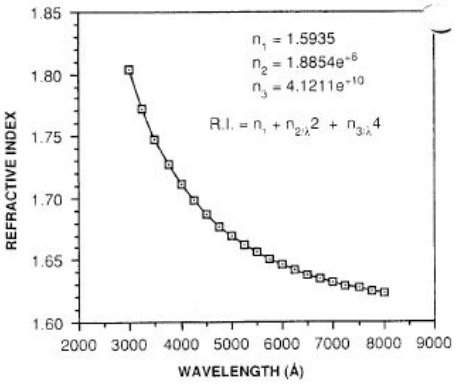

Exposure

Proper film thickness selection is critical in order to reduce photospeed and critical dimension variability. The interference curves displayed in **Figure 4** illustrate the photospeed variability as a function of film thickness. Dyed versions suppress the interference effects which are more pronounced when exposing with monochromatic light sources and when using reflective substrates.

Process Parameters (Refer to Figure 4)	
Substrate	Silicon
Coat	GCA 1006 [2]WAFERTRAC®
Softbake	115°C/60 seconds Hotplate
Expose	GCA 8500 G-Line (0.35 NA)
Developer	MF-321 /10 + 30 DSP @ 21°C

MICROPOSIT S1800 SERIES PHOTO RESISTS can be exposed with light sources in the spectral output range of 350 nm -450 nm. The exposure properties have been optimized for use at 436 nm. **Figures 5 and 6** show the absorbance spectrums for MICROPOSIT S1813 and S1813 J2® PHOTO RESISTS.

Process Parameters (Refer to Figures 5 and 6)	
Substrate	Quartz
Coat	12,300Å
Softbake	115°C/60 seconds Hotplate
Expose	Oriel Scanning Wedge
Measure	Hewlett Packard 8450A Spectrophotometer

Table 1 summarizes the Dill parameters for each MICROPOSIT S1800 SERIES PHOTO RESIST version. Dill parameters are used in optical exposure models such as SAMPLE and PROLITH.

MICROPOSIT S1800 SERIES PHOTO RESISTS
Table 1. Dill Parameters

	365 nm		436 nm	
Photoresist	A (μm^{-1})	B (μm^{-1})	A (μm^{-1})	B (μm^{-1})
S1813	1.07	0.31	0.61	0.08
S1813 D1	1.05	0.34	0.58	0.26
S1811 J2	1.07	0.49	0.59	0.61
S1818 J1	1.06	0.42	0.57	0.37

[2] Registered Trademark of GCA, a unit of General Signal

MICROPOSIT S1813 and S1813 J2 PHOTO RESISTS
Figure 4. Interference Curves

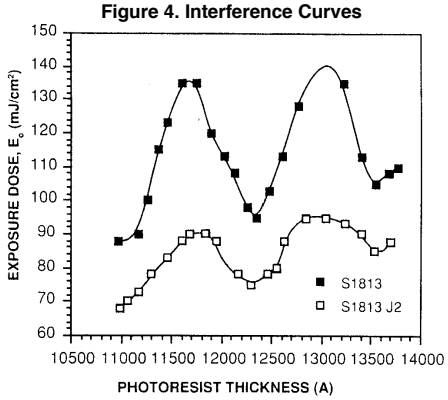

MICROPOSIT S1813 PHOTO RESIST
Figure 5. Absorbance Spectrum

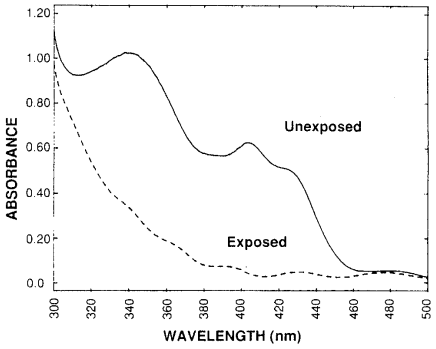

MICROPOSIT S1813 J2 PHOTO RESIST
Figure 6. Absorbance Spectrum

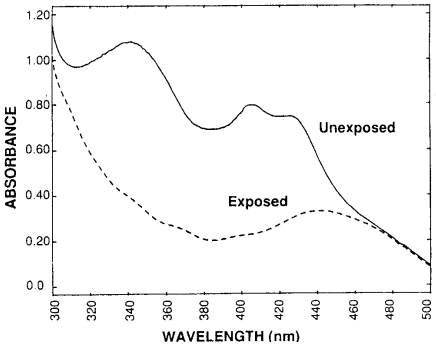

Figure 7 displays a contrast curve for MICROPOSIT S1813 PHOTO RESIST developed with MICROPOSIT® MF®-321 DEVELOPER. In general, high contrast values correlate to higher angle wall profiles.

Process Parameters (Refer to Figure 7)	
Substrate	Silicon
Coat	12,300Å
Softbake	115°C/60 seconds Hotplate
Expose	GCA 8500 G-Line (0.35 NA)
Develop	MF-321 /10 + 30 DSP @ 21°C

DEVELOP

MICROPOSIT S1800 SERIES PHOTO RESISTS are compatible with both Metal-Ion-Free (MIF) and Metal-Ion-Bearing (MIB) developers. A photoresist and developer system is dependent upon specific application requirements. Contact your local Shipley Technical Sales Representative for additional product information.

Figures 8 thru 10 illustrate the lithographic functionality of MICROPOSIT S1813 PHOTO RESIST using process parameters designed to maximize resolution while maintaining excellent exposure and focus latitude (refer to SEM photographs in **Figure 1**). The functional lithographic responses are summarized in **Table 2**.

Process Parameters (Refer to Figures 8 thru 10)	
Substrate	Silicon
Coat	12,300Å
Softbake	115°C/60 seconds Hotplate
Expose	Nikon 1505 G6E G-Line (0.54 NA)
Develop	MF-321 /15 + 50 DSP @ 21°C

MICROPOSIT S1813 PHOTO RESIST with MICROPOSIT MF-321 DEVELOPER

Table 2. Functional Lithographic Summary Data

Sizing Energy	150 mJ/cm^2 (1.3 E_0)	
Resolution	0.48 µm	
Masking Linearity (±10% CD)	0.50 µm	
	1.0µm L/S	0.60 µm L/S
Exposure Latitude (±10% CD)	65%	45%
Focus Latitude (±10% CD) ≥ 85° Wall Angle	2.25 µm	1.25 µm

MICROPOSIT S1813 PHOTO RESIST
Figure 7. Contrast Curve

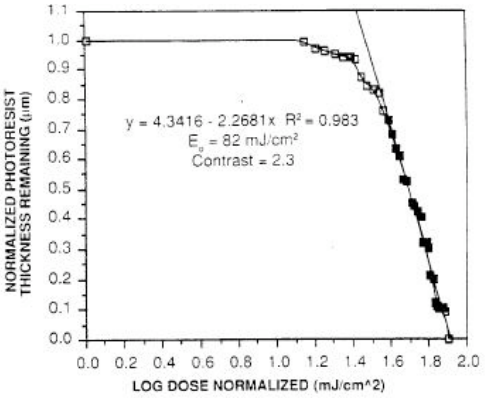

MICROPOSIT S1813 PHOTO RESIST
Figure 8. Masking Linearity Plot

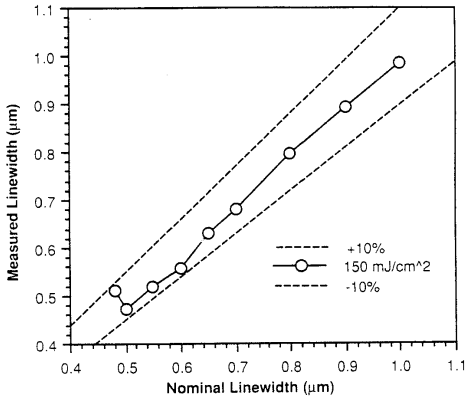

MICROPOSIT S1813 PHOTO RESIST
Figure 9. Exposure Latitude Plot

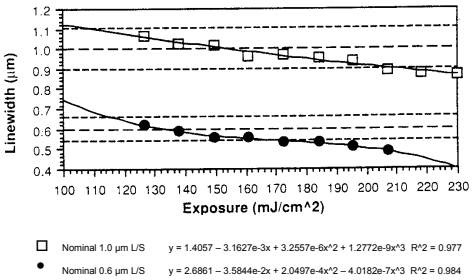

MICROPOSIT S1813 PHOTO RESIST
Figure 10. Focus Latitude Plot

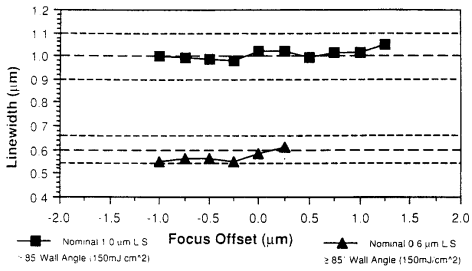

Handling Precautions

WARNING: MICROPOSIT S1800 SERIES PHOTO RESISTS are combustible mixtures containing propylene glycol monomethyl ether acetate. Contact with eyes, skin and mucous membranes causes irritation. Handle with care. Do not get in eyes, on skin or on clothing. Avoid breathing vapors or mists. Use with adequate ventilation. Wash thoroughly after handling.

Wear chemical goggles, chemical gloves and suitable protective clothing when handling MICROPOSIT S1800 SERIES PHOTO RESISTS.

In case of eye or skin contact, flush affected areas with plenty of water for at least 15 minutes. Then contact a physician at once.

Consult product Material Safety Data Sheet before using.

Toxicological and Health Advantages

The solvent used in MICROPOSIT S1800 SERIES PHOTO RESISTS is propylene glycol monomethyl ether acetate. Toxicological studies reported that propylene glycol derivatives contained in MICROPOSIT S1800 SERIES PHOTO RESISTS do **not** demonstrate the adverse blood effects and reproductive effects that ethylene glycol derived ether acetates demonstrate (NIOSH Current Intelligence Bulletin 9 -5/2/83).

Storage

Store MICROPOSIT S1800 PHOTO RESISTS only in upright, original containers in a dry area at 50°-70°F (10°-21°C). Store away from light, oxidants, heat, and sources of ignition. Do not store in sunlight. Keep container sealed when not in use.

Equipment

MICROPOSIT S1800 SERIES PHOTO RESISTS are compatible with most commercially available photoresist processing equipment. Compatible materials include stainless steel, glass, ceramic, unfilled polypropylene, high density polyethylene, polytetrafluoroethylene, or equivalent materials.

Technical Literature

Please contact your Shipley Technical Sales Representative for information on the use and performance of Shipley products.

REFERENCES

[1] A. Gill, "Defects and the dynamics of phase transitions," *Contemporary Physics*, vol. 39, no. 1, pp. 13–47, 1998.

[2] R. P. Feynman, *Statistical Mechanics*. Addison Wesley Longman, 1972.

[3] C. Kittel and H. Kroemer, *Thermal Physics*. W.H. Freeman and Company, 1980.

[4] R. Bowley and M. Sánchez, *Introductory Statistical Mechanics: Second Edition*, ch. 11. Oxford University Press, second ed., 1999.

[5] A. Rajantie, "Defect formation in the early universe," *Contemporary Physics*, vol. 44, no. 6, pp. 485–502, 2003.

[6] T. Kibble, "Symmetry breaking and defects," *Arxiv preprint cond-mat/0211110*, 2002.

[7] T. W. Kibble, "Classification of topological defects and their relevance to cosmology and elsewhere," in *Topological Defects and the Non-Equilibrium Dynamics of Symmetry Breaking Phase Transitions* (Y. M. Bunkov and H. Godfrin, eds.), pp. 7– 11, Kluwer Academic Publishers, 2000.

[8] E. Alfinito, O. Romei, and G. Vitiello, "On Topological Defect Formation in the process of symmetry breaking phase transitions," *Modern Physics Letters B*, vol. 16, no. 4, pp. 93–106, 2002.

[9] T. Kibble, "Topology of cosmic domains and strings," *Journal of Physics A: Mathematical and General*, vol. 9, no. 8, pp. 1387–1398, 1976.

[10] W. Zurek, "Cosmological experiments in superfluid helium?," *Nature*, vol. 317, no. 6037, pp. 505–508, 1985.

[11] J. Anglin and W. Zurek, "Vortices in the Wake of Rapid Bose-Einstein Condensation," *Physical Review Letters*, vol. 83, no. 9, pp. 1707–1710, 1999.

[12] R. Peierls, "Spontaneously broken symmetries," *Journal of Physics A: Mathematical and General*, vol. 24, no. 22, pp. 5273–5281, 1991.

[13] R. Peierls, "Broken symmetries," *Contemporary Physics*, vol. 33, no. 4, pp. 221–226, 1992.

[14] Y. Bunkov and H. Godfrin, *Topological Defects and the Non-Equilibrium Dynamics of Symmetry Breaking Phase Transitions*. Kluwer Academic Publishers, 2000.

[15] A. Rajantie, "Formation of Topological Defects in Gauge Field Theories," *International Journal of Modern Physics A*, vol. 17, no. 1, pp. 1–43, 2002.

[16] M. Hindmarsh and A. Rajantie, "Defect Formation and Local Gauge Invariance," *Physical Review Letters*, vol. 85, no. 22, pp. 4660–4663, 2000.

[17] A. Vilenkin and E. Shellard, *Cosmic Strings and Other Topological Defects*. Cambridge University Press, 1994.

[18] E. A. Cornell, J. R. Ensher, and C. E. Wieman, "Experiments in dilute atomic Bose-Einstein condensation," in *Bose-Einstein Condensation in Atomic Gases, Proceedings of the International School of Physics "Enrico Fermi", Course CXL* (M. Inguscio, S. Stringari, and C. E. Wieman, eds.), pp. 15–66, IOS Press, 1999.

[19] J. Ensher, *The First Experiments with Bose-Einstein Condensation of 87 Rb*. PhD thesis, University of Colorado, 1998.

[20] M. Bijlsma and H. Stoof, "Renormalization group theory of the three-dimensional dilute Bose gas," *Physical Review A*, vol. 54, no. 6, pp. 5085–5103, 1996.

[21] D. Scherer, C. Weiler, T. Neely, and B. Anderson, "Vortex Formation by Merging of Multiple Trapped Bose-Einstein Condensates," *Physical Review Letters*, vol. 98, no. 11, p. 110402, 2007.

[22] D. Scherer, *Vortex Formation by Merging and Interference of Multiple Trapped Bose-Einstein Condensates*. PhD thesis, The University of Arizona, 2007.

[23] D. Stauffer, M. Ferer, and M. Wortis, "Universality of Second-Order Phase Transitions: The Scale Factor for the Correlation Length," *Physical Review Letters*, vol. 29, no. 6, pp. 345–349, 1972.

[24] S. Sondhi, S. Girvin, J. Carini, and D. Shahar, "Continuous quantum phase transitions," *Reviews of Modern Physics*, vol. 69, no. 1, pp. 315–333, 1997.

[25] T. Kibble, "Phase-transition dynamics in the lab and the universe," *Physics Today*, vol. 60, no. 9, pp. 47–52, 2007.

[26] F. Dalfovo, S. Giorgini, L. Pitaevskii, and S. Stringari, "Theory of Bose-Einstein condensation in trapped gases," *Reviews of Modern Physics*, vol. 71, no. 3, pp. 463–512, 1999.

[27] A. Leggett, "Bose-Einstein condensation in the alkali gases: Some fundamental concepts," *Reviews of Modern Physics*, vol. 73, no. 2, pp. 307–356, 2001.

[28] M. Andrews, C. Townsend, H. Miesner, D. Durfee, D. Kurn, and W. Ketterle, "Observation of Interference Between Two Bose Condensates," *Science*, vol. 275, no. 5300, pp. 637–641, 1997.

[29] A. Griffin, D. Snoke, and S. Stringari, *Bose-Einstein Condensation*. Cambridge University Press, 1995.

[30] C. J. Pethick and H. Smith, *Bose-Einstein Condensation In Dilute Gases*. Cambridge: Cambridge University Press, 2004.

[31] D. Tilley and J. Tilley, *Superfluidity and Superconductivity*. Hilger, 1986.

[32] R. Donnelly, *Quantized Vortices in Helium II*. Cambridge University Press, 1991.

[33] M. Matthews, B. Anderson, P. Haljan, D. Hall, C. Wieman, and E. Cornell, "Vortices in a Bose-Einstein Condensate," *Physical Review Letters*, vol. 83, no. 13, pp. 2498–2501, 1999.

[34] A. Leanhardt, A. Görlitz, A. Chikkatur, D. Kielpinski, Y. Shin, D. Pritchard, and W. Ketterle, "Imprinting Vortices in a Bose-Einstein Condensate using Topological Phases," *Physical Review Letters*, vol. 89, no. 19, p. 190403, 2002.

[35] S. Inouye, S. Gupta, T. Rosenband, A. Chikkatur, A. Görlitz, T. Gustavson, A. Leanhardt, D. Pritchard, and W. Ketterle, "Observation of Vortex Phase Singularities in Bose-Einstein Condensates," *Physical Review Letters*, vol. 87, no. 8, p. 80402, 2001.

[36] J. Abo-Shaeer, C. Raman, J. Vogels, and W. Ketterle, "Observation of vortex lattices in Bose-Einstein condensates," *Science*, vol. 292, no. 5516, pp. 476–479, 2001.

[37] P. Haljan, I. Coddington, P. Engels, and E. Cornell, "Driving Bose-Einstein-Condensate Vorticity with a Rotating Normal Cloud," *Physical Review Letters*, vol. 87, no. 21, p. 210403, 2001.

[38] E. Hodby, G. Hechenblaikner, S. Hopkins, O. Maragò, and C. Foot, "Vortex Nucleation in Bose-Einstein Condensates in an Oblate, Purely Magnetic Potential," *Physical Review Letters*, vol. 88, no. 1, p. 10405, 2001.

[39] K. Madison, F. Chevy, W. Wohlleben, and J. Dalibard, "Vortex Formation in a Stirred Bose-Einstein Condensate," *Physical Review Letters*, vol. 84, no. 5, pp. 806–809, 2000.

[40] B. Anderson, P. Haljan, C. Regal, D. Feder, L. Collins, C. Clark, and E. Cornell, "Watching Dark Solitons Decay into Vortex Rings in a Bose-Einstein Condensate," *Physical Review Letters*, vol. 86, no. 14, pp. 2926–2929, 2001.

[41] Z. Dutton, M. Budde, C. Slowe, and L. Hau, "Observation of quantum shock waves created with ultra-compressed slow light pulses in a Bose-Einstein condensate," *Science*, vol. 293, no. 5530, pp. 663–668, 2001.

[42] M. V. Berry, "The adiabatic phase and Pancharatnams phase for polarized light,," *Journal of Modern Physics*, vol. 34, pp. 1401–1407, 1987.

[43] J. Samuel and R. Bhandari, "General Setting for Berry's Phase," *Physical Review Letters*, vol. 60, no. 23, pp. 2339–2342, 1988.

[44] B. V. Svistunov, "Highly nonequilibrium Bose condensation in a weakly interacting gas," *J. Mosc. Phys. Soc.*, vol. 1, p. 373, 1991.

[45] Y. Kagan *et al.*, "The Bose-condensation kinetics in an interacting Bose-gas," *Zh. Éksp. Teor. Fiz.*, vol. 101, p. 528, 1992. [Sov. Phys. JETP **75**, 387 (1992)].

[46] Y. Kagan and B. V. Svistunov, "Kinetics of long-range order formation in Bose-condensation in interacting gas," *Zh. Éksp. Teor. Fiz.*, vol. 105, p. 353, 1994. [Sov. Phys. JETP **78**, 187 (1994)].

[47] Y. Kagan and B. V. Svistunov, "Evolution of Correlation Properties and Appearance of Broken Symmetry in the Process of Bose-Einstein Condensation," *Phys. Rev. Lett.*, vol. 79, p. 3331, 1997.

[48] B. Svistunov, *Quantized Vortex Dynamics and Superfluid Turbulence*, vol. 571 of *Lecture Notes in Physics*, ch. Kinetics of Strongly Non-Equilibrium Bose-Einstein Condensation. Springer-Verlag, 2001.

[49] N. G. Berloff and B. V. Svistunov, "Scenario of strongly nonequilibrated Bose-Einstein condensation," *Phys. Rev. A*, vol. 66, p. 013603, Jul 2002.

[50] B. V. Svistunov, "Strongly non-equilibrium Bose-Einstein condensation in a trapped gas," *Phys. Lett. A*, vol. 287, p. 169, 2001.

[51] C. W. Gardiner, P. Zoller, R. J. Ballagh, and M. J. Davis, "Kinetics of Bose-Einstein Condensation in a Trap," *PRL*, vol. 79, p. 1793, 1997.

[52] C. W. Gardiner, M. D. Lee, R. J. Ballagh, M. J. Davis, and P. Zoller, "Quantum Kinetic Theory of Condensate Growth: Comparison of Experiment and Theory," *PRL*, vol. 81, p. 5266, 1998.

[53] M. D. Lee and C. W. Gardiner, "Quantum kinetic theory. VI. The growth of a Bose-Einstein condensate," *Phys. Rev. A*, vol. 62, p. 033606, Aug 2000.

[54] M. J. Davis, C. W. Gardiner, and R. J. Ballagh, "Quantum kinetic theory. VII. The influence of vapor dynamics on condensate growth," *Phys. Rev. A*, vol. 62, p. 063608, Nov 2000.

[55] M. J. Bijlsma, E. Zaremba, and H. T. C. Stoof, "Condensate growth in trapped Bose gases," *Phys. Rev. A*, vol. 62, p. 063609, Nov 2000.

[56] M. J. Davis and C. W. Gardiner, "Growth of a Bose-Einstein condensate: a detailed comparison of theory and experiment," *J. Phys. B.*, vol. 35, p. 733, 2002.

[57] I. Shvarchuck, C. Buggle, D. S. Petrov, K. Dieckmann, M. Zielonkowski, M. Kemmann, T. G. Tiecke, W. von Klitzing, G. V. Shlyapnikov, and J. T. M. Walraven, "Bose-Einstein Condensation into Nonequilibrium States Studied by Condensate Focusing," *Phys. Rev. Lett.*, vol. 89, p. 270404, Dec 2002.

[58] H.-J. Miesner, D. M. Stamper-Kurn, M. Andrews, D. Durfee, S. Inouye, and W. Ketterle, "Bosonic stimulation in the formation of a Bose-Einstein condensate," *Science*, vol. 279, p. 1005, 1998.

[59] M. Köhl, M. J. Davis, C. W. Gardiner, T. W. Hänsch, and T. W. Esslinger, "Growth of Bose-Einstein Condensates from Thermal Vapor," *PRL*, vol. 88, p. 080402, 2002.

[60] M. Hugbart, J. A. Retter, A. F. Varón, P. Bouyer, A. Aspect, and M. J. Davis, "Population and phase coherence during the growth of an elongated Bose-Einstein condensate," *Phys. Rev. A*, vol. 75, p. 011602, Jan 2007.

[61] S. Ritter, A. Öttl, T. Donner, T. Bourdel, M. Köhl, and T. Esslinger, "Observing the formation of long-range order during bose-einstein condensation," *Phys. Rev. Lett.*, vol. 98, p. 090402, 2007.

[62] G. Karra and R. Rivers, "Reexamination of Quenches inˆ{4} He (andˆ{3} He)," *Physical Review Letters*, vol. 81, no. 17, pp. 3707–3710, 1998.

[63] R. Rivers, "Slowˆ{4} He Quenches Produce Fuzzy, Transient Vortices," *Physical Review Letters*, vol. 84, no. 6, pp. 1248–1251, 2000.

[64] M. Hindmarsh and A. Rajantie, "Phase transition dynamics in the hot Abelian Higgs model," *Physical Review D*, vol. 64, no. 6, p. 65016, 2001.

[65] J. Higbie, L. Sadler, S. Inouye, A. Chikkatur, S. Leslie, K. Moore, V. Savalli, and D. Stamper-Kurn, "Direct Nondestructive Imaging of Magnetization in a Spin-1 Bose-Einstein Gas," *Physical Review Letters*, vol. 95, no. 5, p. 50401, 2005.

[66] P. Hendry, N. Lawson, R. Lee, P. McClintock, and C. Williams, "Generation of defects in superfluid 4 He as an analogue of the formation of cosmic strings," *Nature*, vol. 368, no. 6469, pp. 315–317, 1994.

[67] M. Dodd, P. Hendry, N. Lawson, P. McClintock, and C. Williams, "Nonappearance of Vortices in Fast Mechanical Expansions of Liquid^{4} He through the Lambda Transition," *Physical Review Letters*, vol. 81, no. 17, pp. 3703–3706, 1998.

[68] C. Baüerle, Y. M. Bunkov, S. N. Fisher, H. Godfrin, and G. R. Pickett, "Laboratory simulation of cosmic-string formation in the early universe using superfluid He-3," *Nature*, vol. 382, p. 332, 1996.

[69] V. Ruutu, V. Eltsov, A. Gill, T. Kibble, M. Krusius, Y. Makhlin, B. Placais, G. Volovik, and W. Xu, "Vortex formation in neutron-irradiated superfluid 3 He as an analogue of cosmological defect formation," *Nature*, vol. 382, no. 6589, pp. 334–336, 1996.

[70] R. Monaco, M. Aaroe, J. Mygind, R. Rivers, and V. Koshelets, "Experiments on spontaneous vortex formation in Josephson tunnel junctions," *Physical Review B*, vol. 74, no. 14, p. 144513, 2006.

[71] S. Ducci, P. Ramazza, W. González-Viñas, and F. Arecchi, "Order Parameter Fragmentation after a Symmetry-Breaking Transition," *Physical Review Letters*, vol. 83, no. 25, pp. 5210–5213, 1999.

[72] W. Petrich, M. Anderson, J. Ensher, and E. Cornell, "Stable, Tightly Confining Magnetic Trap for Evaporative Cooling of Neutral Atoms," *Phys. Rev. Lett.*, vol. 74, no. 17, p. 3352, 1995.

[73] A. A. Svidzinsky and A. L. Fetter, "Dynamics of a vortex in a trapped Bose-Einstein condensate," *Phys. Rev. A*, vol. 62, p. 063617, Nov 2000.

[74] A. Lohmann and D. Paris, "Binary Fraunhofer holograms, generated by computer," *Applied Optics*, vol. 6, no. 10, p. 1739, 1967.

[75] A. Lohmann, "A Pre-History of Computer-Generated Holography," *Optics and Photonics News*, vol. 19, no. 2, p. 36, 2008.

[76] A. MacGovern and J. Wyant, "Computer generated holograms for testing optical elements," *Appl. Opt*, vol. 10, no. 3, pp. 619–624, 1971.

[77] Y. Cheng, A. Isoyan, J. Wallace, M. Khan, and F. Cerrina, "Extreme ultraviolet holographic lithography: Initial results," *Applied Physics Letters*, vol. 90, p. 023116, 2007.

[78] R. Eriksen, V. Daria, and J. Gluckstad, "Fully dynamic multiple-beam optical tweezers," *Optics Express*, vol. 10, no. 14, pp. 597–602, 2002.

[79] R. Gerchberg, "W. 0. Saxton," A practical algorithm for the determination of phase from image and diffraction plane pictures,"," *Optik*, vol. 35, no. 2, 1972.

[80] J. Fienup, "Phase retrieval algorithms: a comparison.," *Applied Optics*, vol. 21, no. 15, pp. 2758–2769, 1982.

[81] R. Firth, D. Kessler, E. Muka, M. Naor, and J. Owens, "A continuous-tone laser color printer.," *J. IMAG. TECHNOL.*, vol. 14, no. 3, pp. 78–89, 1988.

[82] J. C. Burbach, T. S. Fisli, and G. K. Starkweather, "Laser scanning for electronic printing," *Proc. of IEEE*, vol. 70, no. 6, pp. 597–618, 1982.

[83] W. Flack, D. Soong, A. Bell, and D. Hess, "A mathematical model for spin coating of polymer resists," *Journal of Applied Physics*, vol. 56, p. 1199, 1984.

[84] P. C. Hendry, N. S. Lawson, R. Lee, P. V. E. McClintock, and C. D. H. Williams, "Generation of defects in superfluid ^{4}He as an analog of the formation of cosmic strings," *Nature*, vol. 368, p. 315, 1994.

[85] V. M. H. Ruutu, V. B. Eltsov, A. J. Gill, T. W. B. Kibble, M. Krusius, Y. G. Makhlin, B. Placais, G. E. Volovik, and W. Xu, "Vortex formation in neutron-irradiated superfluid ^{3}He as an analogue of cosmological defect formation," *Nature*, vol. 382, p. 334, 1996.

[86] C. Baüerle, Y. M. Bunkov, S. N. Fisher, H. Godfrin, and G. R. Pickett, "Laboratory simulation of cosmic string formation in the early Universe using superfluid ^{3}He," *Nature*, vol. 382, p. 332, 1996.

[87] M. Dodd, P. Hendry, N. Lawson, P. McClintock, and C. Williams, "Nonappearance of vortices in the fast mechanical expansions of liquid ^{4}he through the Lambda transition," *Phys. Rev. Lett*, vol. 81, p. 3703, 1998.

[88] M. J. Davis, R. J. Ballagh, and K. Burnett, "Dynamics of thermal Bose fields in the classical limit," *J. Phys. B*, vol. 34, p. 4487, 2001.

[89] C. W. Gardiner, J. R. Anglin, and T. I. A. Fudge, "The Stochastic Gross-Pitaevskii equation," *J. Phys. B.*, vol. 35, p. 733, 2002.

[90] C. W. Gardiner and M. J. Davis, "The Stochastic Gross-Pitaevskii equation:II," *J. Phys. B.*, vol. 36, p. 4731, 2003.

[91] P. B. Blakie and M. J. Davis, "Projected Gross-Pitaevskii equation for harmonically confined Bose gases at finite temperature," *Phys. Rev. A*, vol. 72, p. 063608, 2005.

[92] H. T. C. Stoof, "Coherent Versus Incoherent Dynamics During Bose-Einstein Condensation in Atomic Gases," *J. Low Temp. Phys.*, vol. 114, p. 11, Jan. 1999.

[93] E. Zaremba, T. Nikuni, and A. Griffin, "Dynamics of Trapped Bose Gases at Finite Temperatures," *J. Low. Temp. Phys.*, vol. 116, p. 277, 1999.

[94] H. T. C. Stoof, "A superfluid is born," *Nature*, vol. 447, p. 390, 2007.

[95] P. Kevrekidis, D. Frantzeskakis, and R. Carretero-Gonzalez, "Emergent Nonlinear Phenomena in Bose-Einstein Condensates: Theory and Experiment," *Springer Series on Atomic, Optical, and Plasma Physics*, vol. 45, 2008.

[96] A. S. Bradley, C. W. Gardiner, and M. J. Davis, "Bose-Einstein condensation from a rotating thermal cloud: Vortex nucleation and lattice formation," *arXiv:*, p. 0712.3436, 2007.

[97] P. B. Blakie and M. J. Davis, "Classical Region of a Trapped Bose Gas," *J. Phys. B*, vol. 40, p. 2043, 2007.

[98] M. J. Davis and P. B. Blakie, "Critical Temperature of a Trapped Bose Gas: Comparison of Theory and Experiment," *Phys. Rev. Lett.*, vol. 96, p. 060404, 2006.

[99] K. Gòral, M. Gajda, and K. Rzążewski, "Multi-mode description of an interacting Bose-Einstein condensate," *Phys. Rev. A*, vol. 66, p. 051602(R), 2002.

[100] C. Ryu, M. F. Andersen, P. Clade, V. Natarajan, K. Helmerson, and W. D. Phillips, "Observation of Persistent Flow of a Bose-Einstein Condensate in a Toroidal Trap," *Phys. Rev. Lett.*, vol. 99, p. 260401, 2007.

[101] D. Stamper-Kurn, M. Andrews, A. Chikkatur, S. Inouye, H. Miesner, J. Stenger, and W. Ketterle, "Optical Confinement of a Bose-Einstein Condensate," *Physical Review Letters*, vol. 80, no. 10, pp. 2027–2030, 1998.

[102] J. Stenger, D. Stamper-Kurn, M. Andrews, A. Chikkatur, S. Inouye, H. Miesner, and W. Ketterle, "Optically Confined Bose–Einstein Condensates," *Journal of Low Temperature Physics*, vol. 113, no. 3, pp. 167–188, 1998.

[103] S. Inouye, A. Chikkatur, D. Stamper-Kurn, J. Stenger, D. Pritchard, and W. Ketterle, "Superradiant Rayleigh Scattering from a Bose-Einstein Condensate," *Science*, vol. 285, no. 5427, pp. 571–574, 1999.